Theory of Laser-Induced Ultrafast Structural Changes in Solids: Calculations on Cerium, Samarium Sulfide, Germanium and Bismuth.

Inaugural-Dissertation
zur Erlangung der
Doktorwürde der Naturwissenschaften
(Dr. rer. nat)

vorgelegt beim Fachbereich Naturwissenschaften
der Universität Kassel

von

Momar Sokhna Diakhate
aus Louga, Senegal

December, 2009

Supervisor Prof. Dr. Martin E. Garcia
Institut für Physik,
Universität Kassel,
Heinrich-Plett-Str. 40,
34132 Kassel, GERMANY.

Day of disputation is 17-th of december 2009

Abstract

The present thesis is a contribution to the study of laser-solid interaction. Despite the numerous applications resulting from the recent use of laser technology, there is still a lack of satisfactory answers to theoretical questions regarding the mechanism leading to the structural changes induced by femtosecond lasers in materials. We provide here theoretical approaches for the description of the structural response of different solids (cerium, samarium sulfide, bismuth and germanium) to femtosecond laser excitation. Particular interest is given to the description of the effects of the laser pulse on the electronic systems and changes of the potential energy surface for the ions. Although the general approach of laser-excited solids remains the same, the potential energy surface which drives the structural changes is calculated with different theoretical models for each material. This is due to the difference of the electronic properties of the studied systems. We use the Falicov model combined with an hydrodynamic method to study photoinduced phase changes in cerium. The local density approximation (LDA) together with the Hubbard-type Hamiltonian (LDA+U) in the framework of density functional theory (DFT) is used to describe the structural properties of samarium sulfide. We parametrize the time-dependent potential energy surface (calculated using DFT+ LDA) of bismuth on which we perform quantum dynamical simulations to study the experimentally observed amplitude collapse and revival of coherent A_{1g} phonons. On the basis of a time-dependent potential energy surface calculated from a non-orthogonal tight binding Hamiltonian, we perform molecular dynamics simulation to analyze the time evolution (coherent phonons, ultrafast nonthermal melting) of germanium under laser excitation. The thermodynamic equilibrium properties of germanium are also reported. With the obtained results we are able to give many clarifications and interpretations of experimental results and also make predictions.

Table of Contents

List of Tables

List of Figures

Chapter 1

Introduction

The main motivation of this work is the understanding and description of the response of solids to ultrafast optical excitations. In particular, we have studied structural changes induced in solids by the creation of a hot electron-hole plasma.

The study of the interaction of femtosecond laser pulses (pulse duration $< 500fs$) with solids has attracted considerable attention during the last decades [GDG83, SLFE87, BFI87, TABC88, KCL$^+$88, LKJ$^+$00, CTS$^+$01, STBB$^+$03, LLSTeA05, BBSS06, RTD$^+$07, HEH$^+$08]. Several studies were motivated by the fact that femtosecond laser excitation offers a novel tool for inducing new phenomena in solids, promising exciting potential applications. Most of the fundamental processes occurring in nature such as chemical reactions and phase transitions involve structural changes. By exciting solids appropriately, many different structural changes can be induced. In fact, depending on the laser characteristics (wavelength, pulse energy, pulse duration), laser solid interaction can result in a wide range of structural responses.

Among the different laser induced structural changes observed one can mention ultrafast melting [SAPF96a, JHL$^+$03, LLSTeA05], solid-solid phase transitions [CTS$^+$01, KTM03, RTD$^+$07, KEH$^+$07, CBRZ08], ablation [BBSS06, RSTvdLA04] and also generation of coherent phonons [PKKS92, SPK93, NHM$^+$01, MMHK04, IKU06, ZTG06a]. The advantage of using ultrashort laser pulse is that the different stages during the structural changes can be studied in a time-resolved way. For instance, melting, ablation and re-solidification phenomena take place on different time scales [BBSS06] (see figure 1.1) and therefore can be investigated separately.

A clear understanding of the mechanism for the structural response of solids to femtosec-

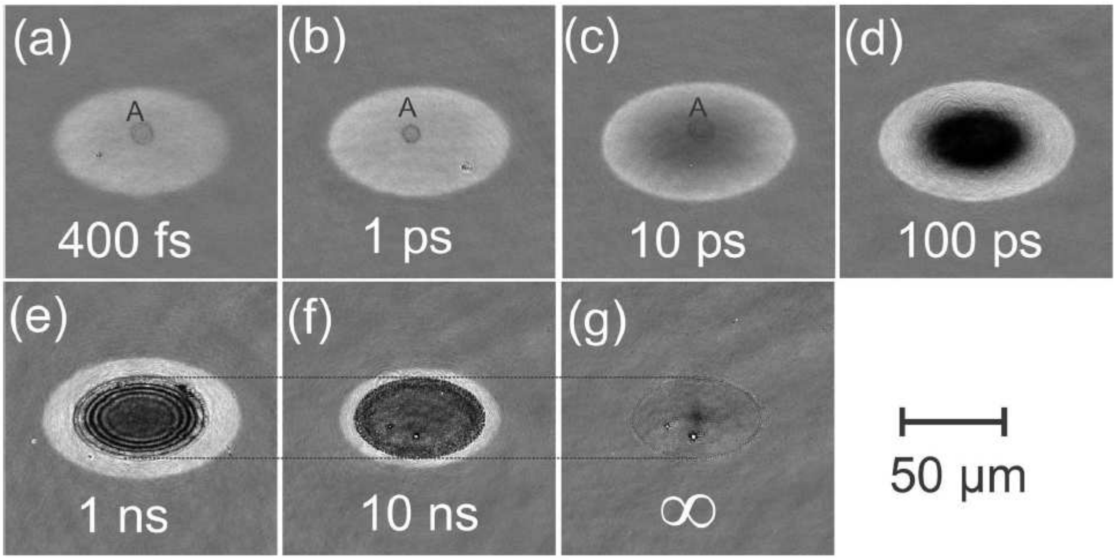

Figure 1.1: Images of a germanium surface at different times after the laser excitation (pump fluence $3.10 \pm 0.08 J/cm^2$, ablative regime). A denotes an imaging artifact which is not related to a modification of the sample surface. The image sequence is encoded in a linear gray scale with an optimized contrast. *Figure reproduced from [BBSS06].*

ond laser excitation is therefore essential to take advantages of the huge technological applications possible.

Since the development of techniques using ultrashort laser pulses in the 1980s, a considerable number of applications have been found. For example, ultrafast laser techniques offer possibilities to shape tissues and skin for medical replacement and to manipulate and fabricate nano-sized materials which have direct applications in our everyday life. Despite the huge and technological applications in real world and the intense research investigations on the subject, a complete and exact understanding of the ultrafast dynamical processes which take place during and after an intensive excitation of materials still remains a scientific and technological challenge.

New experimental techniques such as ultrafast x-ray diffraction [CTS+01, STBB+03, STBD+03, RTD+07] and time resolved reflectivity measurements [BBSS06, CBRZ08, HEH$^+$08] allow to follow the detailed steps of matter transformation within the time scale on which the effect of a laser pulse is considered. Thus with the help of these techniques one can investigate the first steps in the laser driven phase transitions and transformations of materials. Up to the development of pump-probe techniques, it has not been possible to directly observe the atomic motion leading to a phase transformation in matter. For instance, while the first and last step of a chemical reaction was well established, it was not possible to probe the different intermediate steps of the elementary reactions. With the development of pump-probe techniques, structural changes are now measured in a time-resolved way. In the 1990s, *Zewail and coworkers* [Zew88, Zew92, PHP$^+$92, Zew00] used ultrashort laser pulses to observe chemical reactions on the time scales they occur. The authors show that femtosecond laser pulses can be used as a mean to control the different processes occurring during chemical reactions [Zew88, KZ90] and structural changes in solids [KTM03, MMHK04, STBD$^+$03, BBSS06]. The main outcome is the possibility to obtain the quantitative structural informations of physical, chemical and biological systems on time scales that are comparable with the natural periods of vibrations of atoms and molecules ($10fs \leq T \leq 1ps$).

Among the experimental studies regarding structural responses of solids to femtosecond laser excitation done so far, one can mention the following examples which attract our attention and are part of the motivations of this theoretical work:

1) The first example is the work from *Kitagawa and coworkers* [KTM03]. They used a femtosecond laser pulse to study a volume collapse phase transition which occurs in samarium sulfide. *Kitagawa and coworkers* performed Grazing incidence x-ray diffraction (GIXD) analysis of SmS (Fig. 1.2), and showed that by exciting samarium sulfide using femtosecond laser it is possible to induce the semiconductor (S-SmS) to metal phase transition (M-SmS). Ce and SmS exhibit phase transitions with the same characteristics at ambient conditions [JNM70, LLC83]. Therefore by exciting cerium, the same physical

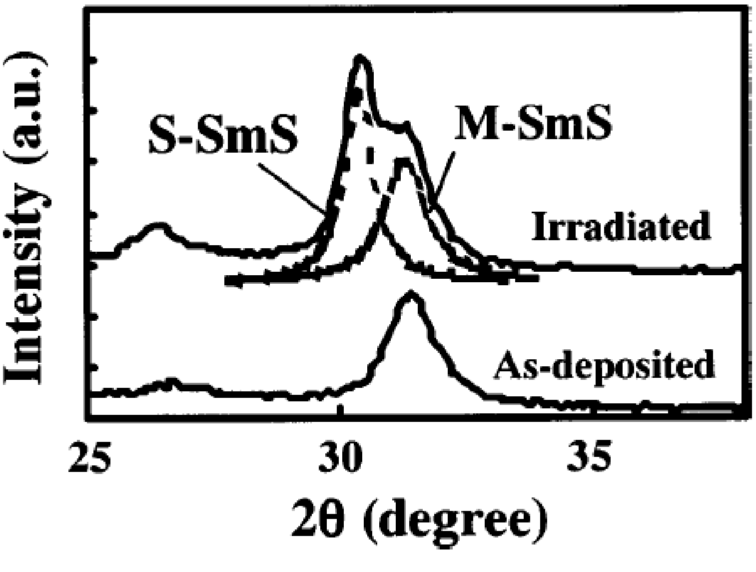

Figure 1.2: Grazing incidence x-ray diffraction (GIXD) analysis of the semiconductor samarium sulfide (S-SmS) to metal samarium sulfide (M-SmS) phase transition induced by femtosecond laser excitation. The figure shows the GIXD patterns of the as-deposited and irradiated film. *Figure reproduced from [KTM03]*

phenomenons can be expected. Up to now experiments regarding laser-induced transition in cerium have not been done.

2) The second example concerns the structural response of bismuth to femtosecond laser excitation. *Misochko and coworkers* [MMHK04] report measurements of the reflectivity of bismuth during and after the femtosecond laser pulse. The authors used a pulse duration of $130fs$ less than a phonon period. Figure 1.3 shows the time derivative of the reflectivity in bismuth at different laser fluences. It was shown that the amplitude of coherent $A_{1\mathrm{g}}$ phonon oscillations vanishes and, at a later time, reappears when the fluence of the pump laser is above a certain threshold value. This phenomenon was explained as a quantum mechanical effect and was therefore referred to as “amplitude collapse and revival”. The same phenomenon was observed in an independent experimental study by *Hase and coworkers* [HKNM02].

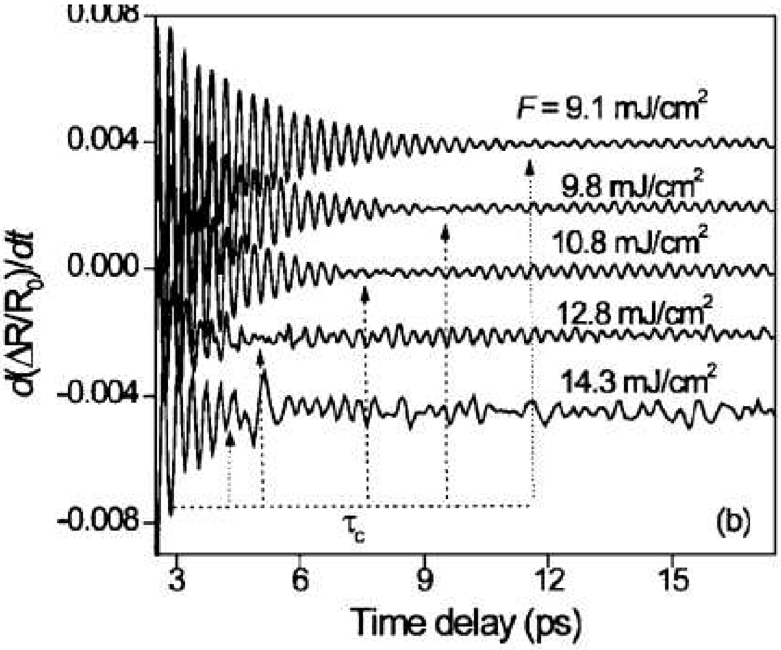

Figure 1.3: Time derivative of R/R0 as a function of the time delay demonstrating the collapse and revival in Bi at T = 10 K for different laser fluences with pulse duration of 130 fs (the transients are offset along the y axis and labeled with the fluence value). Arrows indicate the time collapse. *Figure reproduced from [MMHK04]*

3) The third and last example is related to the work from *Sokolowski-Tinten and coworkers* [STBB$^+$03, STBD$^+$03]. The authors report study of the non-thermal melting of germanium using ultrafast x-ray diffraction techniques. Non-thermal melting simply means that on the time scale on which the phase transition is observed, no thermal motions are involved (the lattice remains cold). The exchange energy between electrons and ions which causes the lattice heating, takes place usually in some picoseconds after the laser excitation peak. Therefore, the immediate change of the lattice structure after the laser excitation is entirely due to the presence of hot electron-hole plasma. The non-thermal melting can be seen from the loss of order indicated by the drop of the X-ray diffraction efficiency peak in figure 1.4. Another illustration of this non-thermal melting of germanium occurring in time scale less than half a picosecond is given in figure 1.1. In

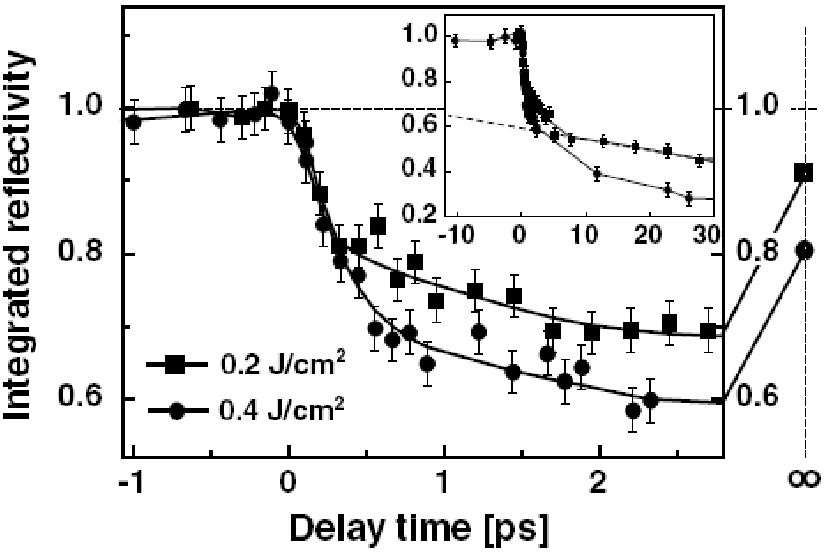

Figure 1.4: X-ray diffraction efficiency (integrated reflectivity) versus delay time. Infinity symbol: measurement a few minutes after the pump pulse. Inset: integrated reflectivity for an extended time span. Dashed line: melt from velocity of 850 m/s for rapid thermal melting. *Figure reproduced from [STBD⁺03]*

an independent work *Bonse and coworkers* [BBSS06] studied the different stages of laser driven structural changes in germanium. The authors used time-resolved reflectivity measurements and show that the non-thermal melting take place at time $t = 400fs$ after the laser peak. It was also shown in both experimental studies that after the laser excitation the system undergo several phases before ending to its almost initial phase at time $t = \infty$ (re-solidification), see figures 1.1 and 1.4.

Although the existing ultrafast x-ray diffraction techniques and time resolved reflectivity measurements allow monitoring of atomic motions in femtosecond time and angstrom spatial resolution, there are still a considerable uncertainty in the correspondence between the macroscopic quantities and the atomic scale properties for a given material. Therefore, there is need to go through the theoretical description of the response of materials to optical excitation.

A realistic theoretical description of laser heating solids must take into account explicitly the electronic as well as the atomic degrees of freedom. The reason is that, systems subjected to intense laser excitation will respond strongly to the modification of the interatomic potential or potential energy surface (PES) due to the significant electronic excitations. To calculate the potential energy surface which governs the atomic motion, several theoretical methods exist in various levels of sophistication: density functional theory, Hartree theory, tight binding approximations, empirical theory. Among these methods the most accurate and sophisticated ones so far are first principles (ab-initio) methods based on density functional theory [HK64, KS65].

However first principles methods are limited by the fact that they are computationally expensive. For this reason, theories based on simple empirical pair potential (for example Lennard-Jones-type potentials) are still in use for numerical study of dynamical properties of solids. In contrast to the other models, the empirical pair potentials do not include explicitly the electronic system and therefore are not suitable for the study of the dynamical processes which occur in excited systems. An intermediate possibility which combine a quantum mechanical treatment of electrons and classical treatment of ions is the tight binding theory. As discussed in section 2.4.1 the tight binding method is widely used because of its ability to treat different properties of solids in a reasonable way. The efficiency of tight binding formalism comes from the fact that the Hamiltonian can be parametrized. Consequently the electronic structure can be easily obtained. The tight binding Hamiltonian of solids are calculated from the hopping integral functions which are parameters and interatomic distance dependent. The difficulty of tight binding theory is to find an accurate and transferable model to study systems. Up to now only models for silicon [MS94a, BMP00], carbon [XWCH92] and germanium [MS98] exist.

Although many simulation methods of excited materials have been reported [VGCC96, SAPF96b, SP98], only few theoretical approaches which pay as much attention to the atomic as to the electronic system have been developed.

The starting point of the theoretical investigations was the work of Stampfli and Benneman [SB90, SB92, SB94] regarding the study of structural responses of covalent materials (silicon, carbon, germanium) to femtosecond laser excitation. Stampfli and Benneman analysed the ultrafast laser-induced instability of the diamond structure of semiconductors (Si,Ge,C). The cohesive energy of silicon was calculated [SB94] in function of transverse acoustic δ_t and longitudinal optic δ_l distortions (see figure 1.5). The time-dependent lattice instability of silicon was obtained and the results show that the softening of the tranverse acoustic modes are mainly responsible of the lattice changes. However due to the strong anharmonic interactions resulting from the laser-induced potential energy surface changes (figure 1.5), the longitudinal optical phonons are also affected. According to Stampfli and Benneman this lattice instability takes place within $120fs$ after the laser pulse and yields to rapid melting of the crystal. Same phenomenon was also observed for

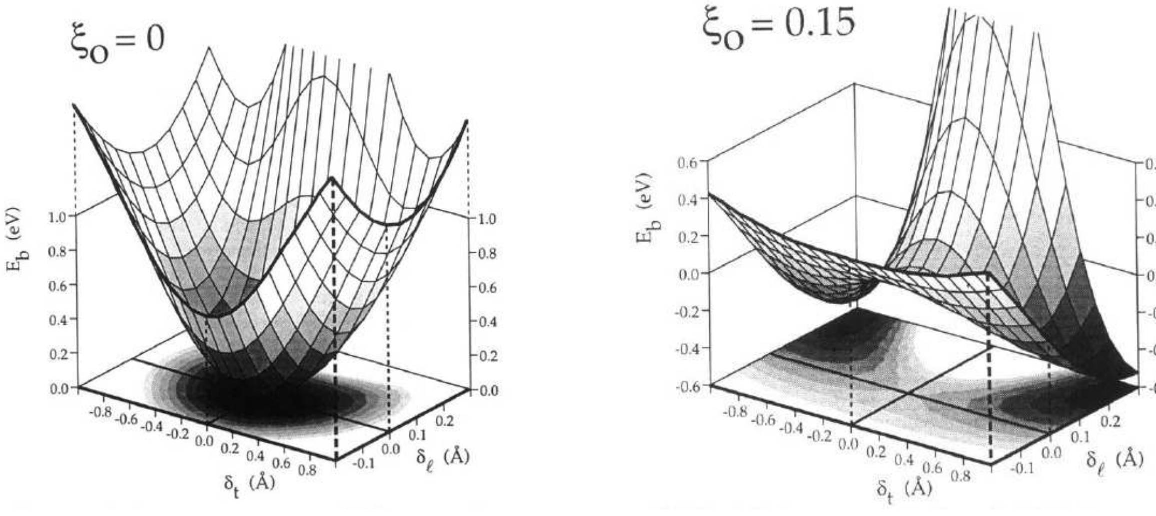

Figure 1.5: Cohesive energy of silicon in the absence of electron hole plasma (left figure) $\xi = 0.0$, and presence of hot electron-hole plasma of density $\xi = 0.15$ corresponding to the excitation of 15% of the valence electrons to the conduction band. δ_t and δ_l are respectively the transverse acoustic and longitudinal optic distortions (amplitude of the phonons). The ideal diamond structure ($\delta_t = \delta_l = 0$) becomes unstable in the presence of laser excitation (right figure) and corresponds to a stable minimum of the cohesive energy in the absence of excitation (left figure). *Figures reproduced from [SB94]*

gallium arsenide (GaAs) [SB93].

Later on Jeschke and Garcia [JGB99a, JGB99b, JGB01, JG, GJ03, RGV$^+$05] developed a theory based on the approach proposed by Stampfli and Benneman to study the response of covalent materials to femtosecond laser excitation. In contrast to the model from Stampfli and Benneman, the model proposed by Jeschke and Garcia incorporated explicitly the time dependent non-equilibrium occupation of the energy levels (taking into account explicitly the time dependent changes of the electronic occupation during and after the laser pulse) in the calculation of the potential energy surface. They used MD simulation on the basis of an orthogonal tight binding Hamiltonian. This model was well applied for the description of structural responses of graphite and carbon nanotubes [JGL$^+$02, GDJ04, DGJY04, RGV$^+$05, DGJY06, JDG09] to femtosecond laser excitation.

In the 1990s, *Parrinello and coworkers* [SAPF96b] have used first principles molecular dynamics simulation to study the dynamical response of silicon to ultrashort laser excitation. Similar study has been performed to describe laser-induced melting of graphite [SP98]. The method proposed by *Parrinello and coworkers* are mainly based on the treatment of ions and electrons with density functional theory in the local density approximation. Within these model, an instant creation of electron hole plasma is assumed at time $t = 0$ so that the duration of laser pulse is set to zero ($\tau = 0$). In fact the first principle methods do not allow an explicit time treatment of the laser pulse. We used a similar idea in the second purpose of this work, to calculate the potential energy surface of bismuth at high electronic temperatures (simulating laser excitation) and we proposed a model to include the time dependent laser parameters, see sec. 2.3.

The aim of this thesis is to provide theoretical approaches combined with simulation tools to:

i) Firstly study the structural responses of cerium to femtosecond laser excitation. Special attention is paid to the description of laser-induced volume changes in the vicinity of the fascinating isostructural phase transition (referred as $\alpha \longleftrightarrow \gamma$ phase transition). Figure 1.6 shows the observed isostructural phase transition [LLC83] (both phases are fcc structures) leading to a volume collapse of roughly 15% under ambient temperature and at a given critical external pressure. Same isostructural phase transition have been also observed for samarium sulfide [JNM70]. Regarding this fascinating behavior observed in both systems cerium and samarium sulfide the questions which have no clear answer up to now are: how the microscopic quantities (electronic structure) are coupled to the macroscopic quantities (volume change during the phase transition)? What is the driving mechanism of the transition? And finally what is the role of the correlation between f electrons and *spd* valence electrons in the transition? These fundamental questions are still under debate, and many experimental [vdEKvdM01, ea04] and theoretical studies [AM82, AL92, HOSK05] are devoted to this subject. We proposed an approach based

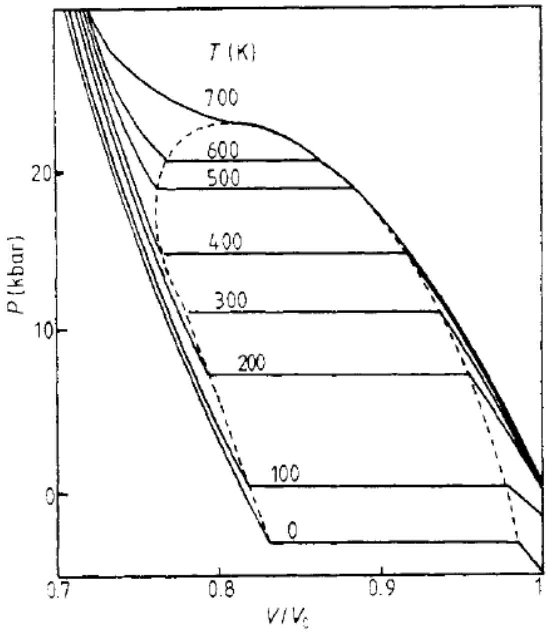

Figure 1.6: Time derivative of R/R0 as a Isotherm of cerium. Illustration of the volume collapse $\gamma \rightarrow \alpha$ transition at ambient temperatures. *Figure reproduced from [LLC83]*

on calculation of the potential energy surface from the model Hamiltonian proposed by Falicov [RF71] to study laser-induced phase changes in cerium. With a hydrodynamic simulation we estimate the time scale on which laser induced volume changes of cerium can occur and discuss about how the electronic structure changes are involved. We also investigated the structural properties of samarium Sulfide by means of first principle methods based on LDA+U. For this purpose we used LDA+U to study the equilibrium properties of SmS and discuss the possibility of laser induced the experimentally observed semiconductor-metal phase transition.

ii) Secondly we studied the dynamical response of bismuth to femtosecond laser excitation. A particular attention is given to the study of the experimentally observed amplitude collapse and revival of coherent A_{1g} phonons. When femtosecond laser pulse interacts with bismuth crystal, due to the presence of hot electron-hole plasma large amplitude coherent phonons are excited [HWDK95]. These collective lattice vibrations, which usually involve only a few degrees of freedom, provide a useful system to study both laser-matter interactions and the physical processes related to the relaxation of the non-thermal state induced by the laser [HKNM02, JBM+08, BGR+08]. A question that has received relatively little attention is, whether the induced phonons behave classically as is usually assumed or whether some quantum effects may be detected [MSN00]. In this respect interesting observation has recently been made by *Misochko and coworkers* [MMHK04] in bismuth: The goal of this work is to clarify whether the origin of the observed amplitude collapse and revival of the coherent A_{1g} phonon is classical or quantum mechanical. To this aim we have performed quantum dynamical simulations on time-dependent potential energy surfaces calculated using density functional theory and accurate full-potential linearized augmented plane wave methods. The time dependent potential energy surface includes explicitly the laser pulse parameters (fluence, intensity, pulse duration).

iii) The third and last purpose of this thesis is the description of ultrafast phenomenons occurring in covalent materials upon ultrashort laser excitation. Particular interest has been given to the semiconductor germanium. The aim of our investigations was to understand on which time scale do laser-induced structural transitions occur in germanium, and identify the different processes involved in the experimentally observed changes [PKKS92, SPK93, NHM$^+$01, STBD$^+$03, BBSS06]. And finally look at whether these different processes can be controlled by laser parameters like fluences, duration, and intensity. In this last part of the work a theory which is mainly based on the model proposed by Jeschke and Garcia [JGB99a, JGB99b, JGB01, JG, GJ03] for the description of laser induced electronic non-equilibrium states, will be developed and combine to MD simulations.

The thesis is organized as follows:

In chapter 2 we presents all the theoretical approaches and methods used for the calculations. In chapter 3 we present our results. Finally in chapter 4 we give a general conclusion and discuss about the future work perspectives.

Chapter 2

Theory

This chapter starts with an overview of the theoretical approach outlining the general aspects of the methodology used to describe laser-irradiated solids. This is followed by the application of this theoretical framework to the different systems (Ce, SmS, Bi, Ge), although using different methods for the calculation of the potential energy surface which drives the structural changes.

2.1 Theoretical approach of laser excited solids

In this section we introduce the basic concepts of the theoretical description of laser-induced structural changes in solids. The approaches used are mainly based on the calculation of the time-dependent potential energy surface and an explicit treatment of electronic degrees of freedom.

The physics and the resulting phenomena of laser excitation of materials can be summarized as follow: In most of the cases, intense femtosecond laser pulses are able to produce in solids a situation of extreme non-equilbrium state in which electrons acquire very high temperatures while the lattice remains cold. This is due to the fact that on the time scale on which the laser interacts with solids, the laser energy is initially coupled with the carriers yielding to the creation of electron-hole pairs (the excited electrons and holes thermalize on a very short time-scale [STvdL04]). The exchange energy between electrons and ions resulting from the relaxation process, takes place usually in some picoseconds after the laser excitation peak. This relaxation time is usually referred to as electron-phonon coupling time and causes delayed heating of the lattice. Thus, a significant increase of the lattice temperature is observed only within several picoseconds. Therefore the immediate change of the lattice structure after the laser excitation is entirely due to the presence of a hot electron-hole plasma and no thermal motions are involved. Furthermore, depending on the density of excited carriers and the laser characteristics, this extremely rapid excitation can lead to several structural transformations such as solid-liquid [SAPF96a, JHL$^+$03, LLSTeA05], solid-solid [JGB99a, CTS$^+$01, KEH$^+$07, JGB01, CBRZ08, RTD$^+$07, KTM03] phase transitions, and also generation of coherent phonons [PKKS92, SPK93, NHM$^+$01, MMHK04, IKU06, ZTG06a].

In fact, the types of phenomenon which occurs after the laser excited solids can be divided into three main classes depending upon the laser characteristics. In the case of low laser energy, the interaction produces only an increase in the electronic pressure resulting to a volume expansion of the heated region while the cold region (unexcited part) is compressed (see below for the case of cerium). However depending on the symmetry of the studied system, the generation of coherent phonons is possible at low fluences (for example diamond structure of germanium [PKKS92, IKU06], rhombohedral structure of bismuth [MMHK04, ZTG06b]). At high laser energies when a certain fluence threshold is exceeded, the interaction may give rise to ultrafast non-thermal melting [STBB$^+$03, BBSS06, ZTG06b, ZWG$^+$08] and ablation [RSTvdLA04].

The knowledge of time dependent electronically excited potential energy surfaces is essential for describing properly these different processes. The physical picture of the response of solids to laser excitation used in the present work is summarized in figures 2.1 and 2.2.

Figure 2.1 illustrates the effect of a short laser pulse on the potential energy surface. During the irradiation of an absorbing crystalline material, the incident optical energy is coupled to the carriers, which are excited from bonding (valence states) to anti-bonding states (conduction band states). Consequently, the inter-atomic forces are therefore mod-

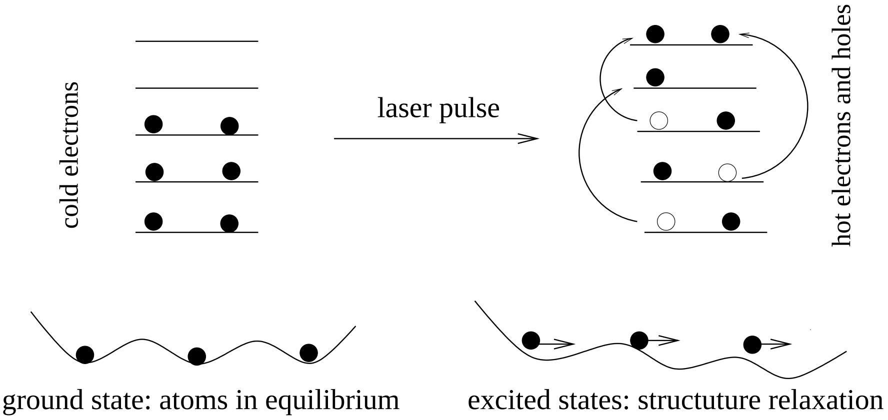

Figure 2.1: Illustration of laser excitation of solids and the resulting effect on the potential energy surface. This scheme shows the effect of a generation of dense electron-hole plasma on the potential energy surface which governs the atomic motions. Situation before the action of the laser pulse: the solid is in thermodynamical equilibrium. For low temperatures, the electrons fill the states up to the Fermi level. The atoms are at the equilibrium positions of the ground state potential energy surface. The laser pulse changes the electronic occupations. This leads to rapid changes in the potential energy landscape. As a consequence, the lattice becomes unstable and forces appear on the atoms, driving a structural change.

ified and cause the structural changes.

Figure 2.2 shows the sketch of the electronic distribution during and after the laser excitation process. In the ground state (electron temperature T_0) electrons show a Fermi-like distribution. During the absorption of laser energy we assist to a non-equilibrium distribution followed by a rapid thermalization of carriers at temperatures much higher than the ground state temperature.

From the ideas mentioned above, one can conclude that a realistic description of laser heating of solids, must take into account explicitly the electrons as well as the atomic degrees of freedom. Thus, the link between electrons and atomic structure for a given material has to be established in an explicit manner in order to consider properly the laser excitation effects.

The coupling of the laser energy to the electrons of the target material is one of the most

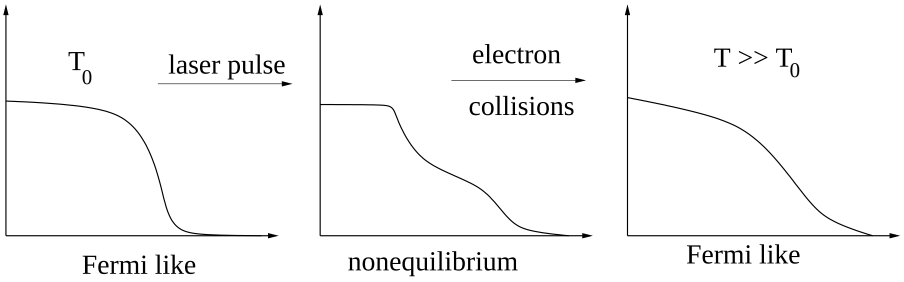

Figure 2.2: Laser induced changes in the electronic distribution. From the ground state (electron temperature T_0) to the excited states (electron temperature T), a non-equilibrium state is created followed by a rapid thermalization process at a higher temperature $T >> T_0$.

difficult problems to face when constructing theoretical models to study laser-matter interaction. This is because many physical processes can be expected depending on the nature of the materials which are treated. Up to now there is no single model which can be used to describe all the physical phenomena resulting from femtosecond laser excitation of solids.

Recently, a theory using the two-temperature molecular dynamics model, which takes into account the electron dynamics has been developed for metals [IZ03]. Although this improved method works well for metallic systems, it is not suitable for all the materials. First principle methods have been also used by Parrinello and coworkers [GMCP89, SAPF96b, VGCC96]. These methods are mainly based on the treatment of ions and electrons with density functional theory in the local density approximation. Within these models, an instant creation of electron hole plasma is assumed at time $t = 0$ so that the duration of laser pulse is set to zero ($\tau = 0$). The first principle methods do not allow an explicit time-dependent treatment of the laser parameters. These methods would not permit a study of materials in a range of laser intensities and durations. Moreover, models based on first principle molecular dynamics simulation, are limited by the fact that they are computationally expensive and therefore do not permit to study systems with large number of atoms.

Thus, there is a need to develop methods which allow to explicitly include the different laser parameters (duration, intensities, fluences) to study the interaction of ultrashort laser with solids. An appropriate theory would also permit to handle the electronic non-equilibrium states.

The basis approach used in the present study, is inspired from the pioneer works of Stampfli and Bennemann [SB90, SB92, SB94] and the recent works of Jeschke and Garcia [JG, GJ03, RGV^{+}05]. The method proposed by Stampfli and Bennemann was very successful on describing the laser-induce lattice destabilization of covalent systems silicon, carbon and germanium. The approach consist of analyzing the instabilities caused by the presence of hot electron plasma in terms of one or two phonons degrees of freedom by assuming that the entropy of the excited electrons remains constant during and after the laser excitation. Later on Jeschke and Garcia proposed an improvment of the model. The proposed model is based on tight binding molecular dynamics, thus the lattice dynamics is described in real space. They used Born Oppenheimer approximation for the simultaneous integration of the equations of motion of electrons and ions. An explicit time-dependent treatment of the electronic occupation changes due to the laser excitation has been introduced. It allowed to explicitly handle the time-dependent laser parameters (pulse duration, intensity, absorbed energy), and study the effect of the variation of those parameters on the dynamics of the lattice.

Although the basic approach remains the same for the description of the electronic non-equilibrium states, the way to compute the potential energy surface which governs the dynamics is different from a particular system to another (depending on the type of electronic structure, we have to deal with). Thus, the previous theoretical works need to be extended for the study of particular systems. We propose here different approaches to study the dynamics of cerium, samarium sulfide, bismuth and germanium upon femtosecond laser irradiation. An overview of each of the different theoretical models employed is given in the next sections.

2.2 Strongly correlated materials: Ce and SmS

Strongly correlated solids are characterized by the presence of incomplete f and d electron shells which mainly determine their physical properties. Among these materials cerium and samarium sulfide attract our attention because of their unique properties. For these elements, the conflict between the valence $s - d$ electrons and the localized f states leads to fascinating physical properties including Kondo behavior [AM82] as well as the unconventional volume collapse phase transition which involves also electronic, optical and magnetic properties changes [JNM70].

Before coming to the discussion concerning the possibility of using femtosecond laser pulse to induce such transition, we review the different theoretical models proposed to give physical explanation of the transition.

2.2.1 Theoretical background

In this subsection we address the old questions regarding the physical origin of the volume collapse phase transition observed in cerium and samarium sulfide. We mention different theoretical models proposed so far, for the description of the phase transition. Although in all the previous models the transition is attributed to the behavior of the 4f electrons, the physical interpretations diverge in how the electronic properties are specially affected during the transition. Among these previous theories the two main microscopic description of the problem are the promotional Falicov model **PM** [RF71] and Kondo volume collapse model **KVCM** [AM82].

In the Falicov picture [RF71], there are two main distinguishable states: one where $4f$ shell is almost empty while the valency is almost 4 and the second where $4f$ shell is occupied while valency is almost 3. This single $4f$ electron play a dominant role in the properties of cerium, it is the most important parameter. On the basis of the **PM**, the removal of the $4f$ electron has as consequence that the nucleus is less screened and then $5d$ and $6s$ orbitals collapse causing an atomic volume reduction. In the spirit of the **PM** the $4f$ level moves from below the Fermi level in the $\gamma \rightarrow \alpha$ transition, consequently the electronic occupation changes $4f^16s^25d^1 \rightarrow 4f^06s^25d^2$. The $4f$ state is closed to Fermi level and the energy needed to promote an electron is of the order of energy gained by the phase transition. In this model the relevant energy scales are the interaction energy between $4f$ states and valence states, and the $4f$ band width. Ramirez and Falicov [RF71] include a Coulomb interaction term G (see below section 2.2.2) between the $4f$ and conduction band states. The Coulomb interaction term plays a major role in the transition. It acts to lower the free energy and can compete with the free energy when electrons raised from the Fermi level to the $4f$ level during the $\alpha \longleftrightarrow \gamma$ phase transition. Unlike to the model proposed by Ramirez and Falicov, which does not account for the hybridization or mixing between states, Alascio et al. [AGL71, ALO73] included the hybridization in their model and showed that the partial occupation found from experiments [GMR69, KLL80, AOL$^+$81, AOL$^+$82] of the $4f$ level, can be explained within this model. In the model proposed by Alascio et al., the introduction of the hybridization leads to a broadening of the f level so that the low energy part lies below the Fermi level. However strong indications are arguing against these promotional type models. In fact recent photoemission experiments show that unlike to the promotional type models the $4f$ state is not close to the Fermi level. They place the $4f$ level at roughly 2 eV in the γ phase, meaning that the energy required to excite $4f$ electron to the conduction band is higher compared to the energy needed to compress the high volume γ phase to the low volume α phase.

The common point of the promotional type models is the fact that they explain the transition from a transition of electron from the localized f state to the delocalized s d band states. As described below these models can be used for a qualitative description of cerium and give satisfactory agreements with the experimental phase diagram. In contrast to the promotional type models cited so far, the other models consider the interaction between the localized f states and conduction band states as the most important ingredient for the transition.

A second theoretical approach of the transition is the so called Kondo volume collapse model (**KVCM**) proposed by Allen and Martin [AM82, AL92]. In the **KVCM** the change in $4f$ occupancy is in principle small. The model involves the spin degrees of freedom and both phases are characterized by a near $4f^1$ configuration. Within the model it is assumed that the transition is as a result of a change in the conduction electron screening of the $4f$ electron which is considered to be localized in both phases. In fact Allen and Martin [AM82] showed that the difference in the both phases is in the magnitude of the on-site exchange interaction between localized $4f$ spins and the conduction electron spins. As the volume decreased in the α phase the hybridization, and hence exchange interaction increase. Thus in the spirit of **KVCM** [AM82] the α phase is characterized by a state where the exchange interaction (coupling constant) is large and each $4f$ spin is engaged in a strongly bonded singlet together with one of the valence electron while the γ phase is characterized with a weak coupling constant.

A third model, the so-called Mott transition model **MTM**, was proposed by Johansson [Joh74]. This model was the first one which did not described the transition to a promotion of an electron from the $4f$ state to the conduction band state. In fact, in this model the $4f$ electron retains its $4f$ character. The nature of the $4f$ states changes from local non-bonding in the γ to itinerant bonding in the α phase, thus $4f$ electron is described by classical band theory in the α phase of cerium for example. In the Mott transition picture the transition is explained as follows: localized $4f$ states in the high volume γ phase become delocalized in the lower volume α phase. The relevant energy scale within this model is the Coulomb repulsion term U between $4f$ electrons in a given atom. The value of U determines the transition between localized behavior and band behavior. Therefore the transition occurs if the coulomb interaction between f electrons in the same atom, is in the same order of magnitude as the $4f$ band width. Johansson showed that the intra atomic Coulomb interaction is $3 - 4eV$ and the $4f$ band width is $\sim 1eV$ which is in contrast to the promotional type picture.

The last method used for the description of the volume collapse transition is the local density approximation in the framework of density functional theory (DFT). The DFT emerged as an efficient and suitable method to describe properties of many systems. In the case of cerium a comparative study using both LDA and LDA+U methods [SPL00, SFL98] showed that the γ phase of cerium is well described by LDA+U method while the α phase is better described by LDA method. This is due to the localized nature of the $4f$ electron in γ phase of cerium and its itinerant behavior in the α phase.

Despite the different interpretations in how the transition occurs and how it affects the electronic properties of the materials, all the theories described above agree in the fact that the $\gamma \rightarrow \alpha$ transition is accompanied by a change in the electronic properties and hence change in volume. At low temperatures the average volume reduction varies from 12% to 17% depending on the applied external pressure.

In the present work we used the qualitative description proposed by Falicov. This qualitative model described well the observed phase transition in cerium under certain thermodynamics conditions (see below sec. 3.1.1). And based on this, we studied the structural properties of cerium upon femtosecond laser excitation.

2.2.2 Falicov model: electronic Hamiltonian

The calculations were done in the framework of the model proposed by Falicov and Ramirez [RF71], which is based on the existence of two possible and qualitatively different states for the electrons: the localized f electronic states (ionic like states) and the itinerant d-band electronic states, coupled via an effective intra atomic Coulomb repulsion G. The volume collapse transition is then described by a delocalization of the electrons through a promotion of electrons from the $f-$ to the 4d-$states$.

It is important to point out that more recent theories are able to account for more degrees of freedom than the promotional model and describe the alpha-gamma transition as an entropy driven process [LED^{+}05, ABGA06]. Both the non magnetic ($\alpha - phase$) and magnetic ($\gamma - phase$) phases are interpreted respectively as pure Kondo phases with high and low Kondo temperature T_K [AM82, AL92]. According to the modern descriptions not the occupancy of the f-electrons but its spectral weight shifts as the temperature is raised due to the unlocking of the Kondo state [HOSK05]. The most important fact is, however, that the volume collapse transition is accompanied by electron delocalization, as one would intuitively expect. The delocalization manifests itself by an increase of double occupancies in the d-orbitals [HMS01].

The above mentioned improvements certainly contributed to obtain a more accurate picture of the electronic properties and, in particular, of the excitation spectrum of Ce at low temperatures. However, and concerning the equation of state $p(VT)$, the promotional model still yields correct results. Therefore, it also reproduces the values of the sound velocity and mechanical properties of Ce with reasonable accuracy. Since our calculations are based on these quantities, we expect our results to give a correct qualitative description of the laser induced phenomena in Ce.

Note also, that the Kondo effect has been shown to be important for a quantitative description of the transition in thermodynamical equilibrium. However, in the case of laser induced transitions the electronic temperature (T_{el}) generated by the excitation is far above the Kondo temperature of Ce (T_K). Therefore, effects involving much lower energy scales compared to the absorbed energy can be neglected.

The electronic Hamiltonian is given by sum of three different terms:

$$H = \sum_k \epsilon_k d_k^+ d_k + G \sum_i f_i^+ f_i d_i^+ d_i + \epsilon_f \sum_i f_i^+ f_i \tag{2.1}$$

with d_k^+,d_k being the creation and annihilation operators for $s-d$ electrons in the conduction band states with energy ϵ_k. f_i^+,fi are the creation and annihilation operators for a f state electron at the lattice site i, with binding energy ϵ_f. A double occupancy of the localized f state is excluded. The first term in the Hamiltonian is the contribution to the energy coming from the itinerant conduction electrons. The second term represents the on-site Coulomb interaction between localized f states with number density $n_f = (1/N)\sum_i f_i^+ f_i$, and the $s-d$ band electrons with number density $n_c = (1/N)\sum_i d_i^+ d_i$, where N is the total number of atoms. Finally, the third term refers to the energy of localized f electrons (ionic energy).

If the system is in thermodynamical equilibrium it is straightforward to obtain the equation of state from the Helmholtz free energy, including the contributions from the electrons and the ions. For the calculation of thermodynamic properties upon femtosecond laser excitation we propose the following model presented below.

2.2.3 Model for laser heating of cerium

As mentioned in the previous sections, a femtosecond laser induce in the material an extreme non-equilibrium state in which the electron and lattice temperatures differ dramatically. The formation of this state can be qualitatively understood as follows. First, electrons gain a large amount of energy due to the absorption of photons. As a consequence, a non-equilibrium (non Fermi-like) electron distribution is produced (see figure

2.2) which, due to electron-electron collisions, thermalizes after a short time to a Fermi-like electron distribution $f(T_{el})$, being T_{el} the electron temperature after laser excitation. Note that T_{el} is much higher than the room temperature, reflecting the laser heating of electrons. Consequently, $T_{el} >> T_{ionic} \simeq T_{room}$, since both laser excitation and electron thermalization occur on time scales which are shorter than typical phonon periods [JG]. Therefore, while the electrons acquire a temperature of a few thousand Kelvin, the ions remain at room temperature T_{room}. The large increase of T_{el} leads to an increase of the electron pressure. As a consequence, the laser excited region tends to expand against the surrounding unexcited part. The resulting expansion dynamics, which determines the laser induced inverse volume collapse transition, is microscopically described in the following.

Using the mean field approximation, the electronic part of the Helmholtz free energy per atom for a given volume V and electronic temperature T_{el} is given by

$$F\left(T,V\right) = F_{conf}\left(T,V\right) + F_{el}\left(T,V\right) + F_{mag}\left(T,V\right). \tag{2.2}$$

Here, the first term F_{conf} refers to the electronic contribution to the ionic configuration, the second one F_{el} accounts for the free energy of the conduction electrons, whereas the last term describes the magnetic free energy. The density of states is assumed to be uniform and normalized in such a way to allow 4 valence electrons in the ground state. The conduction band extends from $-D/3$ to $2D/3$, being $D = 8.16eV$ the band width. The Fermi energy is taken to be zero ($E_F = 0$).

In the ground state, the occupied part of the conduction band has a width of $2.72eV$ while the width of the empty part is $5.44eV$. The electronic part of the free energy can be expressed as $F_{el} = E_{el} - TS_{el}$, with from E_F.

$$E_{el} = \int n\left(\epsilon,V\right) f\left(\epsilon,T_{el}\right) \epsilon d\epsilon \tag{2.3}$$

and

$$S_{el}\left(T_{el},V\right)=\int n\left(\epsilon,V\right)\Big[f\left(\epsilon,T_{el}\right)\,lnf\left(\epsilon,T_{el}\right)\,+ \\ \left(1-f\left(\epsilon,T_{el}\right)\right)\,ln\left(1-f\left(\epsilon,T_{el}\right)\right)\Big]d\epsilon. \tag{2.4}$$

Here, $f(\epsilon,T_{el})$ denotes the Fermi-Dirac distribution and $n\left(\epsilon,v\right)$ the electron density of states. The chemical potential entering in $f(\epsilon,T_{el})$ is computed using that the number of electrons per atom remains constant upon laser excitation, i.e., $n_f+n_c=4$, being

$$n_c=\frac{1}{N}\int n\left(\epsilon,V\right)\;f(\epsilon,T_{el})d\epsilon \tag{2.5}$$

the total number of conduction electrons and n_f the occupation number of f level.The magnetic free energy, second term of Eq(2.2) is written as

$$F_{mag}\left(T,v\right)=-k_BTn_fln\left[2J+1\right]. \tag{2.6}$$

Where $2J+1=6$ is the spin degeneracy and $J=5/2$ the total angular momentum of the localized $4f$ electron.

Finally, the configuration free energy $F_{conf}=E_{conf}-TS_{conf}$ is given by

$$\begin{aligned} F_{ions} &= \epsilon_f n_f - G n_f^2 \\ &- k_BT\left[n_f\,ln\left(n_f\right)+\left(1-n_f\right)ln\left(1-n_f\right)\right]. \end{aligned} \tag{2.7}$$

Here, the first two terms represent the mean ionic energy of the ground state configuration of Ce ions, and n_f the occupation number of the localized $4f$ orbitals. We recall that the f electrons are assumed to be well localized on the ions. The last term refers to the configuration entropy of the localized f electrons, which is given by the different possible distributions of the n_f-electrons on the ions.

In order to describe the lattice expansion dynamics we assume, based on the original idea of Stampfli and Bennemann [SB90, SB92], that on sub-picosecond time scales there is practically no entropy exchange between electrons and ions, and therefore the electronic entropy remains constant,

$$S_{el}\left(T_{el}, V\right) = S_0. \tag{2.8}$$

This assumption is correct as long as only very few degrees of freedom of the lattice become active after laser excitation. For instance, it has been successfully used to determine the dynamics of coherent phonons in Bi [ZTG06a]. In the case of laser excited Ce in the α phase it is reasonable to assume that the motion of the lattice immediately after femtosecond excitation is the expansion, and that other types of lattice motion only become active on later times. Therefore, we rely on Eq. (2.8) and use it to determine the electronic temperature T_{el} as a function of time.

Thus, the excited part of the system will expand through the formation of a shock wave (see below), where the unexcited part will compress. This is shown schematically in Fig. 1. The compression of the unexcited part is not adiabatic, since the whole sample is supposed to be kept at the temperature at which the experiment is performed (for instance room temperature). The electronic pressure which builds up in the excited part as a consequence of the laser excitation is calculated as

$$P = -\left.\frac{\partial E_{el}}{\partial V}\right|_S . \tag{2.9}$$

When the excited part expands the on-site energy of the $f-$orbitals must increase, since the attractive potential of the neighboring ions become less important. We model this fact by writing $\epsilon_f = \epsilon_f^0 + \lambda\left(V - V_0\right)$. ϵ_f^0 is the $f-$level position in the absence of volume changes and λ is an adjustable parameter, which is determined from our choice of ϵ_f^α and ϵ_f^γ. The temperature dependence of the thermodynamic quantities are obtained from the free energy $F(T_{el}, v)$, the $f-$level occupation is computed using [sy96] $n_f = -\frac{\partial F}{\partial \epsilon_f}$. The first step of the simulation is to determine the chemical potential from charge conservation $(n_c + n_f) = 4$. Then, the other thermodynamic quantities $n_f, E, p...$ are calculated. As mentioned before, the sudden increase of the electronic temperature in the laser excited part leads to a rapid increase of the electron pressure. As a consequence, the excited part of the system will expand. Due to the large difference in temperature, entropy and carrier density between the excited and the non excited regions, nonlinear effects are expected to be important and the expansion takes place through the build up of a shock wave. In order to account for this effect we describe the shock wave by using the Rankin-Hugoniot equations, which are derived from the three conservation law (mass, momentum and energy respectively) [GR73].

$$\begin{aligned} \rho\left(u_s - u_p\right) &= \rho_0 u_s \\ P - P_0 &= \rho_0 u_s u_p \\ E - E_0 &= \frac{1}{2}\left(P + P_0\right)\left(V - V_0\right) \end{aligned} \tag{2.10}$$

Here the subscript 0 labels the quantities in the unexcited solid. E refers to the internal energy and ρ_0 to the initial density. Note that the complete process of shock wave propagation in solids can be governed by the above three conservation laws. The combination of these three conservation laws yields the transformation between the kinetic quantities (particle- and shock velocities) and the thermodynamic variables $(P, V.E)$. In the first terms of Eqs. (2.10), u_s and u_p refer to the shock- and the so called particle velocity, respectively. They are related by the equation [GR73].

$$u_s = c_0 + c_1 u_p + c_2 u_p^2, \tag{2.11}$$

where the coefficients c_0, c_1 and c_2 are determined from the experimental data by a least square fitting method, and for the particular case of Ce they are shown in table 2.1. This method for deriving the isotherm in the cold part of the material is based on the analysis of the Hugoniot curve, where the quantities u_s and u_p can be directly measured. Then combining equations (2.11) and (2.10) leads to the relation between

Table 2.1: Fitting parameters using data from [GR73] for $u_p \neq 0$ (see text).

c_0	c_1	c_2
0.6052	2.4765	-0.2292

the applied pressure and particle velocity across the shock front. It is assumed that compression behind the shock line is isotropic, and that the cold part of the material is in thermodynamic equilibrium. The proposed relationship (2.11) is valid in the range of pressure and temperature considered in the present work. The high pressure induced by the laser pulse in the heated region leads, according to Eqs. (2.10), to an increase of the particle velocity. We assume that the particle velocity across the front is equal to the velocity of the material behind the front. In other words, we assume that the expansion velocity of the heated part is equal to compression velocity of the unexcited part. Thus, we evaluate the lattice-volume change in the vicinity of the shock front from the time integration of the particle velocity

$$\delta l = 2 \int_0^t u_p dt \tag{2.12}$$

With a constant total volume, and assuming isotropic expansion, this equation serves to determine the volume change in the expanded material. As already stated above, the shock velocity is derived from pressure by combining Eq. (2.11) and the standard relations of the three law conservation equations. (2.10). Results of the calculations are shown in sec. 3.1.

2.2.4 Density functional theory: LDA+U method

The Density functional theory (DFT) is a quantum mechanical method for the description of electronic structure of atoms, molecules and solids. It has been developed in the 1960s

[HK64, KS65]. Its ability to successfully describe ground state properties of metals, semiconductors, and insulators was well proved. We give here the main aspects of the theory.

The DFT can be seen as a reformulation of a many-body problem in the sense that, instead of solving directly the Schrödinger equation of interacting electrons, the problem is reduced to an electron density dependent of the total energy. Thus the many-body wave function is replaced by the electron density as the basis physical quantity and therefore the problem of N electrons with $3N$ spatial coordinates is reduced to a problem depending only on three spatial coordinates (through the use of the functional of $\rho(r)$ see Eq. 2.15). The theory is based on the Hohenberg-Kohn theorem which states that the ground state energy of a system is an exact functional of the electron density $\rho(r)$. The Kohn-Sham equations [KS65] allow to calculate the electron density which minimizes the total energy. Kohn and Sham have introduced a method based on the Hohenberg-Kohn theorem that enables one to minimize the functional $E_{tot}\left[\rho(r)\right]$ in Eq. 2.15 by varying the electron density $\rho(r)$ over all densities containing N electrons. The method consists of assuming a system with non-interacting electrons moving in an external potential $v_{eff}(r)$. The electron density is obtained by solving the one electron Schrödinger equation

$$\left[-\frac{\hbar^2}{2m}\nabla^2 + v_{eff}\left(r\right)\right]\psi_i\left(r\right) = \epsilon_i\psi_i\left(r\right). \tag{2.13}$$

This eigenvalues equation can be seen as the typical representation of Kohn-Sham equations. Here, ϵ_i is the orbital energy of the corresponding Kohn-Sham orbital ψ_i. The density for an N-particles system

$$\rho\left(r\right) = \sum_i^N |\psi_i\left(r\right)|^2 \tag{2.14}$$

, is derived from these Kohn-Sham equations.

As mentioned above the DFT total energy is a functional of $\rho(r)$ and reads

$$E_{tot}\left[\rho(r)\right] = T\left[\rho(r)\right] + E_{ee}\left[\rho(r)\right] + E_{Ne}\left[\rho(r)\right] + E_{XC}\left[\rho(r)\right] + E_{NN}. \tag{2.15}$$

The first four terms represent the electronic contribution to the total energy which are respectively the kinetic energy of non-interacting electrons (single-electron kinetic energy), the electron-electron repulsion term, the attractive term between nuclei and electrons, and the exchange correlation potential, the last term is the nuclei-nuclei Coulomb repulsion (electrostatic interaction).

While the other terms of the total energy are well known, the exact form of the exchange correlation energy functional E_{XC} is unknown. Its description has given rise to approximations such as the Local Density Approximation (LDA), the Generalized Gradient Approximation (GGA) etc. This exchange correlation energy E_{XC} is the only approximated quantity within the Kohn-Sham density functional theory.

The LDA method is the simplest way to describe E_{XC}. The method consists to consider an homogeneous electron density $\rho(r)$ and express E_{XC} as a functional of $\rho(r)$,

$$E_{XC}^{LDA}\left[\rho(r)\right] = \int d^3r\rho(r)\mu_{XC}\left[\rho(r)\right]. \tag{2.16}$$

A more generalized approach is used for spin polarized systems. This so-called local spin density approximation (LSDA) consists to express the exchange-correlation energy as function of spin density,

$$E_{XC}^{LSDA}\left[\rho(r)\right] = \int d^3r\rho(r)\mu_{XC}\left[\rho_{\downarrow}(r), \rho_{\uparrow}(r)\right] \tag{2.17}$$

with $\rho(r) = \rho_{\downarrow}(r) + \rho_{\uparrow}(r)$ the total density. The LDA methods propose to approximate the total energy of the true electron density by the energy of the local constant density, therefore the method fail in describing more complex systems such as molecule sytems where the electronic density undergoes rapid changes. This lack of accuracy in describing complex systems has led to the development of new and improved functionals. In this regard, an improvement of the LDA and LSDA has been proposed by considering both the gradient of the electron density and the density itself in the evaluation of the exchange-correlation energy. This so-called Generalized Gradient Approximation (GGA) method

[LM88, PW92, PBE96] tends to improve the accuracy of the calculation of the total energy (eq. 2.15). Within this approximation E_{XC} is written as

$$E_{XC}^{GGA}\left(\rho(r)\right) = E_{XC}\left(\rho(r), \nabla\rho(r)\right) = \int d^3r f\left(\rho_{\downarrow}(r), \rho_{\uparrow}(r), \nabla\rho_{\downarrow}(r), \nabla\rho_{\uparrow}(r)\right) \tag{2.18}$$

, where f is an analytical parametrized function. Several parametrization forms exist for the functional $f\left(\rho_{\downarrow}(r), \rho\uparrow(r)_{,}\nabla\rho_{\downarrow}(r), \nabla\rho_{\uparrow}(r)\right)$ [PW92, CVJ$^+$92, PBE96].

The approximations described above to calculate E_{XC} have limitations when they are used to study systems with correlated electrons (f- or d- electrons) e.g. rare-earth compounds (i.e. SmS, SmTe etc.) or some transition metal oxides. For this reason, a method which incorporates the Hubbard-type Hamiltonian [Hub74] into the total energy calculation has been used to describe properties of strongly correlated materials. For the practical use of DFT, this so-called LDA+U method was one of the most influential improvement during the last decades [AAL97, PMCL03]. The success of the method comes from the fact that the simple LDA based models do not properly describe strongly correlated systems where d- or f-electrons play a main role. In fact the d- or f-states are close to localization and the Coulomb interaction between these electrons within an open shell is of a completely different nature than in homogeneous electron gas, upon which LDA and GGA are based. With the LDA+U approach the Coulomb interaction can be handled in the total energy calculation. However this consideration of the strong Coulomb interaction between electrons in the LDA+U framework leads to some ambiguities in the total energy calculation. This comes from the fact that within LDA all the electron interactions are already incorporated in a mean field way in the total energy calculation, and the Hubbard Hamiltonian [Hub74]

$$H = \sum_{ij\sigma} t_{ij} c_{i\sigma}^{+} c_{j\sigma} + U \sum_{i} n_{i\uparrow} n_{i\downarrow} \tag{2.19}$$

also takes into account a large part of the total Coulomb energy of the system. Here, $c_{i\sigma}^{+}$ and $c_{j\sigma}$ are respectively the creation and annihilation operators, t_{ij} the hopings between site i and j. U is the Hubbard parameter and $n_{i\uparrow}, n_{i\downarrow}$ are respectively the spin up and down occupation numbers. Thus, the combination of LDA and Hubbard Hamiltonian leads to a surplus of energy because of the double counting of the Coulomb energy term

$$E = U \sum_i n_{i\uparrow} n_{i\downarrow}. \tag{2.20}$$

Thus, there is a need to identify the surplus in the DFT total energy which are already included in the Hubbard Hamiltonian and subtract them. This task is not obvious if not impossible, since the DFT total energy is formulated in terms of the total electron density and the Hubbard Hamiltonian in the orbital representation. A direct link between the two representations is not possible. The efficiency of the LDA+U method depends on the choice of the model used to avoid such double counting of the Coulomb energy. As mentioned above the double counting comes from the LDA method used to describe the exchange correlation term in Eq. 2.15. In fact the LDA method introduces an unphysical self-interaction of a particle with itself (In principle, an exact density functional for the total energy calculation do not need such correction because orbitals do not self interact). An exact parametrized functional of E_{XC} would then have a self interaction part which would exactly cancel this self interaction term in the total energy (Hartree part of the total energy which contains the mean field interaction energy of an electron with itself). This self interaction term can be neglected for systems with broad bands where the electrons are in Bloch states. However, for strongly correlated materials (with localized states as $4f$ states in SmS), the scenario is different and the self interaction correction (SIC) must be seriously considered.

In the present work we followed the PBE method [PBE96] as implemented in wien2k code [BSM^{+}01] to subtract the self interaction energy from the DFT total energy of SmS.

2.3 Coherent $A_{1\mathrm{g}}$ phonons in bismuth

2.3.1 Structure of bismuth: Peierls distortion

The atoms in bismuth are located on positions near the vertices of a distorted simple cubic lattice. At low temperatures bismuth crystallizes in $A7$ structure. The unit cell of bismuth contains two atoms which are separated non-equidistantly along the hexagonal $c_3 - axis$ due to a Peierls instability (see figure 2.3.1). Consequently, we assist to the presence of a double-well potential along this hexagonal $c_3 - axis$ we describe as the Z axis in the present work. The magnitude of the Peierls displacement can be derived from the atomic coordinate z, which is usually expressed as a fraction of the hexagonal lattice parameter $c = 11.8$ Å. A value of $z = 0.25$ indicates no Peierls distortion. In the ground

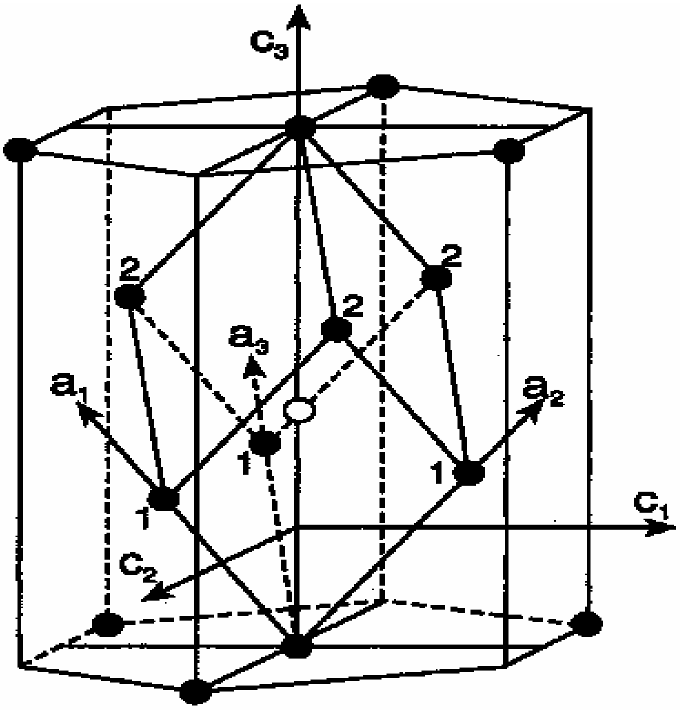

Figure 2.3: A7 structure of Bismuth with two atoms in the unitcell. In the A_{1g} phonon mode the atoms move in the direction of the c_3 axis labelled as z in the text.

state $z = 0.234$, which means that atomic planes are displaced by 0.19 Å in alternating directions. The coordinate z is perhaps the most important parameter here, because it is associated to the A_{1g} phonons. These phonons can be excited by a femtosecond laser pulse and can, for example, be detected through induced changes in the isotropic reflectivity. As we will see below, the A_{1g} phonon frequency is proportional to the second derivative of the potential energy curve along the z direction.

2.3.2 Calculation of the total energy

We computed the total energy of bismuth with the all-electron full-potential linearized augmented plane wave (LAPW) computer program WIEN2k [BSM$^+$01]. This implementation of density functional theory (DFT) [HK64, KS65] has been designed to provide accurate results, which validity depends on no other approximation than the local density approximation [PW92]. Details of our calculations are as follows. In our basis set we included LAPW's with energies up to 18.9 Ry. Atomic spheres around the Bi atoms had radii of 2.3 a_0. Inside the atomic spheres we used a combination of augmented plane waves and local orbitals (APW+lo) [SNS00, MBS$^+$01] to describe the $5d$, $6s$, and $6p$ states. The augmentation energies for these APW+lo's were -1.237, -0.274, and 0.262 Ry, respectively. In order to achieve a further reduction of linearization errors we employed additional $6p$ and $6d$ local orbitals [Sin91] with energy parameters of 2.262 and 0.142 Ry, respectively. We treated spin-orbit coupling self-consistently in a second variational procedure [Sin94], where we used the scalar relativistic eigenstates up to 10 Ry as a basis for the relativistic calculation. We sampled the entire Brillouin zone with 32768 $\mathbf{k}$ points using temperature smearing ($T_e = 1$ mRy).

2.3.3 Effect of laser excitation

To describe bismuth after laser excitation we have used the following physical picture: The laser pulse creates electrons and holes, which undergo dephasing and collisions on a timescale that is much shorter than the typical time of ionic motion (~ 300 fs, based on the $A_{1\mathrm{g}}$ phonon frequency). Therefore one can for all practical purposes assume that the excited carriers thermalize instantaneously. In other words, we simulated the effect of the excitation by an ultrashort laser pulse by heating the electrons. In our calculations the electronic temperature T_e ranged between 1 mRy for the electronic ground state and 28 mRy (4.4 10^3 K) for the highest excited state. Here we wish to mention, that we have used the microcanonical ensemble for the electrons (there is no heat bath). This means that the electronic entropy S_e, not the temperature T_e, was a constant of motion. The atomic z coordinate of bismuth was treated as an external parameter.

In practical computations, we have calculated the total energies at elevated electronic temperatures T_e (corresponding to constant values of the entropy S_e) using

$$E_{\mathrm{tot}}(T_e) = E_{\mathrm{tot}}(\mathrm{gs}) + \Delta E_{\mathrm{band}}, \tag{2.21}$$

where $E_{\mathrm{tot}}(\mathrm{gs})$ is the self-consistent total energy of the electronic ground state and $\Delta E_{\mathrm{band}} = E_{\mathrm{band}}(T_e) - E_{\mathrm{band}}(\mathrm{gs})$. This approach is based on the interpretation of the Kohn-Sham energies [KS65] as single-electron excitation energies. In standard temperature-dependent DFT [Mer65] the electronic occupation numbers are incorporated in the self-consistent cycle to take into account possible screening effects. We have also performed such calculations, assuming that the local density approximation of [PW92] is still valid at high temperatures.

2.3.4 Parametrization of the potential energy surface

We fitted our total energies, which we computed on a fine grid of z values ($z = 0.2250$, 0.2251, $\cdot$ and for 28 different electronic entropies (The entropies were chosen in such a way that $T_e = 1, 2, \cdots, 28$ mRy at $z = 0.2341$) to a function of the form

$$V(z, E_0) = E_0 + 4373.0\,\nu^2(z - z_{\mathrm{eq}})^2 + \gamma(z - z_{\mathrm{eq}})^3 + \delta(z - z_{\mathrm{eq}})^4 + \epsilon(z - z_{\mathrm{eq}})^5, \quad (2.22)$$

where E_0 was entropy dependent (a different value has been allowed for each electronic entropy) and the parameters ν, z_{eq}, γ, δ, and ϵ depended implicitly on the electronic entropy through E_0 via the following relations:

$$\nu = \nu_0 + \nu_1\,E_0 + \nu_2\,E_0^2 + \nu_3\,E_0^3 + \nu_4\,E_0^4 + \nu_5\,E_0^5 \quad (2.23)$$

$$z_{\mathrm{eq}} = z_0 + z_1\,E_0 + z_2\,E_0^2 + z_3\,E_0^3 \quad (2.24)$$

$$\gamma = \gamma_0 + \gamma_{1/2}\,E_0^{1/2} + \gamma_{3/2}\,E_0^{3/2} \quad (2.25)$$

$$\delta = \delta_0 + \delta_1\,E_0 + \delta_2\,E_0^2 + \delta_3\,E_0^3 \quad (2.26)$$

$$\epsilon = \epsilon_0 + \epsilon_{1/2}\,E_0^{1/2} + \epsilon_1\,E_0 \quad (2.27)$$

where E_0 was shifted by a constant to make it zero for the electronic ground state calculation. The symbols in the above equations have the following physical meaning and units: ν is the harmonic $A_{1\mathrm{g}}$ phonon frequency in THz, $V(z, E_0)$ is the total energy in mRy/atom, and z_{eq} is the quasi-equilibrium value of the atomic z coordinate of Bi (see section 2.3.1). γ, δ, and ϵ describe the third, fourth, and fifth order anharmonicity of the potential [see equation (2.22)]. E_0 is the total energy at the minimum of a constant-entropy curve, which can be interpreted as the energy absorbed from the laser.

Whereas this interpretation is exact for relatively long laser pulses, which heat Bi adiabatically, the error is never more than $\approx 5\%$ of E_0, even in the limiting case of an extremely short laser pulse that deposits an energy of $E_0 = 10.5$ mRy/atom, which is the

Table 2.2: Best-fit parameters.

Parameter	Fitted value	Parameter	Fitted value
ν_0	2.98316	ν_1	-0.146079
ν_2	0.0219823	ν_3	-0.00407929
ν_4	0.000370427	ν_5	$-1.27975\,10^{-5}$
z_0	0.234416	z_1	0.00047797
z_2	$-3.79899\,10^{-6}$	z_3	$3.51079\,10^{-7}$
γ_0	-0.698865	$\gamma_{1/2}$	-0.197901
$\gamma_{3/2}$	0.00845577	δ_0	-31.8839
δ_1	0.914822	δ_2	0.16485
δ_3	-0.0103825	ϵ_0	-1.30737
$\epsilon_{1/2}$	1.0219	ϵ_1	-0.176243

maximum value of E_0 for which our fit is still valid. Therefore, in the present work we have used this interpretation. We wish, however, to stress that it is not complicated to compute corrections to the absorbed laser energy for short pulses using equation (2.22). In summary, we fitted 6468 computed data points to a function with 48 free parameters [28 values of E_0 plus the 20 parameters of equations (2.23)–(2.27)]. Our best-fit parameters are summarized in table 2.2. Together with equations (2.23)–(2.27) they give a closed analytical description of the A_{1g} phonon frequency, the quasi-equilibrium value of the atomic coordinate, and the third, fourth, and fifth order anharmonic terms as a function of the energy absorbed from the laser. It is worth mentioning, that the root-mean square of the residuals of our fit was only 0.005 mRy/atom, indicating that our parametrized potential energy surface followed the computed data very closely. For more details of the time dependence of the parametrized potential energy surface, see sec 3.3.1.

2.3.5 Theory of amplitude collapse and revival

A theoretical derivation of the amplitude collapse and revival of wave packets in weakly anharmonic potentials has been given in [AP89]. Here we just mention the main results. (i) Wave packets in a harmonic potential move along classical trajectories. They typically spread, but the spreading is reversible. After one period a packet completely regains its initial shape due to the equidistant character of the spectrum of states. (ii) Anharmonicity leads to a quantum dephasing of a wave packet. The time scale on which this happens can be estimated from

$$T_{\mathrm{rev}} = \frac{2T_{\mathrm{cl}}}{h\left|\frac{\partial \nu_{\mathrm{cl}}}{\partial E}\right|}. \tag{2.28}$$

Here, T_{cl} is the classical period of the trajectory, ν_{cl} is the classical frequency, and E is the expectation value of the energy of the wave packet. Note, that all quantities appearing on the right-hand side of equation (2.28) are classical. For times $t \ll T_{\mathrm{rev}}$, the wave packet behaves essentially classically. (iii) If the anharmonicity is small, the quantum dephasing is reversible. In particular, at $t = T_{\mathrm{rev}}$ the initial wave packet is approximately restored (this is called revival) and at $t = T_{\mathrm{rev}}/2$ the wave packet is shifted by half a classical period (the so-called revival of order 1/2). (iv) In between these revivals, which are phase shifted with respect to each other, the expectation value of the amplitude of the oscillation disappears. This is sometimes referred to as “amplitude collapse of the wave packet”.

The derivation given in [AP89] relies on the discrete nature of the spectrum of states. Therefore, it should be expected that “amplitude collapse and revival” can only be observed in finite systems. In equation (2.28) this becomes apparent if one realizes that ν_{cl} is an intrinsic quantity, which changes little with system size, and that E is an extrinsic quantity, which scales roughly linearly with, for example, the number of atoms in a molecule.

Experimentally, amplitude collapse and revival has unambiguously been observed for electronic wave packets in Rydberg atoms [YMJ90] and for molecular wave packets in small molecules [VVS96]. In addition, the recent experiment on bulk bismuth that we have mentioned in the introduction has also been explained in the same way [MMHK04].

2.3.6 Quantum dynamical simulation method

In this subsection we present the method used to simulate the dynamics of $A_{1\mathrm{g}}$ phonons. We assumed that the displacive excitation of coherent phonons (DECP) [ZVC$^+$91] is the only generating mechanism of the $A_{1\mathrm{g}}$ oscillations in Bi (see [ZTG06a] for a justification of this approximation). The idea behind DECP is that oscillations along the z direction (coherent $A_{1\mathrm{g}}$ phonons) are essentially a consequence of the change in the potential equilibrium position z_{eq} due to the laser excitation. When the pulse duration is short enough (approximately less than half a phonon period) to induce such a change nonadiabatically, the atoms start to oscillate about their new equilibrium positions after the laser pulse. Note that our simulations on time-dependent potential energy surfaces automatically include the phonon generation due to DECP.

For the description of the time evolution of the wave packet ψ which represents the $A_{1\mathrm{g}}$ phonon, we solve the time-dependent Schrödinger equation (TDSE).

$$i\hbar\frac{\partial\psi\left(z,t\right)}{\partial t}=\left[\hat{T}+V\left(z,t\right)\right]\psi\left(z,t\right). \tag{2.29}$$

Where $\hat{T}$ and $V(z,t)$ are respectively the kinetic energy and potential energy operators. Because of the complexity of $V(z,t)$, due to the contribution of the anharmonic terms, only numerical methods can be used to solve the quantum mechanical equation of motion. Several numerical schemes exist to solve such equation. Numerical method based on split operator techniques whose we used in the present work, appears to be the most stable one. The method consist in writing

$$\psi\left(z,t+\delta t\right)=U\left(\delta t\right)\psi\left(z,t\right), \tag{2.30}$$

where $U\left(\delta t\right)$ is the evolution operator (an unitary operator). With a time independent Hamiltonian H the evolution operator $U\left(\delta t\right)$ reads.

$$U\left(\delta t\right)=e^{-iH(\delta t)/\hbar} \tag{2.31}$$

In case of a variable potential, the kinetic energy $\hat{T}$ and the potential energy operators $V(z)$ do not commute, therefore equation 2.31 can be rewritten as

$$U\left(\delta t\right)\approx e^{-i\hat{T}(\delta t)/\hbar}e^{-iV(\delta t)/\hbar}. \tag{2.32}$$

This approximation lies on the Glauber's formula. According to this formula $e^{A}e^{B}=e^{A+B}e^{\frac{1}{2}[A,B]}$, where $[A,B]$ is the commutator. The error introduced in this approximation is $0(\delta t)^2$. This error vanishes in case of constant potential because $\hat{T}$ and V commute(free particle case for example).

One can also reduce this error to $0(\delta t)^3$ by making a symmetric decomposition of the evolution operator $U\left(\delta t\right)$.

$$U\left(\delta t\right)\approx e^{-i\hat{T}(\delta t)/2\hbar}e^{-iV(\delta t)/\hbar}e^{-i\hat{T}(\delta t)/2\hbar} \tag{2.33}$$

As described in subsection 2.3.4 the calculated potential energy $V(z,t)$ is a scalar function in coordinate space, hence the action of the operator $e^{-iV(\delta t)/\hbar}$ on the wave function is only a multiplication of $V(z,t)$ respect to $\psi\left(z,t\right)$. However, the action of the operator $e{-}i\hat{T}\left(\delta t\right)/\hbar$ on the wave packet is less obvious to describe, since the kinetic energy operator $\hat{T}$ is a differential function in coordinate space z. To evaluate its action on the wave function one can utilize the property of the Fourier transform which claims that the differentiation of a function in coordinate space is equivalent to the multiplication of that function's representation in the Fourier space by the conjugate variable k (variable conjugate of the real coordinate z). This means that the kinetic energy operator $\hat{T}$ is a scalar function of the wave vector k in the momentum space ($\hat{T} = \hbar^2 k^2/2m$). Thus, the action of $e^{-i\hat{T}(\delta t)/\hbar}$ can be evaluated in the momentum space using Fourier transform,

$$e^{-i\hat{T}(\delta t)/\hbar}\psi\left(z,t\right) = F^{-1}\left[e^{-i\hbar^2 k^2(\delta t)/2m}F\left[\psi\left(z,t\right)\right]\right]. \tag{2.34}$$

The method used to describe the time evolution of the $A_{1\mathrm{g}}$ phonon coordinate (z coordinate) can be summarized as follows:

First, we constructed two one-dimensional grids, in position and momentum space, where our spatial grid ranged from $z_{\min} = 0.227\ c$ to $z_{\max} = 0.248\ c$, with 1024 grid points. At low temperature (amplitude collapse and revival in Bi has been observed for $T = 10$ K [MMHK04]), only the ground state is occupied. Therefore, a well-defined initial wave packet is formed. This initial state was constructed by solving numerically the time-independent Schrödinger equation on the spatial grid. We obtained the spatial and time propagation of the quantum wave packet using the above split operator technique [FF82], in which one calculates $\psi(z, t + \delta t)$ from $\psi(z, t)$ by applying the propagator $U(\delta t) \approx e^{-i\delta tV/2}e^{-i\delta tT}e^{-i\delta tV/2}$, where V is evaluated at $t + \delta t/2$. We used an extremely small time step of 0.01 fs, which was necessary to properly account for the time dependence of the Hamiltonian. The potential and kinetic operators are diagonal in the position and momentum space, respectively. By going back and forth between our two numerical grids using Fourier transformations the propagator $U(\delta t)$ could efficiently be applied [FF82].

An important point that we have not addressed so far is how the macroscopic size of bulk bismuth affects the quantum simulations of the $A_{1\mathrm{g}}$ phonons. To study this we have introduced a parameter N, which indicates the number of unit cells included in our quantum dynamical simulation. This parameter affects both the initial wave packet and the form of the operators $\hat{V}$ and $\hat{T}$. The case $N = 1$ represents an artificial Bi dimer with exactly the same potential energy surface as bulk bismuth. As this is a finite system, we expected to see clear indications of its quantum nature. To calculate the quantum response of bismuth, we have studied the $A_{1\mathrm{g}}$ oscillations as a function of N, where the bulk limit is obtained for $N \to \infty$. Note that, according to our discussion after equation (2.28), one expects the emergence of classical mechanics as $N \to \infty$. Results are shown in sec. 3.3.

2.4 Theoretical description of laser-excited germanium

As mentioned in the introduction the theoretical model used in the present work to describe femtosecond laser excited germanium is inspired from the works of Jeschke and Garcia [JGB99a, JGB99b, JGB02, JGL$^+$02, JG02] which were based on the original investigations of Stampfli and Bennemann [SB90, SB92, SB94]. The approach used consists to perform molecular dynamics simulation on the basis of a time-dependent potential energy surface derived from a nonorthogonal tight binding Hamiltonian.

2.4.1 Nonorthogonal tight-binding formalism

A realistic simulation method of the physical properties of solids needs to satisfy two main demands: The first demand is the need of accuracy of the theoretical model used, without which the results are meaningless, and the second demand is the need of large system sizes to approach the real systems in nature. The first principle methods although describing accurately the properties of semiconductors, do not satisfy the second demand due to the computational costs. For this reason, the tight binding methods remain good candidates for theoretical study of solids. They give a reasonable description of the inter-atomic interactions and have as advantage this possibility to study relatively large systems. The quantum mechanical nature of the electrons which controls the inter-atomic bonding are taken into account in tight binding approach. In fact the approach keeps the fundamental physics through the quantum description of the electron degrees of freedom in the forces calculation (see sec 2.4.3).

The basis ideas behind tight binding approximation are the followings:

In the spirit of the method the total wave function ψ_m which represents the state of system of N components is given by a linear combination of atomic orbitals $|i\alpha>$ (LCAO method)

$$\psi_m = \sum_{i\alpha} C^m_{i\alpha} |i\alpha> . \tag{2.35}$$

Here i labels the ions and run from 1 *to* N. $C^m_{i\alpha}$ is the occupancy of the $\alpha - th$ orbital located at the $i - th$ site. In the case of nonorthogonal basis ($< i\alpha|j\beta > \neq 0$), the eigenvalues and eigenvectors are obtained from the secular equation:

$$HC = \varepsilon SC \tag{2.36}$$

where H and C are respectively the Hamiltonian and overlap matrix. The matrix elements are

$$H_{i\alpha j\beta} = < i\alpha|H|j\beta > = \int \phi^*_{i\alpha} H \phi_{j\beta} d^3r \tag{2.37}$$

and

$$S_{i\alpha j\beta} = < i\alpha|j\beta > = \int \phi^*_{i\alpha} \phi_{j\beta} d^3r. \tag{2.38}$$

In order to calculate the Hamiltonian and overlap matrix elements, we follow the concept developed by Harrisson and Schilfgaarde [vSH71]. Within this model the effect of nonorthogonality is introduced via a proportional relationship between the overlap and Hamiltonian matrix elements (sec 2.4.2 for details).

Despite its simplicity and the possibility to study system with relatively large number of atoms, the tight binding approximation is usually confronted to a loss of accuracy and transferability when describing complex systems. The main difficulty lies on the parametrization of the Hamiltonian and hence the calculation of the total energy.

2.4.2 Parametrization of the Hamiltonian and overlap

The efficiency of tight binding formalism comes from the fact that the Hamiltonian (and overlap in case of nonorthogonal basis) can be parametrized. This allows to easily extract the electronic structure properties and calculate the inter-atomic forces.

The first parametrization of tight binding Hamiltonian has been formulated by Slater and Koster in 1954 [SK54]. This two-center approximation based model can be seen as the starting point of the investigations of electronic structure of crystalline solids. Later on, in the 1970s tight binding models for total energy calculation have been developed by Harrison [Har] and Chadi [Cha78, Cha84]. The models proposed by Harrison and Chadi were very successful on describing properties of silicon and carbon in tetrahedral bond environment. These first investigations have given rise to a race toward many theories on the orthogonal [SFPO88, GSP89, WHC93, JLMC94, KBW$^+$94] and nonorthogonal [PBF92, FWK$^+$95, MS94b, MS98] formulations of the tight binding approximation.

Our work is based on the the original parametrized model proposed by Menon [MS98] for germanium. We give here a general overview of our model.

Our treatment of bulk germanium containing N atoms is based on the calculation of the total energy, which reads as,

$$U = U_{el} + U_{rep} + U_0. \tag{2.39}$$

The first term U_{el} is the contribution of electrons to the total energy. The second term U_{rep} is the repulsive potential. The third term U_0 is an additional atomic energy which is an arbitrary constant used to shift the total energy value. The repulsive energy is given by

$$U_{rep}\left(r\right) = \sum_{i>j} \phi\left(r_{ij}\right). \tag{2.40}$$

Here, R_{ij} is the inter-atomic distance and $\phi\left(r_{ij}\right)$ a scaling function.

$$\phi\left(r_{ij}\right) = \phi_0 e^{-\beta\left(r_{ij}-d_0\right)}, \tag{2.41}$$

ϕ_0 and β are adjustable parameters and d_0 is the equilibrium bond length.

The attractive part of the total energy U_{el} is less trivial to compute than the repulsive energy which is an analytical function of r_{ij}. In the following, we focus on the calculation of U_{el}.

The attractive part of the total energy U_{el} is the sum over all occupied states. It reads

$$U_{el} = \sum_{m}^{occ} n\left(\varepsilon_m, t\right) \varepsilon_m, \tag{2.42}$$

where $n(\epsilon_m, t)$ is the occupation number at time t of the energy level ε_m. For the calculation of the eigenvalues ε_m, we solved numerically the secular equation 2.36. The overlap matrix was built from the Hamiltonian matrix using the extended Hückel theory [Hof63]. Within this theory, the off-diagonal Hamiltonian matrix elements H_{ij} are related to the diagonal elements of the Hamiltonian and overlap matrix via the proportionality relationship [WH52]

Table 2.3: Electronic parameters used in the present work [Har].

parameters	eV
$V_{ss\sigma}$	-1.73
$V_{sp\sigma}$	1.86
$V_{ps\sigma}$	-1.86
$V_{pp\sigma}$	2.42
$V_{pp\pi}$	-0.78

$$S_{ij} = \frac{2}{K} \frac{H_{ij}}{\left(H_{ii} + H_{jj}\right)}. \tag{2.43}$$

The overlap matrix is therefore directly derived from the Hamiltonian. The coefficient K is the Wolfsberg-Helmholtz parameter [WH52], which is called coefficient for nonorthogonality. For the parametrization of the Hamiltonian and Overlap matrix, we used as previously mentioned the general and transferable parametrization scheme proposed by

Menon [MS98]. Within this method, the matrix elements H_{ij} are derived from the orthogonal matrix elements V_{ij}.

$$H_{ij} = V_{ij}\left(1 + \frac{1}{K} - S_2^2\right) \tag{2.44}$$

where r is the inter-atomic distance and K the coefficient for nonorthogonality which is exponentially r dependent function.

$$K\left(r\right) = K_0 e^{\sigma(r-d_0)^2}, \tag{2.45}$$

with K_0, σ and d_0 adjustable parameters. In our calculation we reduced this exponential function to a constant value $K = K_0$. The other term in equation 2.44 are

$$S_2 = \frac{S_{ss\sigma} - 2\sqrt{3}S_{sp\sigma} - 3S_{pp\sigma}}{4} \tag{2.46}$$

with

$$S_{\lambda\lambda'\mu} = \frac{2V_{\lambda\lambda'\mu}}{K\left(\varepsilon_\lambda + \varepsilon_{\lambda'}\right)} \tag{2.47}$$

and $V_{\lambda\lambda'\mu}\left(r\right)$ the hopping terms,

$$V_{\lambda\lambda'\mu(r)} = V_{\lambda\lambda'\mu}\left(d_0\right) e^{-\alpha(r-d_0)} \tag{2.48}$$

which are also exponentially r dependent. For the determination of the equilibrium hopping elements $V_{\lambda\lambda'\mu}\left(d_0\right)$,

$$V_{\lambda\lambda'\mu}\left(d_0\right) = n_{\lambda\lambda'\mu}\frac{\hbar^2}{md_0^2} \tag{2.49}$$

we used the universal parameters proposed by Harrison [Har], the values are given in tab. 2.4.2.

The other parameters are given in tab. 2.4. With this parametrization of the Hamiltonian and the Overlap matrix, we can easily compute the forces.

Table 2.4: NOTB parameters used in the present work.

ϵ_s (eV)	ϵ_p (eV)	d_0 $\left(\mathring{A}\right)$	α $\left(\mathring{A}^{-1}\right)$	K_0	ϕ_0 (eV)	σ $\left(\mathring{A}^{-2}\right)$
-14.38	-6.36	2.44	1.604	2.92	0.44	0.0

2.4.3 Calculation of forces

One of the most important aspects in all dynamical study of solids is the efficiency to compute the forces acting on atoms. The calculation of forces is the main computational and also the most time-consuming task in case of molecular dynamics simulation (as in the present work). There exist several methods to evaluate the interaction forces. While the repulsive force can be easily computed from a simple analytical derivative of the repulsive energy of Eq. 2.40, the attractive force from the electronic part of the Hamiltonian (see Eq. 2.42) is less trivial to obtain. Here, the attractive force acting on a given atom is computed quantum mechanically through the Hellmann-Feynmann theorem [G32, Fey56].The total force reads

$$F = -\frac{\partial U}{\partial R} = m\frac{\partial^2 R}{\partial t^2}, \tag{2.50}$$

with U the total energy. Since the repulsive part of the total force is calculated by the analytical derivative of the repulsive potential (Eq. 2.40) respect to the atomic position, we only focus on the attractive part. We give here the details of the calculation of F_{att} as implemented in our molecular dynamics TB code.

First of all the generalized linear equation

$$\sum_{j\beta} \left(H_{i\alpha j\beta} - \varepsilon_m S_{i\alpha j\beta}\right) C^m_{j\beta} = 0 \tag{2.51}$$

is solved. With matrix notation this equation becomes

$$\left(H - \varepsilon_m S\right) C^m = 0. \tag{2.52}$$

As H and S are Hermitic we can write

$$C^{n+}\left(H-\varepsilon_m S\right)=0. \tag{2.53}$$

Differencing (2.52) with respect to the atomic position R leads to

$$\left[\frac{\partial}{\partial R}\left(H-\varepsilon_m S\right)\right]C^m+\left(H-\varepsilon_m S\right)\frac{\partial}{\partial R}C^m=0, \tag{2.54}$$

then

$$C^{m+}\left[\frac{\partial}{\partial R}\left(H-\varepsilon_m S\right)\right]C^m+C^{n+}\left(H-\varepsilon_m S\right)\frac{\partial}{\partial R}C^m=0. \tag{2.55}$$

Because of Eq. (2.53) the second term vanishes. By means of the Hellmann-Feynmann theorem [G32, Fey56], we obtain the derivative of the eigenvalues respect to atomic position R

$$\frac{\partial}{\partial R}\varepsilon_m=\frac{C^{n+}\left(\frac{\partial H}{\partial R}-\varepsilon_m\frac{\partial S}{\partial R}\right)C^m}{C^{n+}SC^m}. \tag{2.56}$$

The eigenvectors are normalized,

$$C^{+}SC=1. \tag{2.57}$$

Equation (2.56) can be rewritten in details

$$\frac{\partial}{\partial R}\varepsilon_m=\sum_{i\alpha j\beta}C_{i\alpha}^{n*}\left(\frac{\partial H_{i\alpha j\beta}}{\partial R}-\varepsilon_m\frac{\partial S_{i\alpha j\beta}}{\partial R}\right)C_{j\beta}^{m}. \tag{2.58}$$

The attractive part of the total force acting on atoms is obtained by differencing the attractive energy respect to atomic position,

$$F_{att}=-\frac{\partial U_{el}}{\partial R}=-\sum_m n\left(\varepsilon_m,t\right)\frac{\partial}{\partial R}\varepsilon_m \tag{2.59}$$

here $n\left(\varepsilon_m,t\right)$ is the time dependent eigenvalue occupation. Replacing (2.58) in (2.59) gives

$$F_{att}=-\sum_m\sum_{i\alpha j\beta}n\left(\varepsilon_m,t\right)C_{i\alpha}^{n*}\left(\frac{\partial H_{i\alpha j\beta}}{\partial R}-\varepsilon_m\frac{\partial S_{i\alpha j\beta}}{\partial R}\right)C_{j\beta}^{m} \tag{2.60}$$

and

$$F_{att}=-\sum_{i\alpha j\beta}\left(\frac{\partial H_{i\alpha j\beta}}{\partial R}A_{i\alpha j\beta}-\frac{\partial S_{i\alpha j\beta}}{\partial R}W_{i\alpha j\beta}\right), \tag{2.61}$$

where

$$A_{i\alpha j\beta} = \sum_m n\left(\varepsilon_m, t\right) C^{n*}_{i\alpha j\beta} C^{m}_{i\alpha j\beta}, \tag{2.62}$$

and

$$W_{i\alpha j\beta} = \sum_m \varepsilon_m n\left(\varepsilon_m, t\right) C^{n*}_{i\alpha j\beta} C^{m}_{i\alpha j\beta} \tag{2.63}$$

are respectively the matrix density and the energy weighted matrix density elements. Technically, this calculation is an intensive computationally task in terms of time and memory since it is achieved at every time step. For instance, in our pairwise interacting system of N atoms, if we consider only the first neighbors contribution to the force we must evaluate $N \times (N-1)$ pair distances which means that the time needed to evaluate the forces scales as N^2. However some tricks (i.e Verlet list [Verb], Cell lists [HE] etc.) can be used to reduce such computational time to a scaling factor of N (see sec. 2.4.5). Although the physical description of the electronic properties of the excited and non-excited bulk germanium differ, the computation of the forces described in this subsection remains the same.

2.4.4 Absorption of laser energy

As emphasized in sec. 2.1 the laser pulse interacts primary with the electrons which thermalize very quickly. The time dependent many-body potential which governs the dynamics of the system, is derived from the single electronic Hamiltonian

$$H = \sum_{i\alpha} \epsilon_{i\alpha} n_{i\alpha} + \sum_{ij\alpha\beta j\neq i} V^{\alpha\beta}_{ij}(r_{ij}) c^{+}_{i\alpha} c_{j\beta}. \tag{2.64}$$

Here, $\epsilon_{i\alpha}$ is the on-site energy of atom i and orbital α (s,p orbitals). The values of ϵ_s and ϵ_p are given in table 2.4. $c^{+}_{i\alpha}$ and $c_{j\alpha}$ are the creation and annihilation operators, and $V^{\alpha\beta}_{ij}(r_{ij})$ the hopping integrals. We assume that the valence electrons of germanium can be described by this effective single-particle Hamiltonian. The parametrized functions of the Hamiltonian and overlap matrix elements are presented in sec. 2.4.2. Note that the Hamiltonian and overlap matrix elements depend on the inter-atomic distances r_{ij}. Thus, the solution of the secular equation 2.36 yields to M eigenvalues ϵ_m which depend on $\{r_{ij}\}$. For the coupling between laser energy and electrons we assume that the time-dependent potential energy surface $U(\{r_{ij}\},t)$ which governs the motion of the atoms is equal to the free energy of the electrons $F_{\text{el}}(\{r_{ij}\},t)$, which is given by

$$\begin{aligned} U(\{r_{ij}\},t) &= F_{\text{el}}(\{r_{ij}\},t) = \sum_m n(\epsilon_m,t)\epsilon_m + \\ &\quad + U_{\text{rep}}(\{r_{ij}\}) - T_{\text{el}}(t)S_{\text{el}}(t), \end{aligned} \tag{2.65}$$

where $n(\epsilon_m,t)$ are the occupations of the corresponding electronic levels ϵ_m. This assumption is based on the fact that electron thermalization is very fast compared with the time scale for the motion of the ions. As described in sec. 2.1, the rapid thermalization of electrons is justified for laser pulse intensities that excite significant percentage of the valence electrons ($> 8\%$ for Ge). As consequence of the strong excitation the system undergo rapid bond breaking and structural changes. Due to the presence of the laser pulse, these occupations are time-dependent. The first term of Eq. 2.65 represents the attractive contribution from the valence electrons. The second term is the repulsive part of the potential energy (described in eqs. 2.40 and 2.41). The third term contains the electronic temperature T_{el} and the electronic entropy S_{el}, which is given by

$$\begin{aligned} S_{\text{el}} &= -k_B \sum_m \left[n(\epsilon_m,t) \log\left(n(\epsilon_m,t)\right) \right. \\ &\quad \left. + \left(1 - n(\epsilon_m,t)\right) \log\left(1 - n(\epsilon_m,t)\right) \right]. \end{aligned} \tag{2.66}$$

Eq. (2.65) represents a generalization of the Born-Oppenheimer approximation (BOA). Note that the usual BOA is recovered for $T_{\text{el}} = 0$.

It is important to point out that the functional dependence of $U(\{r_{ij}\},t)$ on the inter-atomic distances $\{r_{ij}\}$ is strongly dominated by the electronic occupations $n(\epsilon_m,t)$ present in the first and third terms of Eq. 2.65. Therefore strong changes in electronic occupations yield to strong modifications of the potential energy landscape $U(\{r_{ij}\},t)$.

From the above points it comes out that, it is essential to take into account explicitly the time-dependent change of electronic occupation $n\left(\epsilon_m, t\right)$ for the description of laser induced structural effects. Here, we use the approach proposed by Jeschke and Garcia [JG, JDG09] to introduce the time dependent change of electronic occupation. This approach gives a good description of laser induced structural changes in diamond, graphite and silicon [JGB99a, JGB99b, JGB02, JGL$^+$02, GJ03] and also in carbon nanotubes [DGJY04, RGV$^+$05]. We give here the details of the approach combined with our NOTB method to study laser excitation of bulk germanium.

In order to obtain an equation for the rate of change of the electron occupations $n(\epsilon_m, t)$ we consider the equation of motion for the density matrix $\hat{\rho(r)}$, which reads

$$\dot{\hat{\rho}} = -\frac{i}{\hbar}\left[H_{\text{TB}} + V_{\text{laser}}, \hat{\rho}\right] + \left.\frac{\partial \hat{\rho}}{\partial t}\right|_{coll} . \tag{2.67}$$

The first term refers to the coherent motion of the electrons, which is driven by the laser field and which involves optical transitions between the energy levels of the Hamiltonian H_{TB}. Since the tight-binding Hamiltonian is a single-particle one, it does not describe interactions between the excited electrons, which are essential for the thermalization processes. Thus, we treat them by including a second, dissipative term in Eq. 2.67.

Eq. 2.67 represents a system of coupled differential equations for the diagonal and nondiagonal elements of the density matrix. However, since the electron-hole plasma created by the laser undergoes rapid dephasing, the relevant equations of motion will be those describing the diagonal elements. Therefore, neglecting the contribution of the nondiagonal elements one obtains

$$\begin{aligned} \frac{dn(\epsilon_m, t)}{dt} = & \int_{-\infty}^{\infty} d\omega\, g(\omega, t-\tau)\Big\{\left[n(\epsilon_m - \hbar\omega, t-\tau)\right. \\ & \left. + n(\epsilon_m + \hbar\omega, t-\tau) - 2n(\epsilon_m, t-\tau)\right]\Big\} \\ & - \frac{n(\epsilon_m, t) - n^0(\epsilon_m, T_{\text{el}})}{\tau_1} . \end{aligned} \tag{2.68}$$

Here, the first integral describes the laser excitation and creation of a non-equilibrium electron distribution. Eq. 2.68 describes the absorbtion of light from the laser pulse. $g(\omega, t)$ is the intensity function of the laser pulse and is calculated by:

$$g(\omega, t) = I_0 exp\{-\frac{4ln2\,(t-t_0)}{\tau_p^2} - \frac{f\tau_p\,(\omega-\omega_0)^2}{16ln2}\}. \tag{2.69}$$

$g(\omega, t)$ represents the distribution of intensity over time and energies. It is the product of the envelope of the pulse $I\,(t)$ which may be described by a Gaussian function with a pulse duration τ_p and its Fourier transform $I\,(\omega)$.

$$I\,(t) = I_0 exp\{-\frac{4ln2\,(t-t_0)^2}{\tau_p^2}\} \tag{2.70}$$

and

$$I\,(\omega) = \tilde{I}_0 exp\{-\frac{f\tau_p\,(\omega-\omega_0)^2}{16ln2}\}. \tag{2.71}$$

With f a factor depending on the units used for time and energies. In our case $f = \frac{10^{-15}e}{h}$ for time in fs and ω in eV.

The effects of the laser excitation on the electronic system can be described as follows. The electronic distribution is at each time step folded with the intensity function $g(\omega, t)$. This means that at each time step, the occupation of an energy level ϵ_m changes in proportion to the occupation difference with respect to levels at $\epsilon_m - \hbar\omega$ and at $\epsilon_m + \hbar\omega$. Another important simplification which has been made within the approach is to neglect the optical matrix elements in eq. (2.68). They are assumed to be equal to unity. Therefore the band structure plays the main role in the absorption process. This absorption process is illustrated in fig. 2.4. The second term of Eq. (2.68) describes the electron thermalization resulting from electron-electron collisions through a relaxation time τ_1. Thus, with a time constant τ_1, the distribution $n(\epsilon_m, t)$ approaches a Fermi-Dirac distribution $n^0(\epsilon_m, T_{\rm el})$, which is given by

$$n^0(\epsilon_m, T_{\rm el}) = \frac{1}{\exp\{\beta(\epsilon_m - \mu) + 1\}}\,, \quad \text{with } \beta = \frac{1}{k_{\rm B}T_{\rm el}}\,. \tag{2.72}$$

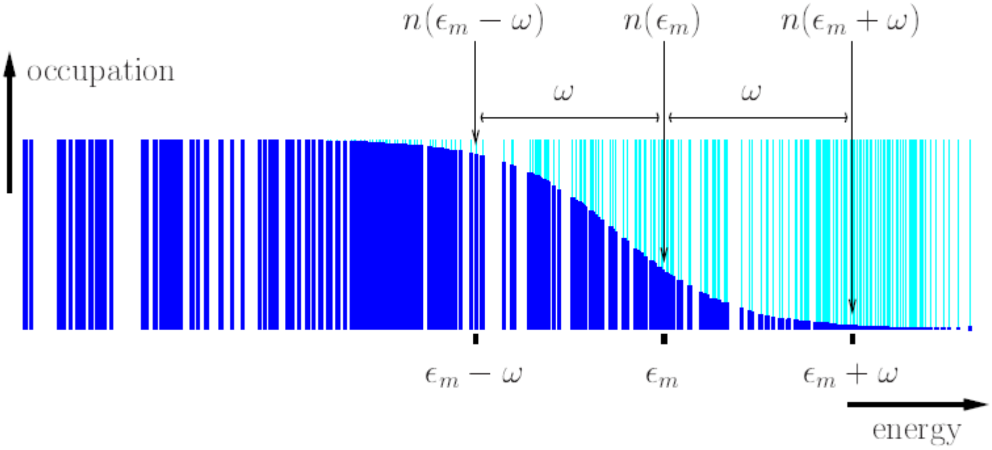

Figure 2.4: Absorption of laser energy. The laser intensity at the frequency ω effects for an energy level ϵ_m an occupation increases from a level at $\epsilon_m - \hbar\omega$ and an occupation decreases toward a level at $\epsilon_m + \hbar\omega$. *Figure reproduced from [JG].*

Here, T_{el} is the electron temperature, and μ is the chemical potential. This simple approach yields good description of laser excited germanium. This is explained by the fact that for dense electron-hole plasmas in covalent solids extremely low relaxation times τ_1 have been found. A carrier thermalization faster than 10 fs in GaAs has been reported [KCL$^+$88]. Even studies that use lower laser intensities than are studied here find thermalization times of the order of 100 fs [ESRL91, WFP$^+$94]. We here use $\tau_1 = 10\ fs$. Note, for these short thermalization time the exact electronic dynamics leading to electronic equilibrium do not play a significant role for the structural changes we are studying here.

The electronic temperature T_{el} and the chemical potential μ, which appear in the Fermi-Dirac distribution and which are not determined by Eq. (2.68), need to be fixed by an additional principle. We will demand that the non-equilibrium distribution $n(\epsilon_m, t)$ approaches the Fermi-Dirac distribution while conserving the total energy of the system. Energy loss mechanisms, which are of course already present as soon as some laser energy has been absorbed, will be treated in a way that does not interfere with this principle of energy-conserving equilibration. The total energy at time t is required to be

$$\begin{aligned} E_{\mathrm{tot}}(t) &= U(\{r_{ij}(t)\}, t) + E_{\mathrm{kin}}(t) \\ &\overset{!}{=} E_{\mathrm{tot}}(t=0) + E_{\mathrm{abs}}(t) - E_{\mathrm{loss}}(t)\,, \end{aligned} \tag{2.73}$$

where $E_{\mathrm{kin}}(t)$ is the kinetic energy of the ions, and $E_{\mathrm{abs}}(t)$ is the energy that has been absorbed from the laser pulse up to the time t. A further, obvious demand which is necessary to determine T_{el} and μ is that the number of electrons N_{e} stays constant over the entire calculation:

$$N_{\mathrm{e}}(t) = \sum_m n(\epsilon_m, t) \overset{!}{=} N_{\mathrm{e}}^0\,. \tag{2.74}$$

Thus, by enforcing conservation of energy during the electron thermalization we make sure that we get physically meaningful results.

With this approach the effect of a laser-induced electronic non-equilibrium on the structural response can be studied. With the help of molecular dynamics technique described in the next subsection we study the structural changes of excited bulk germanium.

2.4.5 Molecular dynamics

Molecular dynamics (MD) simulation is a well established method to study the time evolution of classical and quantum mechanical systems. It allows to provide detailed informations on the structural transformations of a material in a range of time scale over which the changes take place. The key tool of the method is the numerical solution of the equation of motions which are solved for an ensemble of atoms. We discuss here some practical aspects of the MD method.

Originally Molecular dynamics was introduced by Alder and Wainwright in the 1950's to study the interactions of hard spheres [AW57]. From their original work, many interesting results regarding the behaviour of liquid system emerged. Later on the efficiency of MD simulation techniques to study behavior of solids and other complex systems has been proved. The use of MD technique has been facilitated by the availability of powerful computers during the last decades and the simplicity of its algorithm to be implemented. The methodology used to describe the inter-atomic forces in solids can be either empirical or first principle methods, but the MD scheme remains the same. In fact the only difference comes from the electronic contribution to the total energy used to calculate the forces and the subsequent set of dynamical equations to solve. In this work, we used nonorthogonal tight binding (described in sec. 2.4.1) molecular dynamics (NOTB-MD) to study the physical properties of bulk germanium with and without laser excitation. We give here a description of the different steps of our MD scheme.

First of all an initial structure consisting of N particles is assembled, by assigning initial positions for all atoms $\{r_k(t = 0)\}$. The initial structure is usually guided by the nature of the structure that we aim to study. For instance, germanium crystallizes in diamond phase at low temperatures, therefore it is preferable but not necessary to initially place the atoms in a diamond lattice. It is also important to point out that the atoms should be placed in reasonable positions, to avoid significant overlap of the atomic cores.

The second step is to solve routinely the Newton's equation of motion until the properties of the system no longer change with time. The system is therefore equilibrated and the statistical quantities are derived.

In the specific case of simulating laser excited bulk germanium, the system is not necessary in equilibrium state. This yields to some additional physical considerations. For instance, the electronic and ionic motions are treated separately using the Born-Oppenheimer approximation [BOA].

In practice, for a given configuration we first search the electronic ground state and then calculate the potential energy corresponding to that configuration. The motion of ions

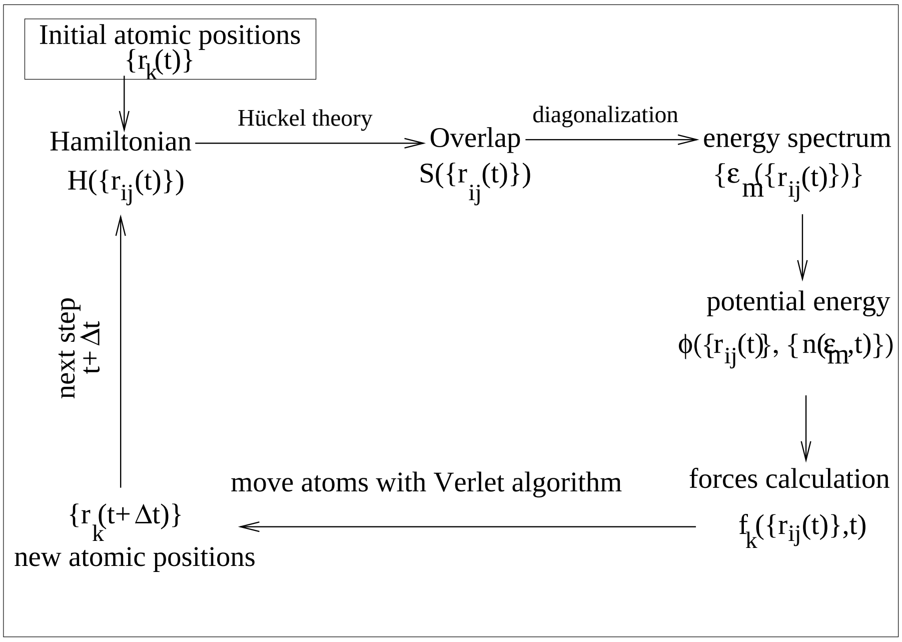

Figure 2.5: Molecular dynamics scheme for the time evolution of the system. Potential energy surface $\phi(\{r_{ij}\}, t)$ which governs the atomic motions is obtained from an electronic Hamiltonian in the basis of nonorthogonal tight binding framework. The time dependent non-equilibrium electronic occupation $n(\epsilon_m, t)$ is taken into account explicitly in the potential energy calculation.

is controlled through the Newton's equation of motion

$$F_i = M_i \ddot{r}_i. \tag{2.75}$$

This differential equation is numerically solved and yields to the time evolution of coordinate and velocity of every atom inside the simulation box.

The main task is to compute the forces acting on atoms. It is computationally expensive in the sense that it involves calculation over all pairs of atoms. For these reason, the time step used to integrate the Newton's equation of motion must be as large as possible while the physical properties of the system are retained. For example, the condition of the conservation of total energy must be fulfilled since we use microcanonical ensemble.

It would be also interesting to have an algorithm that accurately integrate eq. 2.75 and then predicts exactly the trajectory of all atoms in short and long times. Unfortunately, up to now such accurate algorithm doesn't exist. The difficulty comes from the fact that system studied by MD simulation are in regime where the trajectory through phase space depends sensitively on the initial conditions. This essentially means that two trajectories that are initially closed can diverge significantly in time. Therefore one has to consider an algorithm which is able to keep the simulated trajectory as close as possible to the true trajectory expected from the initial conditions. Several algorithms exist in literature. The most used are: *Verlet Algorithm* [Verb, Vera], *Velocity Verlet* [SABW82], Leap-frog Algorithm [HE] and predictor-corrector schemes. Due to the time reversible nature of the Newton's equation, the algorithm used have also to be so. The integration techniques based on predictor-corrector do not ensure this time reversibility and hence can not be used for a proper description of the time evolution of the system. In our simulations we used the Verlet Algorithm in its velocity form (*'velocity Verlet algorithm'*).

The Verlet algorithm in its original form consider the positions r_k at times t and $t - \delta t$ and acceleration $\ddot{r}_k$ at time t to predict the position at time $t + \delta t$ which reads

$$r_k\left(t + \delta t\right) = 2r_k\left(t\right) - r_k\left(t - \delta t\right) + \ddot{r}_k \delta t^2. \tag{2.76}$$

Here, r_k is the position of atom k and δt the integration time step. The *'velocity Verlet algorithm'* [SABW82] computes the atomic positions and velocities as follows:

$$r_k\left(t + \delta t\right) = r_k\left(t\right) + \dot{r}_k\left(t\right)\delta t + \frac{1}{2}\delta t^2 \ddot{r}_k\left(t\right) \tag{2.77}$$

$$\dot{r}_k\left(t + \delta t\right) = \dot{r}_k\left(t\right) + \frac{1}{2}\delta t\left[\ddot{r}_k\left(t\right) + \ddot{r}_k\left(t + \delta t\right)\right] \tag{2.78}$$

From the initial conditions $[\{r_k\}_{t=0}, \{\dot{r}_k\}_{t=0}]$, the time dependent system $\left[r_k\left(t\right), \dot{r}_k\left(t\right)\right]$ is simply obtained by solving routinely eq. 2.75, 2.77 and 2.78. All the atomic degrees of freedom are taken into account, in our real space description of the material.

Another important aspect to emphasize is the size of the studied system. In laboratory experiments, the typical extension of a laser spot is 15 μm and the usual penetration depth is roughly 100 nm. This depends naturally on the studied material and the laser light frequency. The estimation of the excited volume of a material is therefore 7x$10^3 \AA^3$. A typical volume of MD supercell is $10^3 \AA^3$, which means that only a small size of the entire heated part of the material is considered in the simulation. The method used is in fact limited with respect of the number of atoms that can be treated with the available computing power and cost in term of time. In order to handle the system size, it is very common in MD simulation to use periodic boundary condition (PBC). Applying the PBC in the three spatial directions (x,y,z) of the MD cell allows to not only simulate an infinite bulk, but to also eliminate the surface effects (see [JG] for a detailed description of the use of PBC). The complete process of our calculation is illustrated in figure 2.5 and summarized in the next subsection.

2.4.6 Summary of the numerical approach

Our theoretical description of laser induced structural changes in bulk germanium requires to solve in a parallel way the classical equations of motion for the nuclear degrees of freedom (Newton's equations 2.75) and the equations of motion for the electronic occupations [Eq. (2.68)]. The equations of motion are, of course, coupled. Changes in the occupations lead to changes in the potential energy surface $\phi(\{r_{ij}(t)\}, t)$. These lead to changes in the atomic coordinates which cause changes in the eigenvalue-spectrum $\epsilon_m(\{r_{ij}(t)\})$ obtained from the secular equation 2.36 (due to changes of the hopping matrix elements, Eqs. 2.48 and 2.47). Thus the time evolution of the structure is obtained. Results are shown in sec. 3.4.

Chapter 3

Results

3.1 photoinduced structural changes in cerium

Cerium is the most abundant of rare earth metals in nature and the only element in the periodic table with a solid-solid critical point. It can be found in many minerals like allanite, cerite, basnazite etc. Cerium crystallizes in a face-centered cubic (fcc). At ambient conditions it is in its low volume phase named α with a volume reduced to $15 - 17\%$ compared to the high volume phase γ. It exhibits a fascinating iso-structural transition from γ to α phase under certain thermodynamic conditions. This transition which is referred to as $\alpha \longleftrightarrow \gamma$ phase transition is accompanied by a discontinuous volume change [LLC83] (volume collapse transition). In sec. 3.1.1 we describe this volume collapse transition driven by external pressure. In sec 3.1.2 we investigate the inverse phase transition. For this, we study the time dependent volume expansion induced by an ultrashort laser excitation using the model described in 2.2.3.

3.1.1 Volume collapse phase transition

To describe the phase transition we have used the qualitative description proposed by Falicov and Ramirez [RF71]. This approach although qualitative allows to describe appropriately the experimentally observed $\alpha\longleftrightarrow\gamma$ phase transition. The calculated isotherms of cerium are shown in figure 3.1.1. At low temperatures ($T < 600K$) and at a given critical pressure depending on the temperature, a discontinuous volume change is observed. According to Falicov's theory, this sudden volume change is due to a discontinuous transition of one electron from the valence states to the $4f$ states. This transition becomes continuous at high temperatures ($T > 600K$).

However at low pressure an intermediate phase named β-phase can be observed. The β phase has an hexagonal close-packed as crystal structure and its electronic structure is similar to that of the γ phase. The β phase is found when γ phase cerium is cooled. This β phase is not yet well established and described. We focus here on the two well described α and γ phases. As shown in figure 3.1.1, the phase boundary between the α and γ phases is an increasing line with increasing pressure and temperature. Up to now

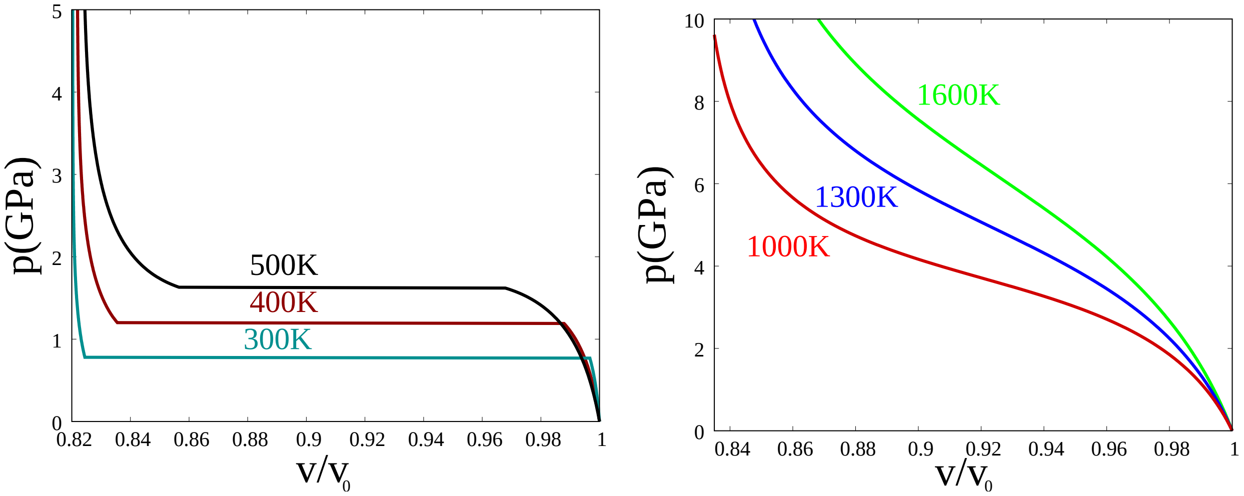

Figure 3.1: Phase diagram p(V) of Ce for different isotherms at high and low temperatures calculated using the promotional Falicov model. Good agreement is obtained with the ab-initio results [LED$^+$05]

it is believed that there are no broken symmetries at the critical points, despite some reasonable doubts which can take place due to some physical reasons. To move smoothly from one phase to another by applying pressure and increasing the temperature, it is not possible that a symmetry is altered. In fact a change in symmetry can not occur in a smooth way and therefore can not take place during such phase transition. Same phase transition from a fcc structure to a distorted fcc structure has also been observed in other systems like SmS.

3.1.2 Laser induced phase changes

In this subsection we analyze the volume changes due to laser excitation and describe the time evolution of the degree of electron delocalization, which we define as

$$\delta = 1 - n_f \tag{3.1}$$

(see sec. 2.2.3). Where n_f is the occupation of the localized $4f$ state. In Fig. 3.3 we show the development of the degree of electron delocalization at different electronic temperature depending on the f level position. As mentioned before, high electronic temperatures correspond to high laser fluences. We have found that the decrease of delocalization of the $4f$ states increases with increasing ϵ_f. The delocalization of the $4f$ electrons takes place continuously in the high volume *gamma* phase. This is consistent to recent DAFT calculations [HMS01]. Since the f-level position will change upon the laser induced expansion, the curve shows that, particularly at high electronic temperatures, no discontinuous transition will occur. This means that for the conditions created by the laser pulse the $5d6s$-$4f$ transition seems to occur continuously. For a sufficiently large value of ϵ_f, no $f-$occupation is expected.

As explained in the section 2.2.3, the time evolution of the system was introduced using the shock wave compression technique. The detailed mechanism of the shock compression of solids has not yet been clarified. However, the shock wave compression technique remains a very important tool to study solids under shock loading. Since solids are incompressible in practical terms, very large pressures are necessary to create even a modest change in volume.

In general, solids do not behave like fluids at low stress due to the presence of shear stress. This means that solids stress and plastic flow may enhance the mechanical changes. This is what we expect to occur upon shock wave formation induced by a femtosecond laser pulse. The increase of the electronic temperature induced by the femtosecond laser pulse

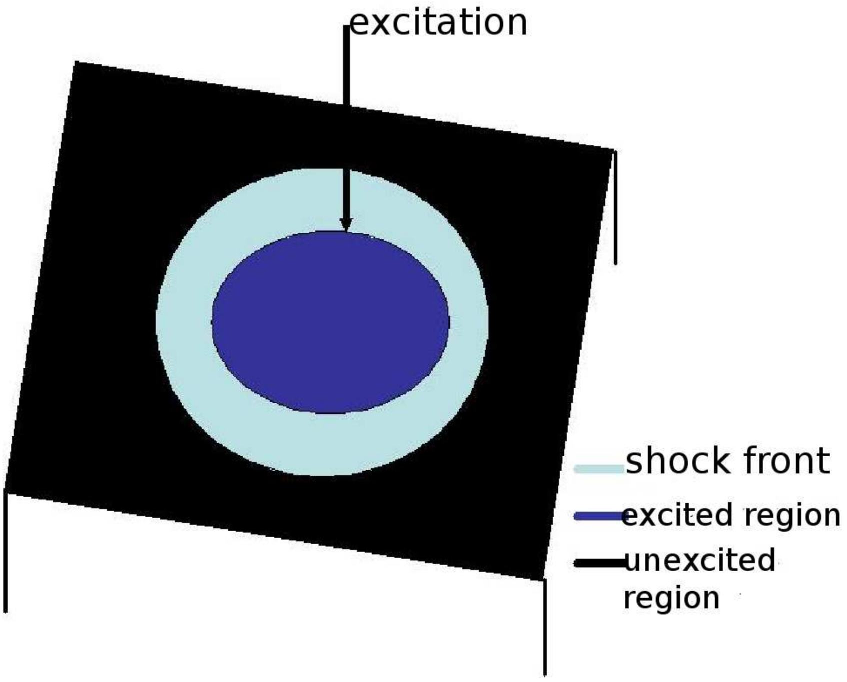

Figure 3.2: (Color online). Scheme of the mechanical change induced in α-Ce by a femtosecond laser pulse. The unexcited part of the system remains cold and is compressed with the shock velocity driven by the pressure P of the excited region, which is high due to the excitation. In the calculations, the pressure is assumed to be continuous at the interface between expanding and shocked matter.

leads to the increase of the pressure. This results in the formation of shock waves and in the expansion of the system. To describe the dynamics of the system and in particular de propagation of the shock waves after the laser heating, and for the sake of simplicity, we assume the volume expansion to be isotropic.

We assume that the total volume of the sample remains constant within the time scales on which the shock waves propagate. This assumption is clearly valid, since only a small part of the sample is irradiated (the size of the laser spot is usually considerably smaller than surface of the sample). Thus, thermal expansion of the whole sample will be a negligible effect. Moreover, it will also occur on much longer time scales than those involved in the shock-wave formation and propagation.

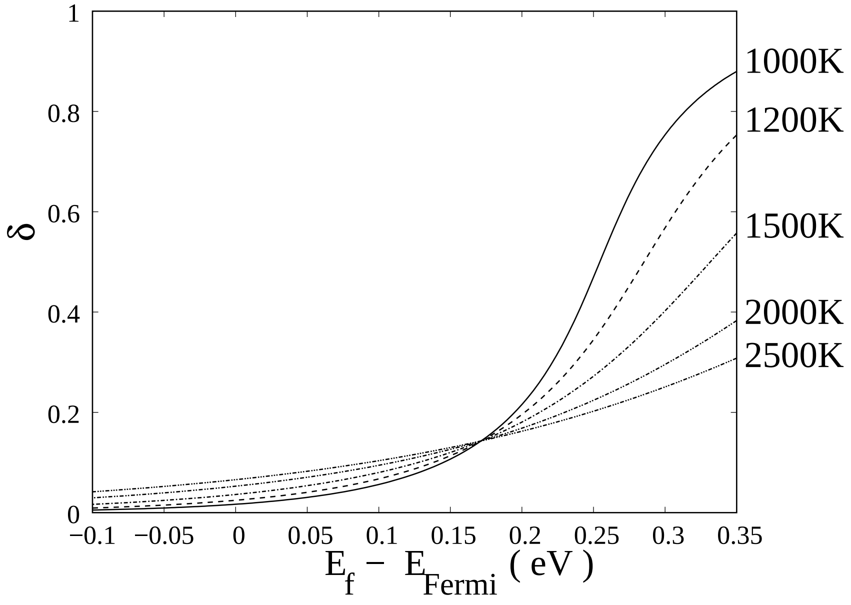

Figure 3.3: Degree of delocalization, δ, as function of f-level position in the band for different values of electronic temperature T_e. The f-level position is determined with respect to the Fermi energy The degree of delocalization δ depends strongly on the f level occupation in the band in the vicinity of the Fermi level.

Since the total volume remains constant, and as explained in the previous section, the change in volume in the heated part due to expansion is equal to the change in the unexcited part due to compression. Note that the time scale for the expansion of the excited region will be governed by the compression velocity in the unexcited part.

We have calculated the laser induced pressure from Eq. 2.9 and used Eqs. 2.10 and 2.11 to determine the particle velocity u_p. The resulting system of four equations with the four unknowns, u_s, u_p, P, V is solved numerically. In Fig. 3.4 we plot the interdependence between u_p and P.

It is important to mention that we do not consider the effect of the elastic pressure in our calculations. This is because the elastic term in the free energy (not considered in Eq. 2) will lead to volume oscillations at time scales which are much larger than those which are relevant for this work.

In Fig. 3.5 the time evolution of the volume of the excited part is shown for different electronic temperatures (corresponding to different laser fluences). We obtain very fast volume changes of the order of 15% occurring on a time scale of 150fs. This shows that ultrashort laser pulses of high enough intensity can induce ultrafast local volume changes in Ce. Interestingly, these sudden laser induced volume changes are related to a transition from α-Ce to γ-Ce. As a consequence of the expansion there is a continuous transition in the occupation of the $4f$-level from values near $n_f \sim 0$ to $n_f \to 1$.

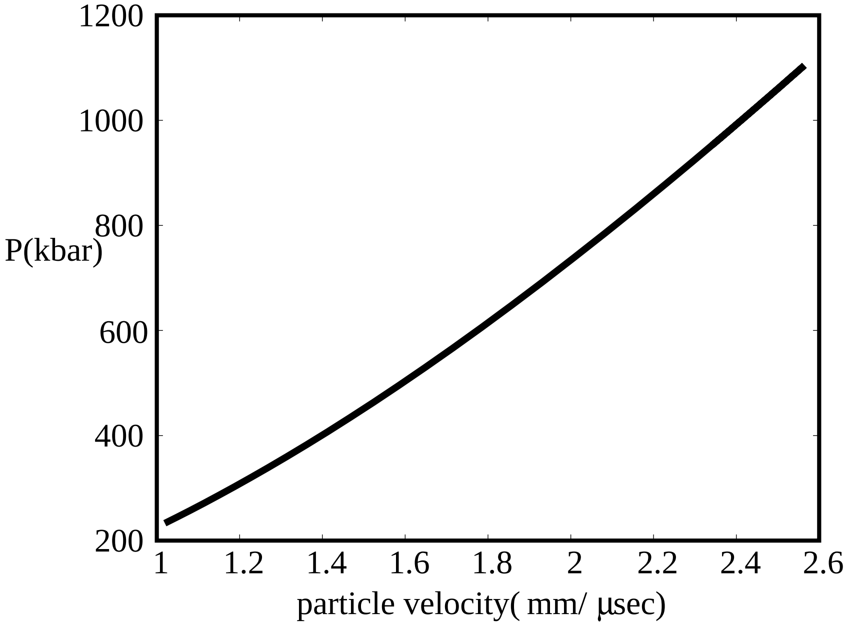

Figure 3.4: Plot of Pressure vs particle velocity in the cold material obtained in the present work. The particle velocity u_p is assumed to be constant in the bulk.

Thus, we predict a laser induced inverse volume collapse transition or a laser induced localization of the valence electrons on a sub-picosecond time scale.

In Fig. 3.6 we plot the time evolution of the degree of electron delocalization δ assuming an excitation which leads to an electronic temperature of $T_{el} = 1000$K. The very fast localization of the electrons yields to the volume changes shown in Fig. 3.5. The structural part of the transition (volume expansion) could be monitored via time-dependent rock-

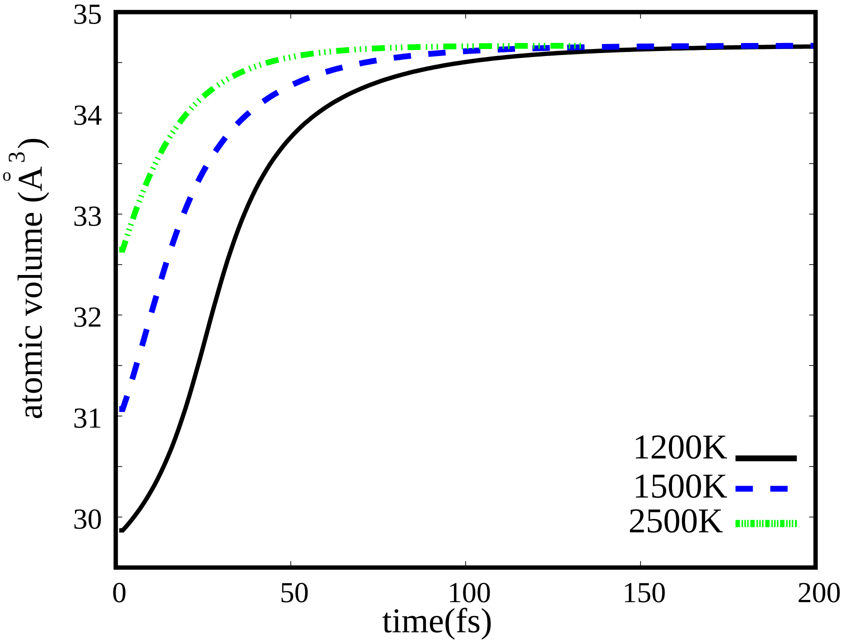

Figure 3.5: Volume variation as a function of time after laser excitation for different electronic temperatures. At the maximum reached volume the corresponding degree of delocalization is almost 0. Note that for higher electronic temperatures the volume expansion is faster.

ing curves measured through pump-probe experiments based on probe ultrashort x-ray pulses [RTD$^+$07] or through time-resolved electron diffraction [CBRZ08, HEH$^+$08]. It is well established that for fcc crystals the (111) Bragg peak is that of highest intensity. Therefore we have computed the time dependence of the Bragg reflections during the lattice expansion from the structure factor

$$| I(t) |^2 = | \frac{1}{N} \sum_{i=1}^{N} e^{iG_{khl}.R_i(t)} |^2, \tag{3.2}$$

where G_{khl} is the corresponding reciprocal lattice vector and $R_i(t)$ the position of ion i in the unit cell at time t. The diffraction angle is obtained from the Bragg condition. In the inset of Fig. 3.6 the time evolution of the (111) Bragg peak. Note that there is a very rapid shift of the peak towards smaller angles reflecting the laser induced expansion.

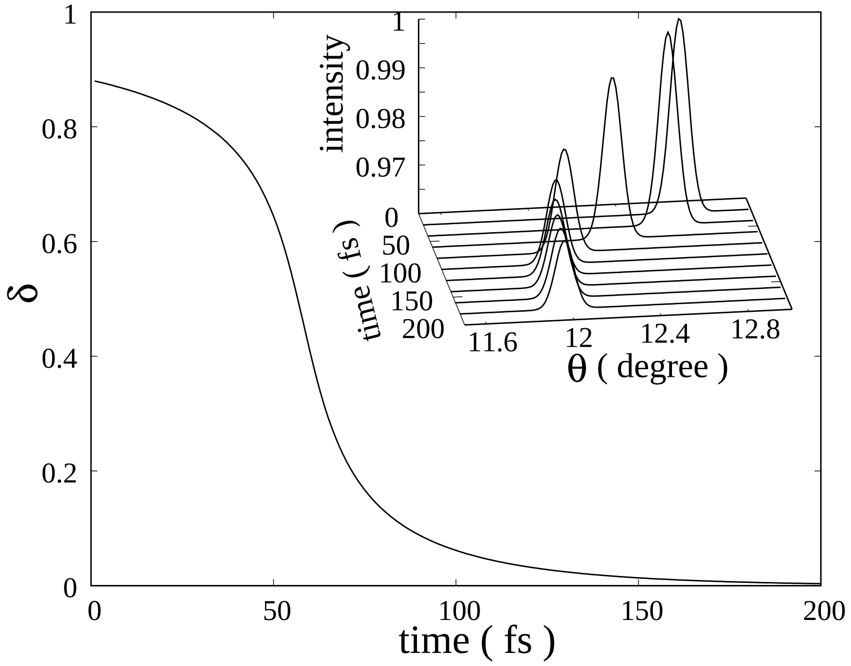

Figure 3.6: Time evolution of the electron delocalization degree for a laser excitation resulting in an electronic temperature $T_{el} = 1000K$. The initial time $t = 0$ corresponds to the laser excitation. Note that for this high electronic temperature no discontinuity is observed. The inset shows the time evolution of the [111] Bragg peak, obtained from Eq (14).

The time evolution of the pressure P after the laser excitation, derived from the free energy applying Eq. 2.9 is shown in Fig. 3.7 for different values of the electronic temperature T_{el}.

Note the presence of a maximum for a given time, which corresponds to the change in curvature for the time behavior of the volume (Fig. 3.5). This maximum shifts to shorter times as the laser fluence increases.

3.1.3 Summary

We used a microscopic model of laser induced structural changes combined with an electronic model Hamiltonian and the Hugoniot theory to demonstrate that an ultrafast photo-induced transition involving large local volume and electronic changes can be in-

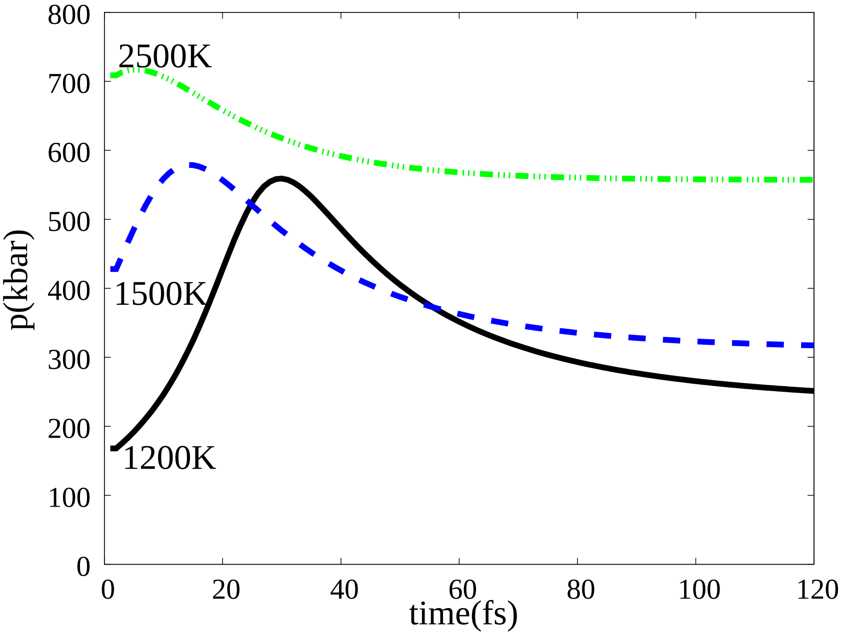

Figure 3.7: Time evolution of the total pressure for different electronic temperatures.

duced in Cerium. In the range of electronic temperatures we have considered in this work, the photoinduced transition occurs as rapid expansion of the solid, initially in the high density α phase, due to the strong excitation of the band electrons. This expansion is accompanied by electron delocalization. We predict a very fast expansion dynamics helped by the formation of shock waves. As a consequence, an ultrafast shift of the (111)-Bragg peak occurs which should be possible to measured by means of time-resolve diffraction experiments.

3.2 Structural and electronic properties of SmS

At ambient conditions SmS crystallizes in NaCl structure with 2 atoms in the unit cell. It belongs to symmetry group Fm3m (No. 225). In order to study the structural properties of SmS, we calculate the phase diagram. For this, we compute the total energy in function of crystal volume. The total energy is calculated using the DFT framework with the LDA + U SIC (Self interaction correction) formalism and the full potential linearized augmented plane wave method (FPLAPW) as implemented in Wien2k code [BSM$^+$01]. The following ingredients have been used to achieve the calculation: Orbital potential was evaluated only for $f-electrons$ in Sm atoms. Spin polarized f electrons along (001) direction and spin orbit coupling have been considered.

To better describe the ground state properties, we adopt for the exchange correlation energy, the Perdew-Burke-Ernzherof (PBE) parametrization [PBE96]. A value of 10^{-7} is chosen as charge convergence criterion, and a good convergence for the self-consistent scheme was achieved with this value. The energy separation between valence and core electrons was $\Delta E = -6Ry$. This value is large enough to allow a good separation between valence and core states in Sm. The values of Hubbard U and exchange parameter J ($U_{eff} = U - J$) were turned to describe the exact equilibrium phase diagram of SmS. We used basis set corresponding to $RMT \times K_{max} = 8.0$, where RMT is the muffin tin radius and K_{max} the plane wave cutt off. Our $RMT = 2.5$ $a.u$ was enough to confine almost all the charges inside the atomic sphere. The angular momentum for the wave function expansion inside the sphere was $l = 12$. The relativistic effects were considered by taking into account the self consistent interaction of the sixth relativistic states of Sm with total angular momentum $J = 5/2$. The smearing technique has been used to smooth the Fermi distribution. A broadening parameter of 0.002 Ry for the Fermi function was found to be low enough and gives good description of the ground state. The First Brioullin zone

Table 3.1: The calculated lattice constant (a), bulk modulus (B) and its derivative (BP) in comparison with experimental results and other LDA.

properties	present work	experiment [HS83]	other work [LSK88]
$a(a.u)$	11.29	11.29	10.4218
$B(GPa)$	47.03	50.3	84.3
BP	4.22	2.4	3.9632

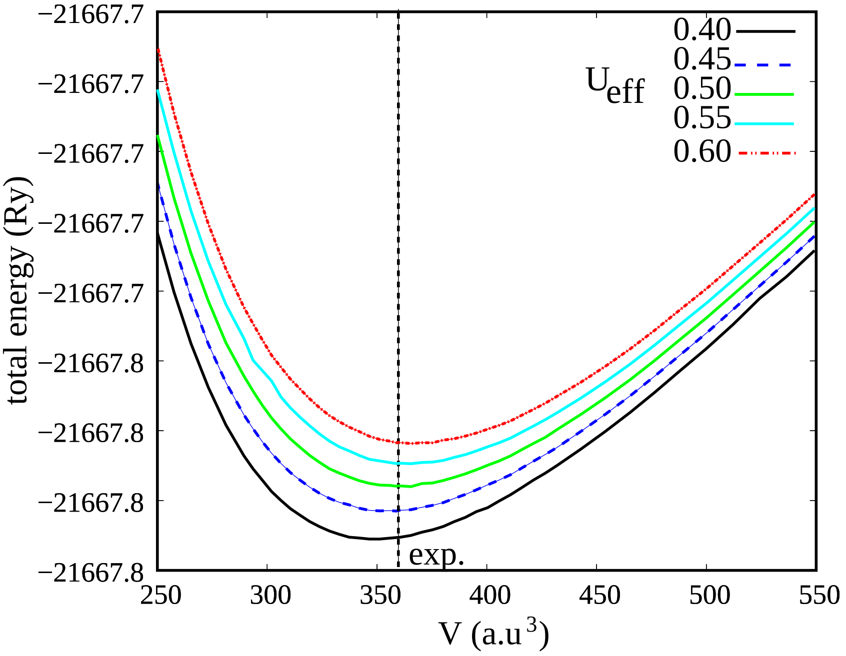

Figure 3.8: The total energy of SmS as function of volume for different values of the Hubbard parameter U_{eff}. Good description of the ground state total energy is observed at $U_{eff} \approx 0.55Ry$.

(BZ) was sampled accurately with 512 k-points and we used the tetrahedron method to perform reciprocal space integration.

The results are shown in figure 3.9. The total pressure was calculated by fitting the total energy to the Birch-Murnaghan equation of state [Bir47]. Our LDA+U calculation reproduce the correct semiconducting ground state of SmS with a Hubbard parameter value of roughly $U_{eff} = 0.5\ Ry$ ($\approx 6.8\ eV$). This value is in good agreement with x-ray photoemission spectroscopy experiment [CBWL74] which places U_{eff} in between 6 and 7 eV. Tab. 3.1 shows comparison between calculated equilibrium bulk properties and experimental results. For the lattice parameter, we obtained an exact reproduction of the experimental value ($a = 11.29$). In comparison to our LDA+U calculation, the LDA calculations provide an inadequate description of the $4f$ states in SmS due to an inappropriate treatment of correlation effects. For instance same calculation of total volume

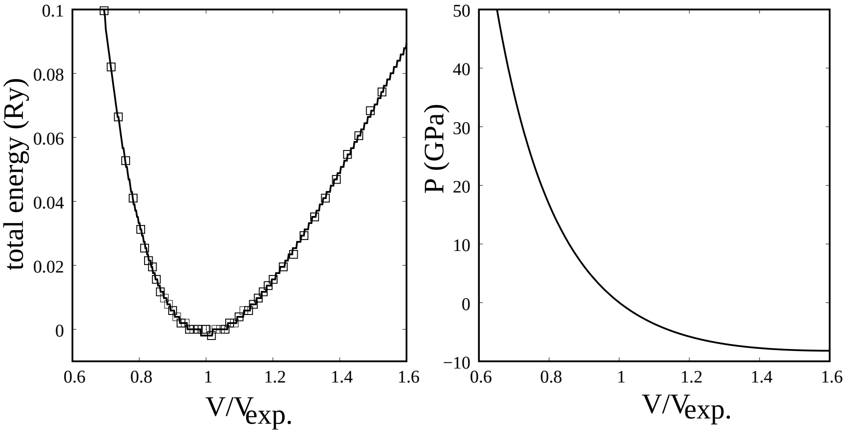

Figure 3.9: Total energy +21667.808957 and derived total pressure as function of volume. open squares are our LDA+U calculation, and data are fitted to to the Birch-Murnaghan equation. (solid lines)

versus energy using LDA approximation underestimates the equilibrium lattice constant [LSK88]. However, these calculations show that the bulk modulus agrees much better with the experimental value when the $4f$ electrons are treated as core states. Our calculated bulk modulus is slightly underestimated. In tab. 3.2 we show the calculated values

Table 3.2: Buk equilibrium properties of SmS.

$Ueff(Ry)$	latt. constant (a.u)	Bulk modulus B(GPa)	BP
0.40	11.18	48.43	4.47
0.45	11.24	47.29	4.35
0.50	11.29	47.07	4.20
0.55	11.33	46.40	4.14
0.60	11.37	46.36	4.10

of the equilibrium parameters for different values of U_{eff}.

The electronic density of states within the unit cell at the equilibrium volume is shown in fig. 3.10. A clear distinction can be seen among two groups of levels separated by the Fermi level. The first group which contains the $3p$ states of atom S and $4f_{5/2}$ of atom

Sm extends from $E = -6\ eV$ to $E = -3\ eV$ below the Fermi level; the second group is composed by $5d$ and $4f_{7/2}$ states of Sm and extends from $E = 1\ eV$ to $E = 5\ eV$ above the Fermi level. The energies of occupied and non-occupied $4f$ levels are separated by approximately U_{eff} (in good agreement with experiment [CBWL74, OA84]). The shift between the two spin states $4f_{5/2}$ and $4f_{7/2}$ is responsible of the magnetization. Thus, the f electrons determine the magnetic properties of the material. As it can be observed from fig 3.10, the six $4f_{5/2}$ are fully occupied and are localized in the gap between S $3p$ and Sm $5d$, while the $4f_{7/2}$ are completely unnoccupied and are situated well above the Fermi level. This splitting of filled and empty f bands, which is expected to be $6 - 7\ eV$ from x-ray photoemission spectroscopy [CBWL74] and bremsstrahlung isohromat spectra measurement [OA84], can not be reproduced by a simple LDA calculation. The LDA+U theory goes beyond the simple LDA theory by offering the possibility to distinguish the

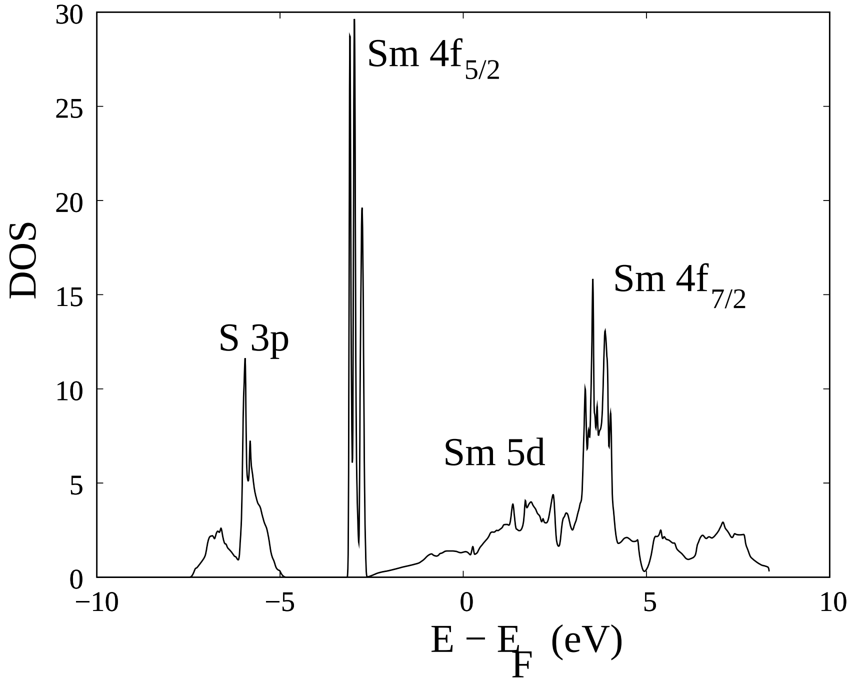

Figure 3.10: Calculated total density of states for SmS at the total energy minimum ($a = 11.29 a.u$) with f^6 configuration.

occupied and non-occupied $4f$ states. In fact the introduction of the Coulomb interaction U as an additional parameter in the one particle (LDA) equation gives better results and better understanding of the semiconducting state of SmS.

As in the case of Ce, it was also experimentally shown that applying external pressure can induce semiconductor to metal transition in SmS [JNM70, SLH+82, HS83]. This transition is accompanied by a discontinuous volume change and significant variations of the optical and electrical properties. An abrupt decrease of both the lattice constant and the resistivity were observed at 0.65 Gpa pressure at 300 K. The experimentally observed phase diagram [JNM70] shows a conversion of Sm^{2+} to Sm^{3+} ($4f \rightarrow 5d$ electron delocalization) during the transition. This is consistent with the model proposed by Falicov [RF71]. However, there is lack of understanding of some important aspects of the effects of the transition on the electronic structure. The LDA+U method emerged as a powerful method to describe the electronic structure, since it takes into account the localized nature of the f orbitals. It has been used to study the optical and electronic properties of Tm monochalcogenides (TmS, TmSe, TmTe) [AHY00] and Sm monochalcogenides(SmS, SmSe, SmTe)[AHY02].

Recent experimental study [KTM03] showed that by using femtosecond laser excitation it was possible to induce the metal-semiconductor transition in SmS. From the above results, it is clear that LDA+U approach gives very good description of the equilibrium properties of SmS and hence can be used as the basis theory to theoretically study laser induced phase transition in SmS.

3.3 Laser-induced coherent phonons in bismuth

In many materials there is extensive evidence from x-ray diffraction techniques and time-resolved optical spectroscopy [SYH83, SWS+91, STBvdL95, MMHK04] that femtosecond laser pulse can generate coherent phonons. Recently, a variety of experiments on the laser excitation of coherent phonons has been performed on bismuth [MMHK04], germanium [PKKS92, SPK93, NHM+01], silicon [KHCP05] and GaAs [IKU06]. Many excitation mechanisms such as displacive excitation mechanisms (DECP) [ZVC+91], and impulsive stimulated Raman scattering (ISRS) [YN87] have been discussed. We assume in the present work that the DECP is the only generating mechanism of the A_{1g} oscillations in Bi. The DECP mechanism is based on electronically induced displacement of the ion equilibrium coordinates. In fact the A_{1g} oscillations are consequence of the change in the minimum of the potential energy surface due to the laser excitation.

3.3.1 Time dependence of the potential energy surface

We here report the dependence of the parametrized potential energy surface on the laser parameters. In [JBM+08] a model for the time dependence of the energy density absorbed from a short laser pulse is presented. The explicit form is given by the sum of expressions (5) and (6) in [JBM+08]. This model depends on the following parameters: The electronic energy decay time τ_1, the penetration depth L_0 of the laser light, a diffusion constant D for the electrons and holes, and a constant n_0, which is the total absorbed energy from the laser. Assuming that the optical properties of bismuth do not change during the laser excitation, in the present work, we have simply obtained the time dependence of E_0 for a laser pulse of finite duration by convoluting the model of [JBM+08] with the laser pulse shape. In our simulations we have used $\tau_1 = 4$ ps, $D = 0$, $L_0 = 16$ nm, and we have varied n_0. These values are somewhat different from the experimentally determined parameters in [JBM+08], but they do not affect our qualitative conclusions. To create comparable conditions as in [MMHK04] we have assumed that the laser pulse shape is a Gaussian with a full width at half maximum of 130 fs. The resulting time-dependent potential energy surface for $n_0 = 5$ mRy/atom is shown in figure 3.11. We wish to stress

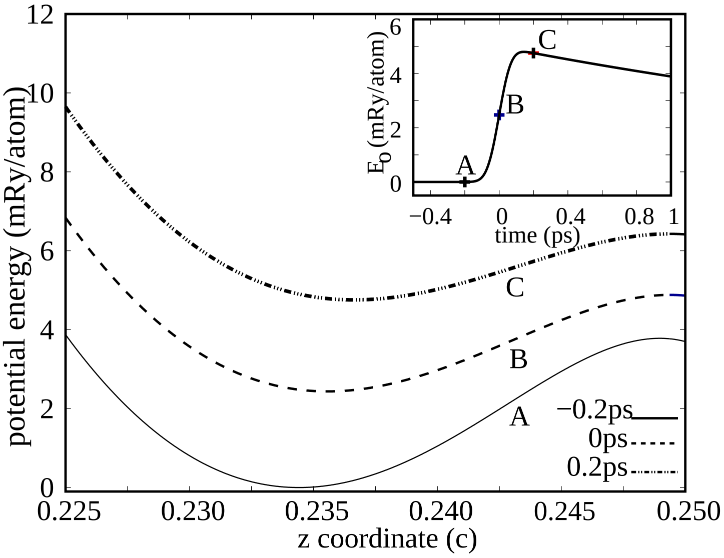

Figure 3.11: Computed potential energy at different times during ultrafast laser excitation. The curves A, B, and C correspond to the points A, B, and C in the inset. A represents the ground state potential, B is the excited potential at the peak time of the gaussian pulse, and C represents the potential at $t = 200$ fs. The inset shows the variation of the absorbed energy E_0 as a function of time.

that our approach, which combines the model of [JBM$^+$08] and the parametrization of section 2.3.4, can be used to describe the time-dependent potential energy surface of bismuth due to lasers pulses of arbitrary shapes and intensities.

3.3.2 Collapse and Revival phenomenon

Our computed oscillatory parts of the expectation value of the z coordinate of Bi are shown in figures 3.12 and 3.13. As pointed out in the previous sections, the oscillations depend on the laser characteristics (fluence, pulse duration, pulse shape). In figure 3.12 we show the dynamics of the phonon wave packet in a two-atom system ($N = 1$). The interaction of the wave packet and the potential leads to a series of collapses and revivals. At low fluences, collapses and revivals are not observed in agreement with experiment [MMHK04]. For high fluences, we found that the collapse and revival times increase when

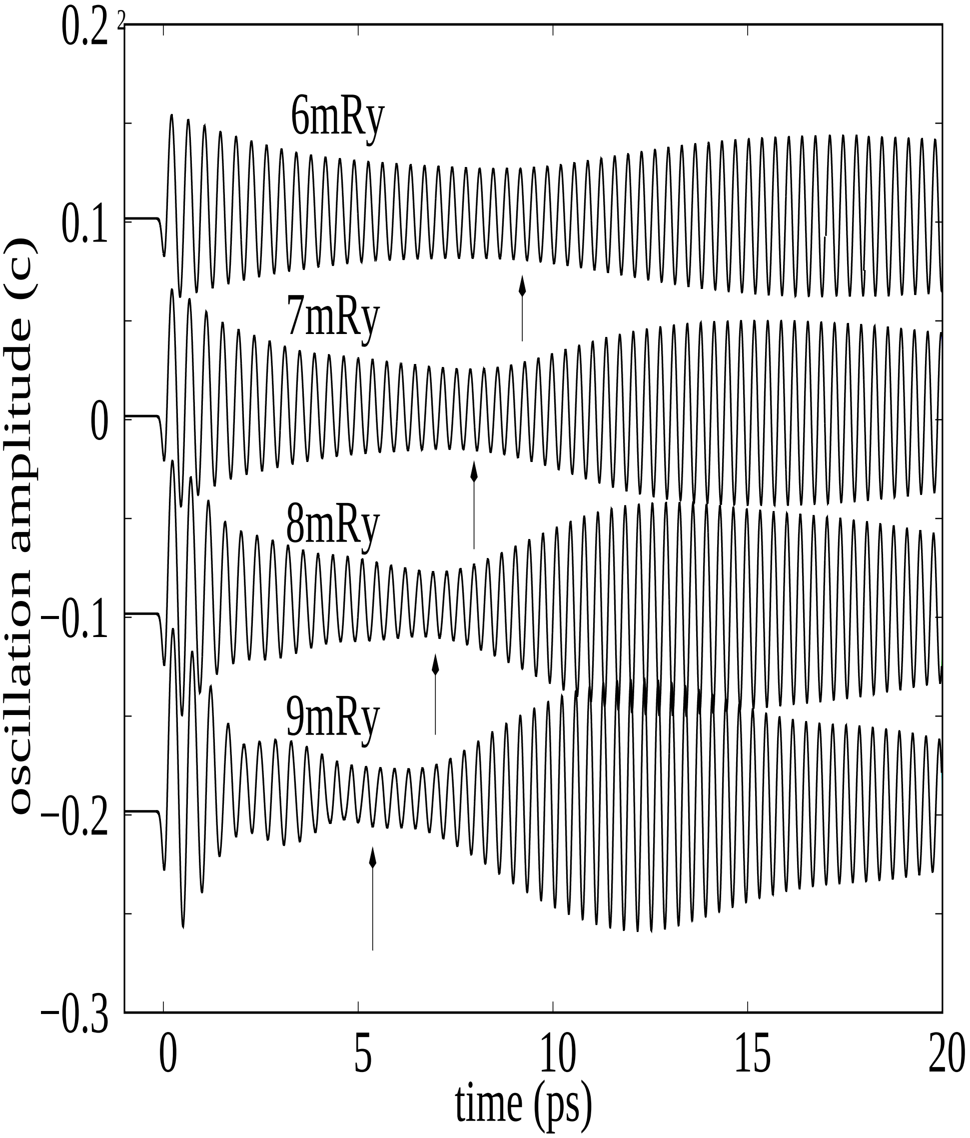

Figure 3.12: Oscillatory part of the z coordinate of an artificial dimer ($N = 1$) for different absorbed energies n_0. The excitation was caused by a laser with pulse duration of 130 fs. Note that the curves are offset along the y axis, for clarity of presentation. Arrows indicate the amplitude collapse of the oscillations.

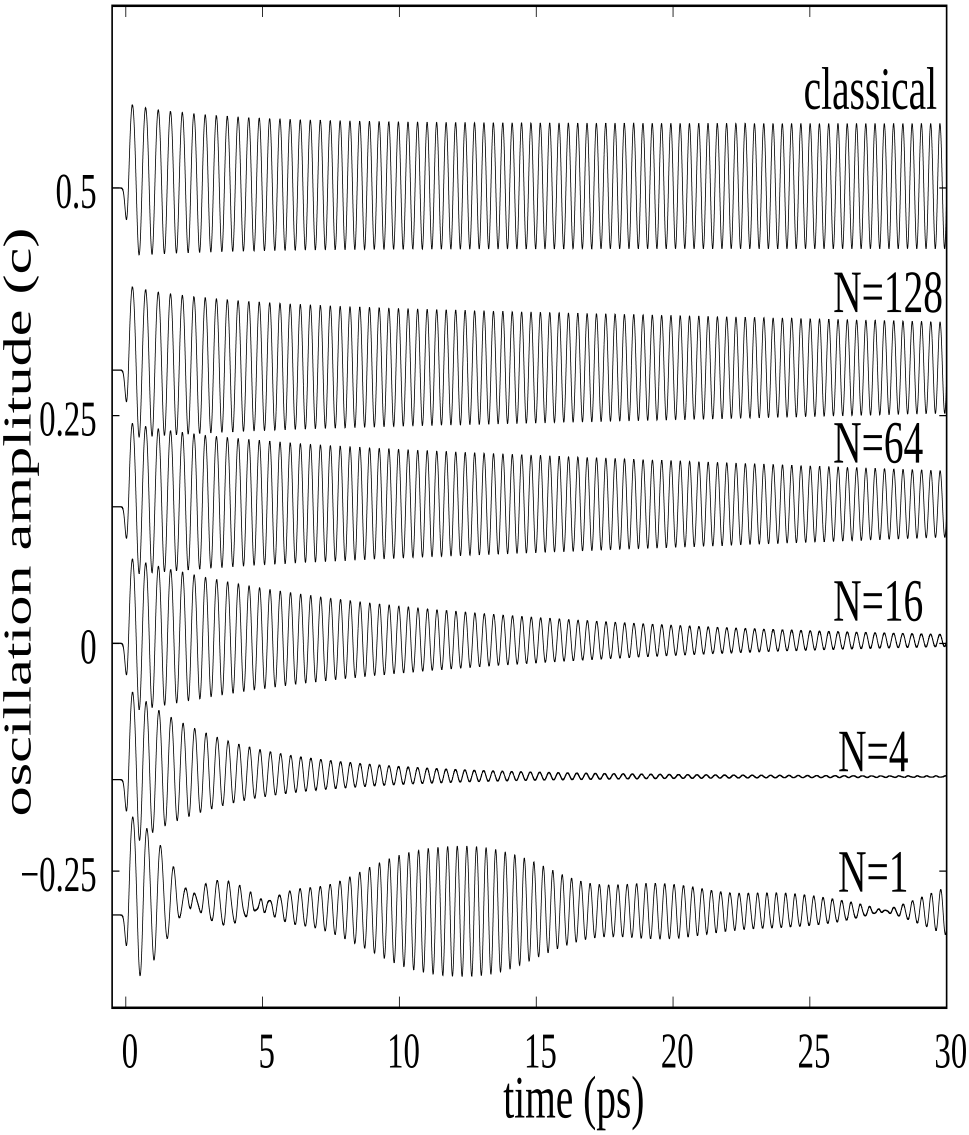

Figure 3.13: Oscillatory part of the z coordinate for an absorbed laser energy of $n_0 = 10$ mRy/atom and a pulse duration of 130 fs. Curves for different values of N are offset along the y axis. The five lowest curves show results from our quantum dynamical simulations and the uppermost curve shows the classical trajectory of the resulting $A_{1\mathrm{g}}$ oscillation.

the absorbed laser energy is decreased. Figure 3.13 shows the results of our quantum dynamical simulation as a function of system size. As was to be expected (sec. 2.3.5), for large systems the behavior of the quantum system approaches the classical limit (the top curve in figure 3.13). This implicates that the experimentally observed series of beatings in bulk bismuth [MMHK04] cannot be explained as a quantum mechanical effect, but is most likely of classical origin.

3.3.3 Discussion

We have performed quantum dynamical simulations on time-dependent potential energy surfaces in order to elucidate the origin of experimentally observed [MMHK04] beatings of laser-induced coherent phonons in bismuth. By introducing a parameter for the number of unit cells included in our study we found that the behavior of the excited phonons approaches the classical behavior rapidly as a function of system size. This is a strong indication that quantum effects do not play a role in the generation of the observed beatings. Possible alternative explanations are a classical interference between signals reflected from different parts of the sample or the beating between excited modes of different symmetries. The first mechanism would presuppose that the sample has been heated unevenly by the laser. Of course from our computations we cannot judge the likeliness of this scenario, but we hope that our study will inspire experimentalists to study this possibility. The second mechanism requires that at least two kinds of phonons are excited in bismuth, that their frequencies are near, and that there is a strong coupling between the two modes. Whereas the first condition is fulfilled (so-called E_g phonons are excited in Bi through Ramann scattering), previous calculations on bismuth [ZTG06a, ZTG06b] indicate that the $A_{1\mathrm{g}}$ and E_g frequencies are not close enough to explain the observed beatings and that the coupling between these modes is relatively weak. Therefore, we believe that this latter explanation is unlikely.

3.4 Lattice dynamics of germanium.

3.4.1 Structural properties

In this subsection we report the structural properties of bulk germanium as function of lattice temperature. We used the NOTB MD simulation described in sec. 2.4.5 to investigate the thermal equilibrium properties of germanium at constant pressure.

Germanium crystallizes in diamond structure at room temperature. Diamond structure can be seen as two inter-penetrating face centered cubic (fcc) structures with atom (0,0,0) the position of the first fcc structure and atom $(1/4, 1/4, 1/4)$ the origin for the second one expressed in terms of the basis vector. Each atom is surrounded by four nearest neighbors in a tetrahedral bonding configuration (coordination number is four) and the nearest neighbor distance is equal to $\sqrt{3}a/4$, with a the lattice constant.

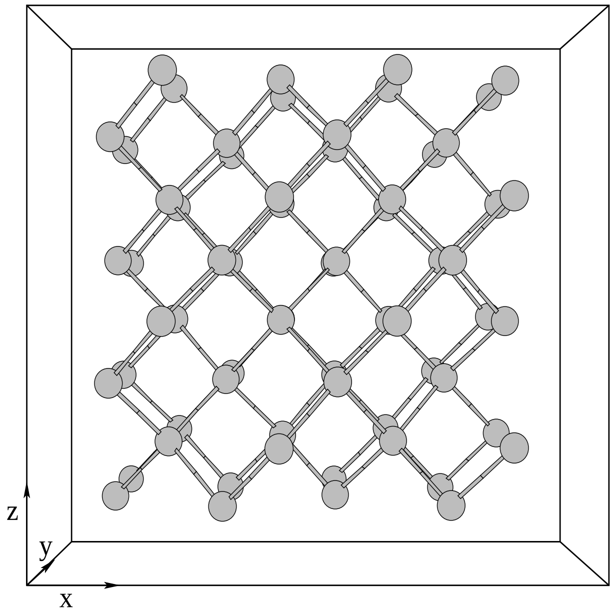

Figure 3.14: The 64 supercell diamond used for the NOTB calculation. The snapshot was taken during the molecular dynamics run at T=300K and $t = 10$ *ps*. It shows the tetrahedrally bounded nature of the structure of Ge at ambient temperatures.

Constant pressure molecular dynamics simulation were performed at different temperatures using the Parrinello-Rahman approach [PR81]. The system was initially arranged in a 216 (8 x 3 x 3 x 3) perfect diamond crystal (unit cell of diamond contains 8 atoms). For each temperature, an equilibration run of 50 ps was performed. The time step used to solve the Newton equations was 1 fs. These ingredients were sufficient to yield static properties and adequate bond fluctuations were found at any finite temperature ranging from $0K$ to $4000K$.

For the description of the 0 K configuration we computed the cohesive energy which is the energy required to break all the binding atoms into isolated atoms. The knowledge of the volume dependence of the cohesive energy is important for determining the equilibrium structure. Fig. 3.15 displays the cohesive energy per atom as function of the relative volume. The experimental equilibrium lattice constant ($a_0 = 5.65\mathring{A}$ i.e. neighbor distance $r_0 = \frac{\sqrt{3}}{4} a_0 = 2.45\mathring{A}$) is well reproduced.

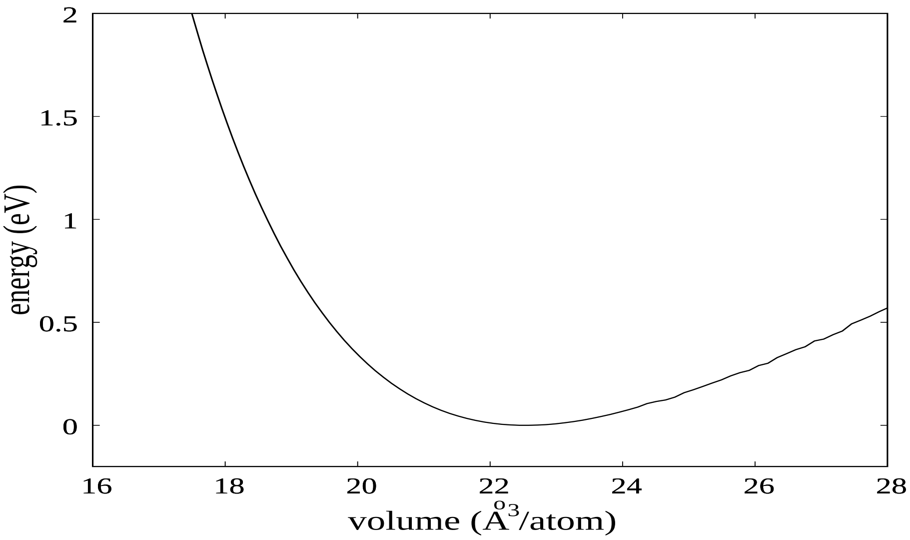

Figure 3.15: Equation of states for diamond structure of Ge. Curve obtained from a fully relaxed zero temperature with the nonorthogonal tight binding scheme discussed in section 2.4.1.

In order to study the thermodynamic properties one needs to introduce temperature into the system. This is not an obvious task because of the fluctuation of the temperature in micro-canonical ensemble. To maintain the system at a given temperature, we rescale the velocities of atoms at regular time intervals (every 100 × timesteps). Physically, rescaling the velocities at regular time intervals consist to add and remove energy from the system. There is no physical justification of such method but it is an efficient tool to avoid large variation of the temperature. According to the equipartition theorem, at the thermal equilibrium state the kinetic energy per degree of freedom is $3/2k_BT$.

For the analysis of the structure at a given temperature, we computed the pair correlation function $g\left(r\right)$, the bond angles distribution $g\left(\theta\right)$ and the coordination number n. The pair correlation function $g\left(r\right)$ is the density of atoms surrounding a given particle in the MD cell. It reads

$$g\left(r\right) = \frac{V}{N^2}\langle\sum_{i=1}^{N}\sum_{j\neq i}^{N}\delta\left[r-\left(R_i-R_j\right)\right]\rangle. \tag{3.3}$$

Where V is the cell volume and N the number of atoms. This pair correlation function is important for many reasons, it gives many informations about the structural nature of the system at any temperature. The structure factor which is the Fourier transform of this pair correlation function can be measured experimentally from neutron and X-ray diffraction techniques. Fig. 3.16 shows the pair correlation function computed at different lattice temperatures. The highest peaks observed in the different curves indicate the average distances of the nearest neighbors. Simulation performed at $T = 300K$ with a fully relaxed system, shows an average neighbor distance $r_n = 2.45\mathring{A}$, which corresponds to the experimental bond length of solid Ge. The other peaks with decreasing amplitudes indicate the long-range order of the crystal and give the location of neighbors at longer distances. However, the pair correlation function is in itself not sufficient to determine the real nature of the crystal, since it gives only informations on the inter-atomic distances and the number of neighbors of each atom. Therefore, to better describe the different phases of germanium at finite temperatures we computed the bond angles distribution

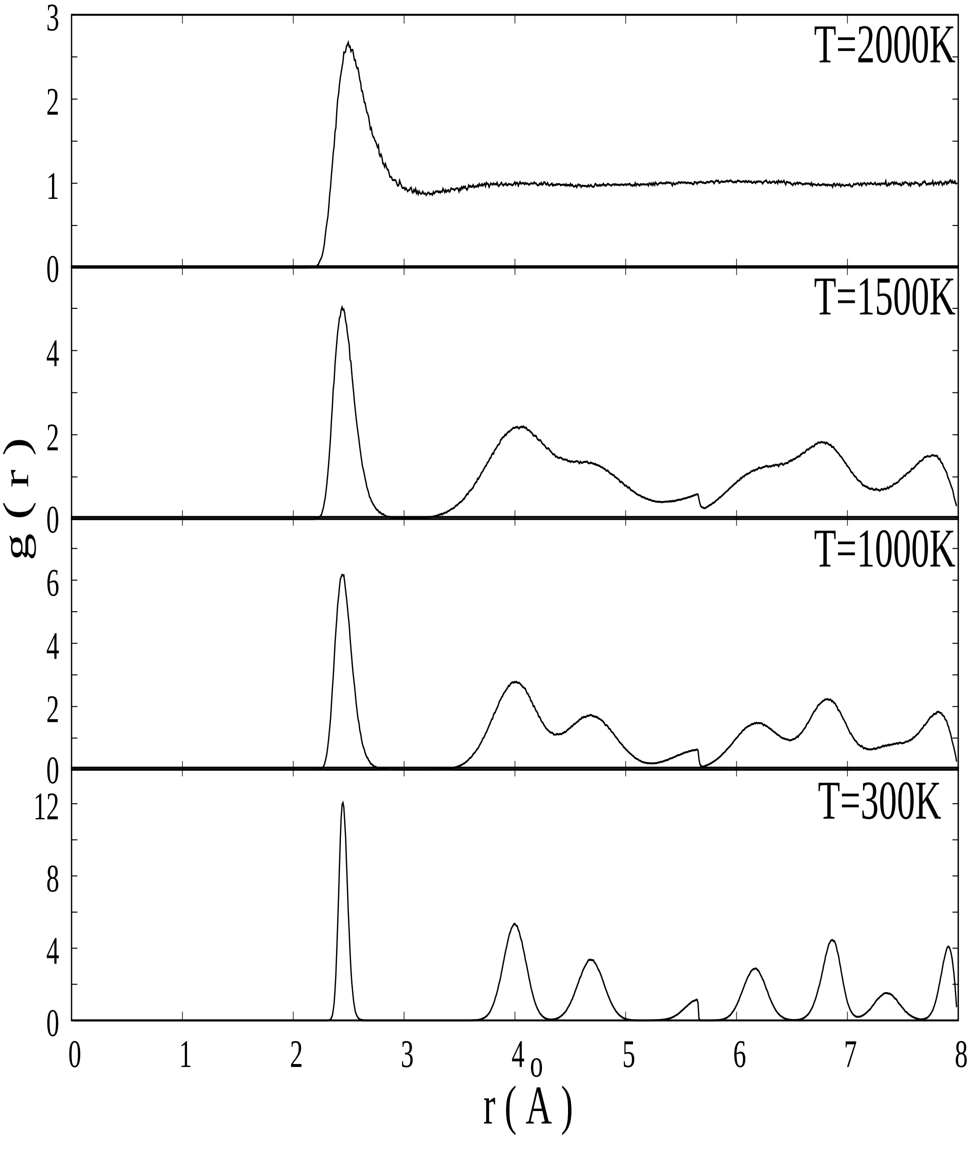

Figure 3.16: Calculated radial distribution functions. Each curve corresponds to a radial distribution function calculated from an ensemble average of $N = 1000$ configurations in the molecular dynamics trajectory at temperature T. One can clearly observed the ordered nature of the crystal at low temperatures with well defined peaks of the pair distribution function. The solid-to-liquid transition (melting) is observed at $T \approx 1500K$.

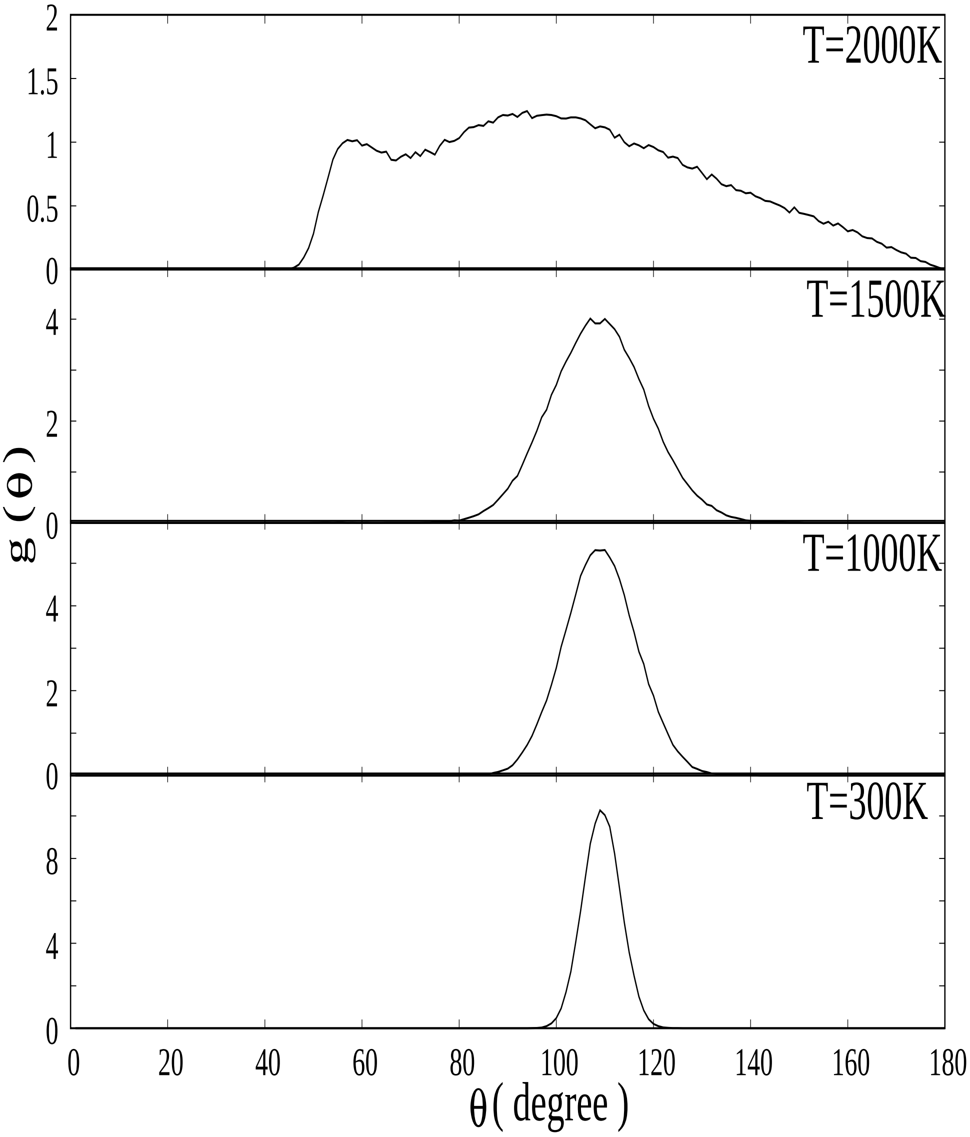

Figure 3.17: Plot showing the calculated bond angles distribution functions. Each curve corresponds to a bond angles distribution function calculated from an ensemble average of $N = 1000$ configurations in the molecular dynamics trajectory at temperature T.

function corresponding to the same MD trajectories.

The bond angle is defined as the angle between two vectors joining a given atom in the MD cell. For its determination, a cut off distance r_{cut} was chosen. The value of r_{cut} is in between the first two peaks of the pair correlation function. Fig. 3.17 shows the calculated bond angles distribution at different lattice temperatures. The sharp peaks observed at $\theta = 109$ degree give evidence of the tetrahedral nature of the crystal at low temperatures. The results showed in Figs. 3.16 and 3.17 indicate strongly that the stable bonding configuration of germanium at low temperatures is the diamond structure. From Figs. 3.16 and 3.17 one can also clearly see that the crystal melts at roughly $T = 1500K$. This calculated melting temperature although different to the experimental value ($T^{exp}_{melting} = 1211K$), is an acceptable value compared to other simulation result [Bor00]. We do also emphasize that the temperature of the system is statistically defined and it is not an obvious task to extract its exact value since it fluctuates. This is due to the fact that we have considered a micro-canonical ensemble where the potential energy as well as the kinetic energy fluctuate while the total energy remains constant.

The melting properties can be also carried out via the determination of the coordination number. Fig. 3.18 displays the calculated coordination number as function of lattice temperatures. The coordination number is calculated by integrating the radial distribution function from $r = 0$ to $r = r_{cut} = 3.2$ Å, so that only the first neighbors are included. The constant value at temperatures below $T = 1500K$ confirms that the crystal remains in diamond structure at low temperatures ($n = 4$ for bulk diamond), and the discontinuity observed at $T = 1500K$ indicates the disordered nature (liquid phase) of the structure at temperature more than $1500K$.

The combination of the three figures 3.16, 3.17 and 3.18 gives a direct analysis of the atomic structure at each temperature. Note that for all the above mentioned results the pressure was kept constant at low values and the variation of the MD cell size was

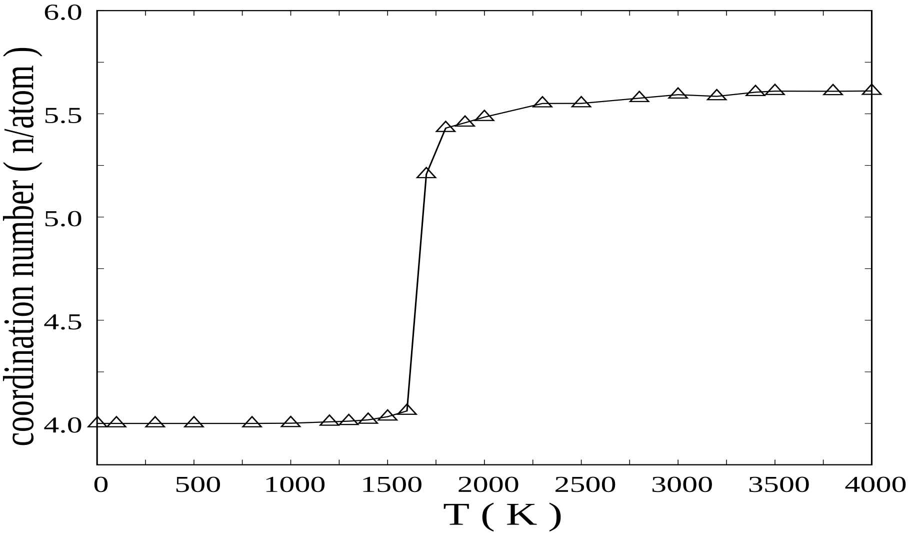

Figure 3.18: The coordination number as function of lattice temperatures. At low temperatures its value is 4 as expected. The dramatic change at about $T > 1500K$ indicates the disordered nature of the crystal.

obtained using the standard Parrinello-Rahman approach [PR81] as described in [JG]. In summary, the calculated structural properties of germanium (pair correlation function, bond angles distribution, coordination number) are in satisfactory agreement with experimental results. Further investigations have been done to determine the vibrational properties of germanium.

3.4.2 Vibrational properties

Lattice vibrational properties of germanium are presented here. We computed the phonon dispersion curves using the frozen phonon method as implemented in the `FROPHO` code [Tog] in the framework of the nonorthogonal tight binding (NOTB) Hamiltonian described in sec. 2.4.2. The frozen phonon method [KM, KM82] is a direct approach in which a distorted crystal is treated as a crystal in new structure. The distortion of the initial equilibrium structure implies significant increase of the inter-atomic forces [KM82]. Thus, the dynamical matrix of the entire system can be built and the phonon frequencies are obtained from the diagonalization of this matrix (see appendix for more details). The equilibrium phonon frequencies of Ge (electronic ground state $T_{\mathrm{el}} = 0$) are

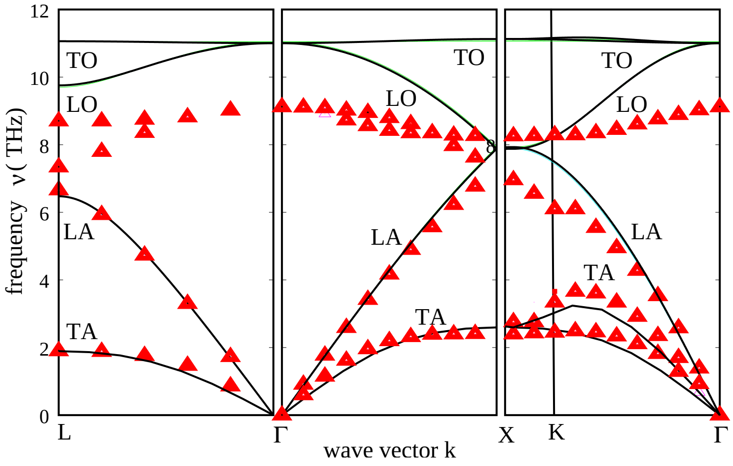

Figure 3.19: The calculated phonon dispersion curves along high symmetry directions in the Briouillin zone (lines) in comparison with experimental results (triangles) [NN70].

reported in Fig. 3.19. The transverse acoustic (TA) as well as the longitudinal acoustic (LA) phonon frequencies agree well with the experimental results [NN70]. Fig. 3.20 shows the phonon dispersion curves and the corresponding density of states. Very strong localization is observed for modes at the high- and low-frequency edges of the phonon spectrum.

We do emphasize that our calculated optical phonons can not be exactly compared to the experimental data [NN70] because of the limitation of the frozen phonon method to describe such phonons [Tog].

From the above results it emerges that our nonorthogonal TB method yields a correct description of bulk germanium. This makes us confident to investigate the dynamics under laser excitation.

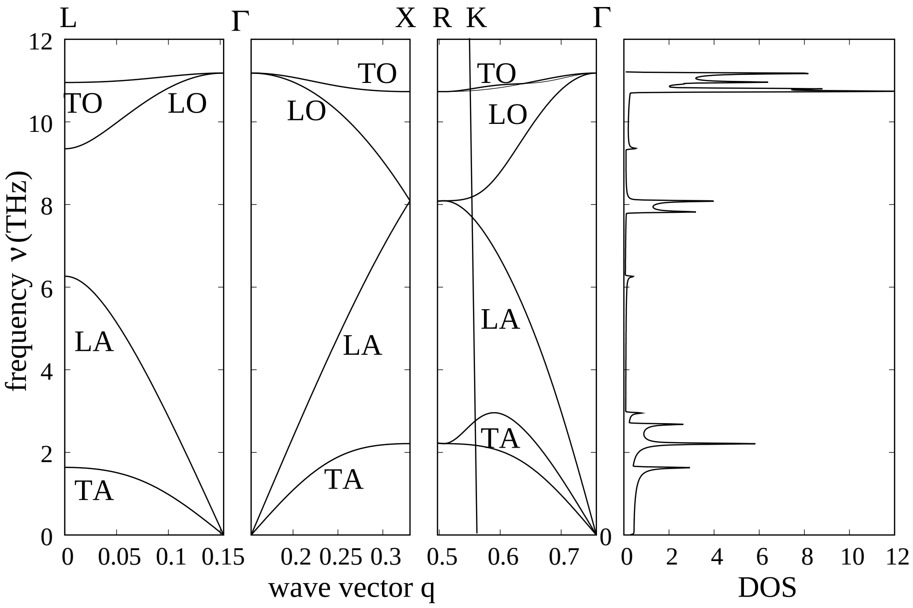

Figure 3.20: The phonon dispersion curves along high symmetry directions in the Briouillin zone and density of states of Ge calculated with our sp^3 NOTB.

3.4.3 Laser induced coherent phonons

It has been experimentally observed that femtosecond laser pulse can generate coherent phonons in germanium [PKKS92, SPK93, NHM+01]. In general coherent phonons in solids can be excited by a laser pulse whose pulse duration is shorter than a phonon period (typical transverse acoustic phonon in germanium $\approx\ 500 fs$ at the ground state). The focus of the present work is to analyze the coherent vibrations in the acoustic directions of bulk germanium when excited by a femtosecond laser pulse. We assume that the displacive excitation mechanism (DECP) [ZVC+91] is the generating mechanism of the oscillations. We show that irradiation with moderate fluences ($< 2\ eV/atom$) induces oscillations of atoms along the acoustic directions. Germanium is indeed characterized by a small and indirect band gap ($E_g = 0.66\ eV$). Therefore a minimum of absorbed energy of E_g is required to excite electrons from the valence band to the conduction band.

In this study, the electron-hole pairs are generated with excitations pulse of 50 fs

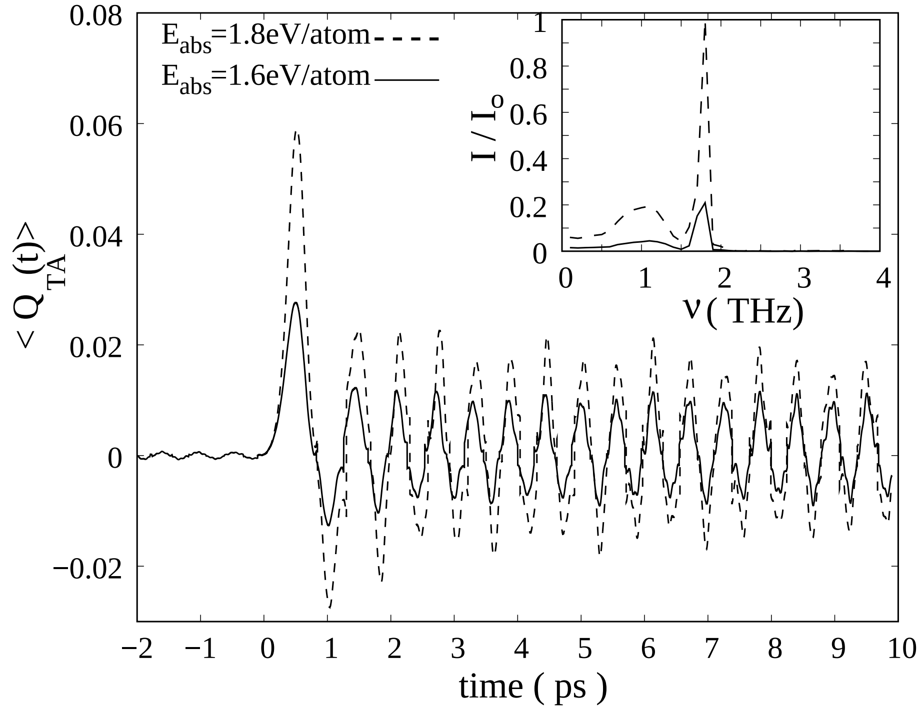

Figure 3.21: Motion along the transverse acoustic direction at low fluences, with pulse duration of $50fs$. The inset represents the Fourier transform of the oscillatory part.

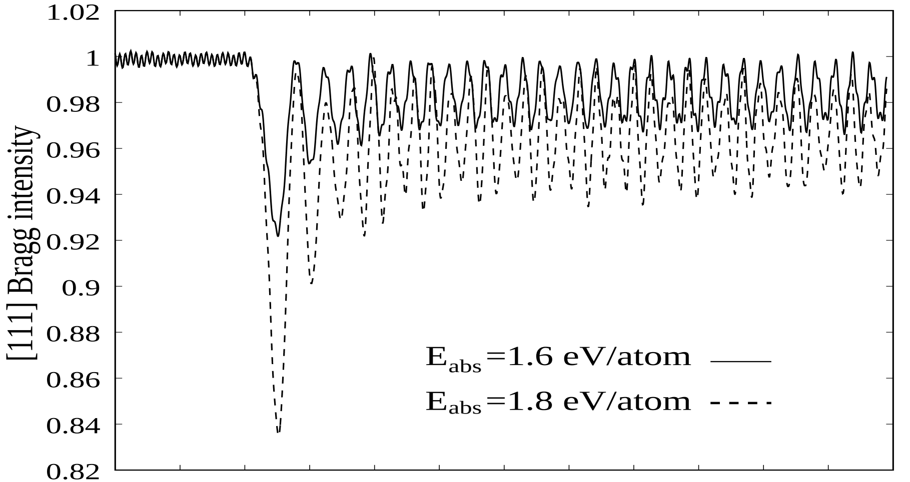

Figure 3.22: Time evolution of the [111] Bragg peak intensity of Ge at low fluences, with pulse duration of $50fs$.

duration and absorbed energies per atom of 1.6 eV and 1.8 eV. These laser characteristics are sufficient to drive coherent phonon oscillations in Ge [SPK93]. However, as previously mentioned the only requirement for the pulse durations is that they do not exceed the phonon period [MMHK04, IKU06], and for the fluences is that they must be below the melting threshold value ($\approx$ 2.0 eV). As shown in many experiments the high symmetry L point in the diamond structure is a natural reference point for analyzing the structural changes.

In Fig. 3.21 we report the time dependence of the transverse acoustic (TA) phonon coordinate at high symmetry L point in the first Briouillin zone. A coherent oscillation with a frequency of $\nu \approx 1.86$ THz is clearly observed, matching exactly the acoustic-phonon frequency in germanium corresponding to this low excitation. The inset of Fig. 3.21 shows the Fourier transform of the oscillatory part of the TA phonon coordinate trajectory.

In Fig 3.22 the response of the [111] Bragg peak intensity to the laser excitation is shown. A slight drop of the intensity (less than 20% of its initial value) followed by coherent oscillations is observed. Same behavior has been also observed for pulses duration less than 200 fs and absorbed energies ranging from 1.0 eV to 2.0 eV. Beyond 2.0 eV we assist to a complete destruction of the crystal order which can lead to melting.

3.4.4 Ultrafast non-thermal melting

In this subsection we report the analysis of laser induced non-thermal melting of bulk germanium. As described in sec. 2.1, the generation of hot electron-hole plasma by an intense laser excitation may also yield a strong destabilization of the lattice structure.

As consequence of the lattice destabilization a transition from the covalent crystalline state to a liquid state occurs. Such transition which takes place within few hundred femtoseconds after the excitation (In comparison normal thermal transition occurs in

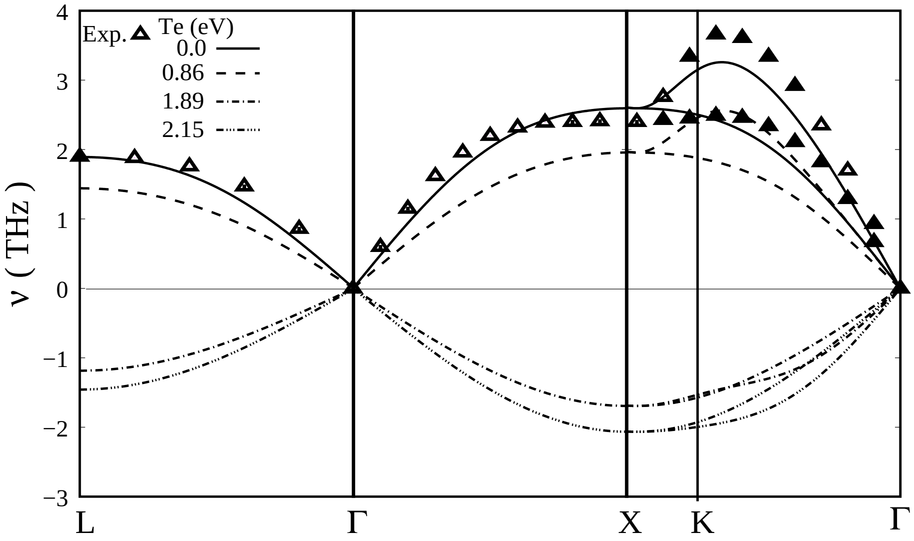

Figure 3.23: Transverse acoustic (TA) phonons at the different high symmetry points in the first Brillouin zone at different values of electronic temperature (T_{el}). Pure imaginary frequencies are plotted as negative.The points in the main figure are experimental values taken from [NN70].

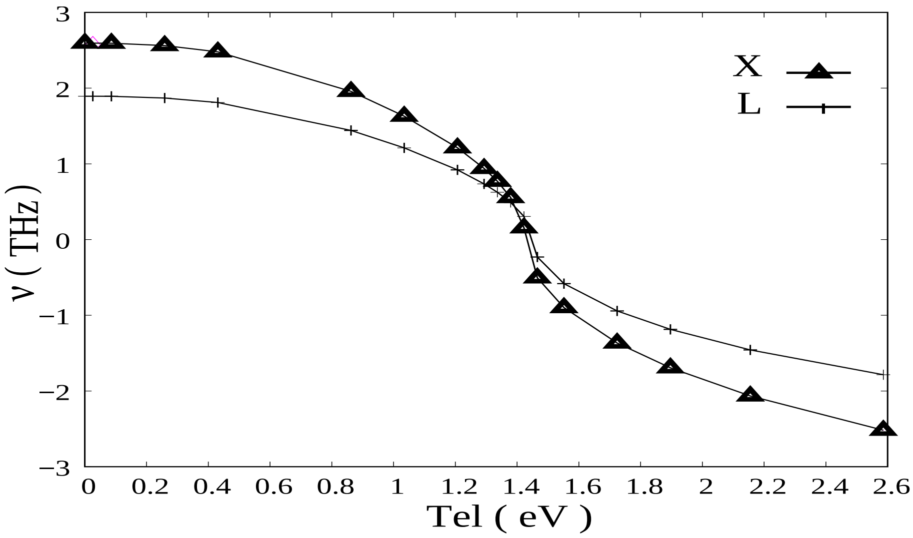

Figure 3.24: Transverse acoustic (TA) phonons frequencies at the high symmetry points X and L in the first Brillouin zone vs electronic temperature (T_{el}). Pure imaginary frequencies are plotted as negative.

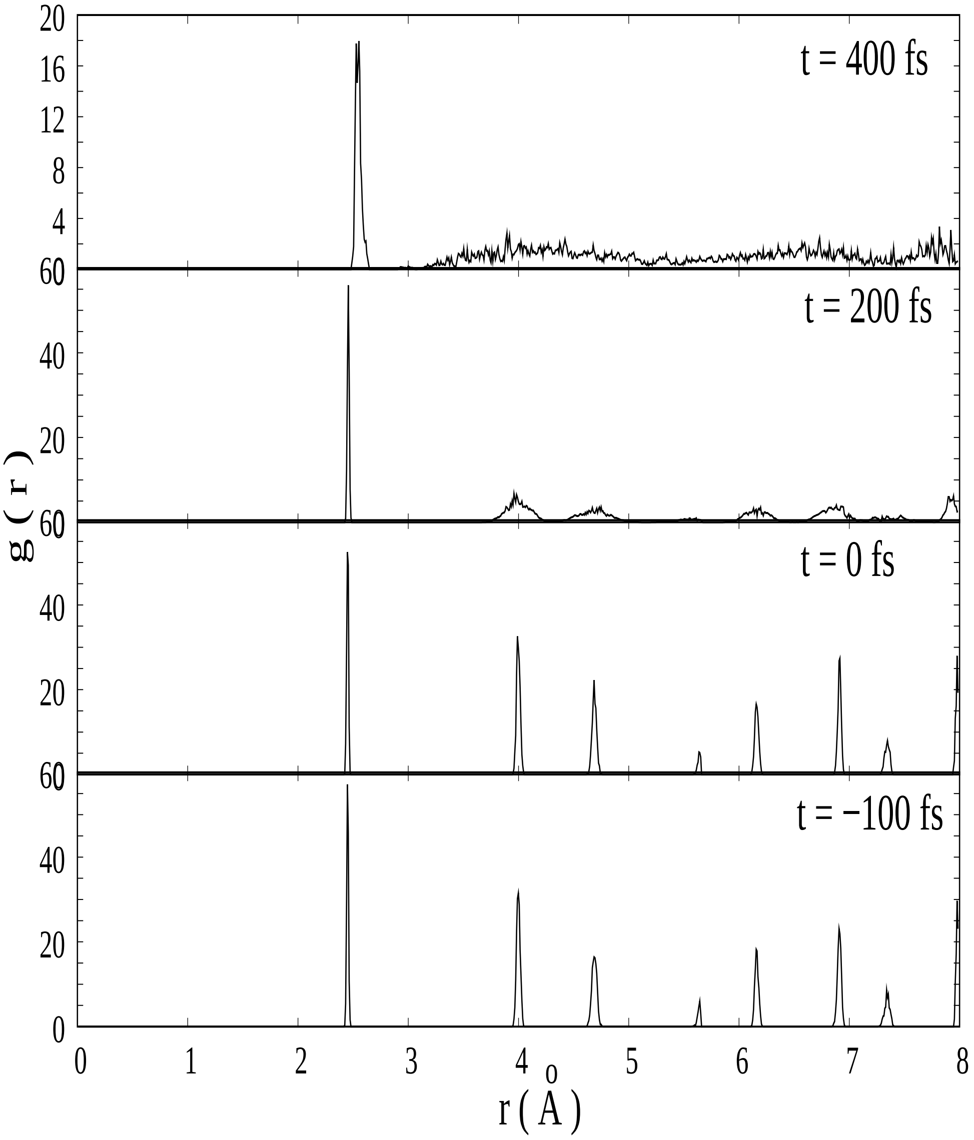

Figure 3.25: Computed time evolution of the radial distribution function after excitation with a laser pulse of $\tau = 50$ fs duration. The intensity of the pulse was chosen to reach an absorbed energy of 2.6 eV/atom. The peak time of the gaussian pulse corresponds to $t = 0\ ps$.

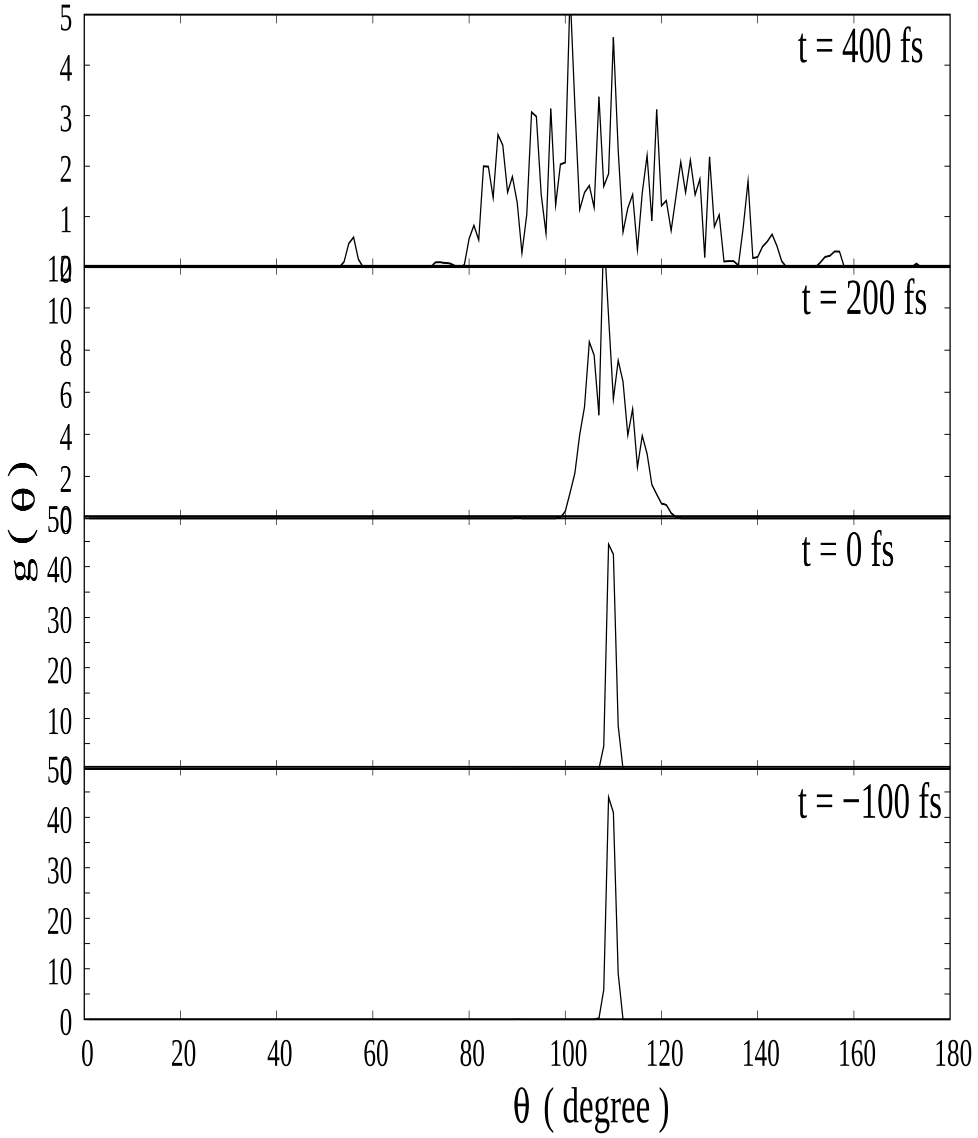

Figure 3.26: Computed time evolution of the bond angles distribution (see text) after excitation with a laser pulse of $\tau = 50$ fs duration. The intensity of the pulse was chosen to reach an absorbed energy of 2.6 eV/atom. The peak time of the gaussian pulse corresponds to $t = 0\ ps$.

much longer time scale) has been extensively investigated by means of ultrafast x-ray diffractions [CTS+01, STBB+03, STBD+03, RTD+07] and ultrafast optical spectroscopy [BBSS06, CBRZ08, HEH+08]. This electronically induced solid-liquid transition is referred to as "ultrafast non-thermal melting" because the time scale required is much shorter than that required for the thermalization of ions due to the deposited laser energy.

We performed two types of calculation in order to analyze the problem of ultrafast melting: We first determined the phonon spectrum of bulk Ge (Fig. 3.20) at the electronic

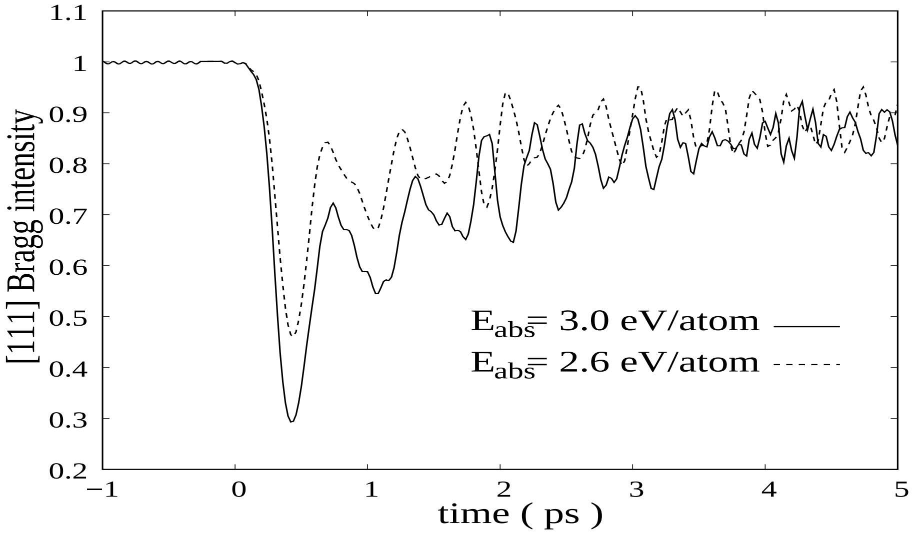

Figure 3.27: Time evolution of the [111] Bragg peak intensity of Ge after excitation with a laser pulse of $= 50fs$ duration, The energy absorbed from the laser was $2.6eV/atom$. The peak time of the gaussian pulse corresponds to $t = 0\ ps$.

ground state. We performed the same type of calculation, but assuming the electrons to be at a high temperature T_{el} in order to simulate the laser excitation. We were especially interested in seeing how the TA modes are affected by the laser excitation. The results are presented in Fig. 3.23 as well. One can clearly observe how the TA phonons undergo a dramatic softening as the electronic temperature (i.e., the laser intensity) increases. In fact the anharmonicity of the TA modes becomes more significant as the electronic temperature increases, and it help to advance the structural transformations. Moreover, for high enough values of T_{el} the TA frequencies become purely imaginary in the range between the high symmetry points L, Γ, X and K of the Brillouin zone. This means that the potential surface along these directions and for all the k-points in between becomes repulsive. A particular case is shown in Fig. 3.24, in which the softening and the transition to a pure imaginary frequency is shown for the TA modes at the X and L points. This is in agreement with the predictions of Stampfli and Bennemann for Silicon [SB94]. Although the laser induced softening of particular phonon branches gives us important information about the first stages of the melting of Ge, it is necessary to perform MD simulations in order to learn more about the time scale of the melting process. Therefore we performed MD simulations using a supercell consisting of 64 atoms. To follow the dynamics of melting of Ge we calculated the time evolution of the structural properties such as the bond angles distribution , the pair correlation function and also the [111] Bragg peak intensity. For the determination of the bond angles a cut-off distance of 3.2 Å

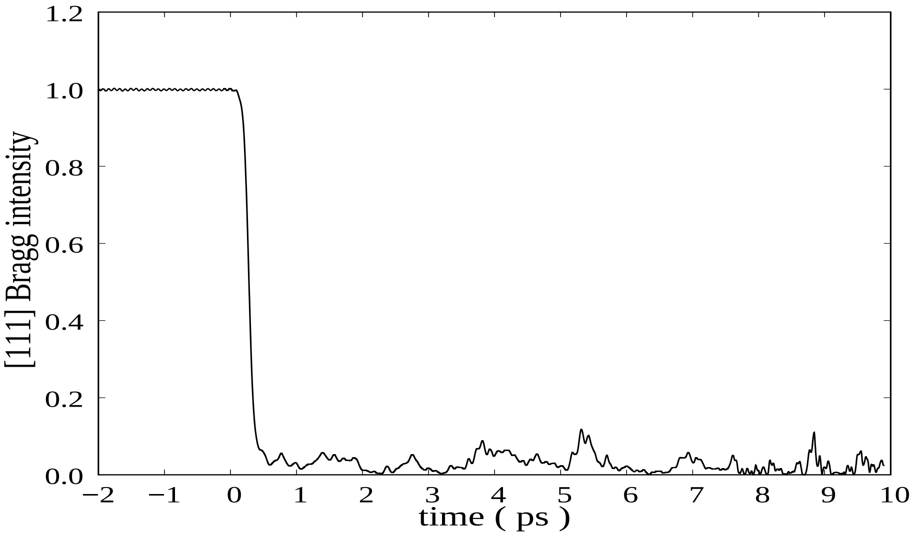

Figure 3.28: Time evolution of the [111] Bragg peak intensity of Ge after excitation with a laser pulse of $= 50fs$ duration. The energy absorbed from the laser is $3.8eV/atom$. The peak time of the gaussian pulse corresponds to $t = 0\ ps$.

was chosen, which is slightly beyond the position of the first peak of the pair correlation function shown in Fig. 3.25. Different laser parameters (pulse duration, fluence, intensity) have been used. As examples, we show in Figs. 3.26 and 3.25 the calculated bond angles distribution and the pair correlation as a function of time before and after laser excitation. The pulse duration was $\tau = 50$ fs and the absorbed energy $E_{abs} = 2.6$ eV. The initial temperature of the crystalline Ge supercell was $T = 10$ K. Before the action of the laser pulse, the bond angles distribution shows a very sharp peak at 109 degrees, which gives evidence of the tetrahedral nature of the bond distribution in the initial diamond crystal structure of the cold Ge. This is confirmed by the sharp peaks observed in the pair distribution functions before the action of laser. As a consequence of laser excitation, however, the bond distribution peak starts to broaden very rapidly. For a time-delay of 400 fs the whole range of bond angles from 60 to 120 degrees can be found with high probability, which means that the crystalline ordering starts to be destroyed. According to our simulations the time scale for non-thermal melting is less than half a picosecond. The disordered nature of the crystal can also be seen from the plot of the correlation function at time $t = 400\ fs$ in Fig. 3.25.

In another side, we computed the time-dependent [111] Bragg peak intensity. In Figs. 3.27 and 3.28 we show the behavior of this peak in time for absorbed energies $E_{abs} = 2.6$ eV, $E_{abs} = 3.0$ eV and $E_{abs} = 3.8$ eV. On can observed from 3.27 a significant drop of the intensity for both absorbed energies within 300 fs after the excitation. The drop is followed by an exponential increase of the intensity due to the energy exchange between electrons and ions. In fact the crystal tends to regain its initial ground state after that the process of the energy absorption is complete. The electron phonon coupling time used in the present work was $\tau = 2.8\ ps$. The analysis of the atomic structure in real space (radial distribution function in fig. 3.25, bond angles distribution in fig. 3.26) shows that the crystal melts when the Bragg peak intensity looses more than 25% of its initial value (*i.e.* $Intensity < 0.75$). However, at very high laser intensity (absorbed energy near the ablation threshold which is $\approx 4.2\ eV$ for pulse duration of $50\ fs$), the peak disappears completely at time scale less than $500\ fs$ giving evidence of the complete disordered nature of the crystal. This is illustrated in Fig. 3.28. Experiments based on time-resolved reflectivity measurements [BBSS06] have shown that the lattice destabilization can take place in less than $500 fs$ after the excitation depending on the pulse intensity, this is confirmed by our calculations.

Chapter 4

Summary and Outlook

In this thesis we have developed theoretical models to describe the ultrafast structural response of different solids to an intense femtosecond laser excitation (*intenstiy* $I \approx 10^{12} - 10^{13} W/cm^2$), *pulse duration* $\tau < 500fs$). Our approaches provide theoretical frameworks for the treatment of non-equilibrium states in solids and the link between microscopic and macroscopic quantities via the calculation of the time-dependent potential energy surface. We have studied the structural responses of cerium, bismuth and germanium upon femtosecond laser excitation. The structural properties of samarium sulfide has been also studied. Quantitative agreements have been found with the existing experimental results and predictions have also been made.

The following results were obtained:

- We have used a hydrodynamic approach combined with an electronic model Hamiltonian to demonstrate that an ultrafast photo-induced transition involving large local volume and electronic changes can be induced in cerium. In the range of electronic temperatures we have considered in this work, the photoinduced transition occurs as rapid expansion of the solid, initially in the high density α phase, due to the strong excitation of the band electrons. This expansion is accompanied by electron localization.

Moreover, also the structural properties of samarium sulfide have been investigated. For this, we have used the local density approximation + interatomic Coulomb interaction (LDA+U) in the framework of the density functional theory. Our results showed that by choosing an appropriate value of U, the structural properties of SmS can be well described. We discussed the possibility of modeling the experimentally observed isostructural transition [KTM03] induced by femtosecond laser pulse.

- Secondly, we have performed quantum dynamical simulations on time-dependent potential energy surfaces calculated using DFT + LDA in order to elucidate the origin of the experimentally observed [MMHK04] beatings of laser-induced coherent phonons in bismuth. It emerged from our study that the behavior of the excited phonons approaches the classical behavior rapidly when increasing the system size. This is a strong indication that quantum effects do not play an important role in the generation of the observed beatings, and that the observed phenomena is probably classical origin.

- Finally, we have performed molecular dynamics (MD) simulation on the basis of a nonorthogonal tight binding (NOTB) Hamiltonian to study the dynamics of semiconductor germanium upon femtosecond laser excitation. With our NOTB model combined with MD simulation, we first described the equilibrium and thermal properties of germanium and analyzed the different phases in the range of temperature going from 0K to 4000K (well above the melting point $T_{melt} = 1210K$). The different phases of germanium as function of temperature were well described. Therefore being confident of the efficiency of the method to describe inter-atomic forces in germanium, we studied the non-thermal melting induced by femtosecond laser pulse under different perspectives. The laser parameters such as fluences, pulses duration have been varied and their effects on the structural phase transitions have been analysed. We were able to show that the non-thermal melting of germanium can take place on sub-picosecond time scales as it was observed experimentally [STBB$^+$03, BBSS06] and is mainly caused by the softening of the transverse acoustic modes. Moreover we also discussed the generation mechanisms of coherent phonons in germanium.

This work is a continuation of the considerable efforts done so far to understand the mechanism underlying the dynamics of solids under laser excitation. With our theoretical models and simulation methods we were able to describe and give interpretations of most structural phenomena which occur in solids under femtosecond laser excitation. However, there are some experimental features which were not taken into account in the proposed models. For example, the spatial laser profile and the subsequent temperature profile in the heated spot were not included. We assumed an uniform distribution of all these quantities. This assumption has not unduly influenced the results that were compared to experimental results.

The future of this work lies in developing more accurate models to include all the physical aspects of the materials. The models must be valid for the whole range of time from femtosecond to nanosecond time scale. An accurate time treatment of the carriers mobility during and after the laser excitation should be considered. The environment of the heated spot and the spatial energy profile must be involved in the calculation.

The unquestionable success of the density functional theory for the description of the ground state properties of large material classes (semiconductors, insulators, metals, rare earth) makes it the most efficient basis of any future electronic structure theory for a precise description of the nonequlibrium states of materials.

It is clear that for reasons related to technologcal applications which result, study of laser-matter interaction remains an active and exciting research subject for both theoreticians and experimentalists.

Appendix A

The Frozen phonon approach

We describe here the approach used to compute the phonon specrum of bulk Ge. First of all the force constants

$$\phi\left(li,l'j\right)=-\frac{F_{\beta}\left(l',j\right)}{\Delta u_{\alpha}\left(l,i\right)}\tag{A.1}$$

are calculated from Eq. 2.56. i. e. the ratio of the force acting on atom j of the $l'-th$ unit cell in the β direction to the displacement of atom i of the $l-th$ unit cell in the α direction. Note that α and β are independent directions and are arbitrary chosen. $\alpha,\beta=x,y,z$ are directions along the cartesian axis (see fig. 3.14). In practise what is done is, an atom is moved along a specific direction with a small amount of displacement Δu from its equilibrium position. Because of the lattice distortion due to this atomic displacement the forces acting on atoms in the rest of the cell become more significants, thus the force constants $\phi\left(li,l'j\right)$ are evaluated. The relaxed positions of the atoms and force constants calculated from the Hamiltonian through the Helmann-Feynmann theorem Eq. 2.56 are then used to build the dynamical matrix for the entire system. The phonon are derived from the diagonalization of the Fourier transform of the real space dynamical matrix (see below). In fact the diagonalization of the q-space dynamical matrix gives the vibrational frequencies and there corresponding eigenvectors. At a given q-point in the reciprocal space, an element of a dynamical matrix is calculated by a sum of the force constants in the supercell multiplied by a phase factor.

$$M\left(q,ij\right)=\frac{1}{\left(m_{i}m_{j}\right)^{\frac{1}{2}}}\sum_{l'}\phi\left(li,l'j\right)exp\left[iq\left(R\left(l',j\right)-R\left(0,i\right)\right)\right]\tag{A.2}$$

l' runs through the unit cell inside the supercell. In our study we sampled the first Brillouin zone of diamond structure of Ge with 512 q-points meshed along the high symmetry directions. The international crystallography table have been used for the determination of the q points coordinate. The phonon frequencies can be obtained from the diagonalization of the dynamical matrix $M(q)$ described in eq. A.2 by solving the following eigenvalues equation

$$\omega^2 e(q,\nu) = M(q)\, e(q,\nu)\,, \tag{A.3}$$

where $\omega e(q,\nu)$ and $e(q,\nu)$ are respectively eigenvalues and eigenvectors (polarisation vector). The eigenvalue ω may be positive (real frequency) or negative (pure imaginary frequency) depending on the physical conditions (see text). The phonon density of states (DOS) is given by

$$D(\omega) = \frac{1}{N_q}\sum_{q,\nu} g\left(\omega - \omega(q,\nu)\right), \tag{A.4}$$

with N_q the number of $q-points$, ω the phonon frequency and $g(\omega)$ a broadening function with Gaussian shape. Because of accuracy reasons of the frozen-phonon approximation, The vibrational simulations results presented in this work were computed by averaging in several supercells. However our calculations show similar results for supercell sizes N=64, 216, 512, this means that our N=64 supercell is large enough to give reasonable description of Ge bulk. The eigenvector $e(q,\nu)$ in Eq. A.4 corresponding to a particular mode gives the relative amplitude and also the direction that each of atoms in the supercell moves under laser excitation of that mode. $e(q,\nu)$ is a polarization vector. For the treatment of optical modes a non-analytical term must be added to the dynamical matrix, this is due to the long range interaction when $k \to 0$ in case of semiconductors.

Bibliography

[AAL97] V.I. Anisimov, F. Aryasetiawan, and A.L. Lichtenstein. *J. Phys.: Condens. Matter*, 9:767, 1997.

[ABGA06] B. Amadon, S. Biermann, A. Georges, and F. Aryasetiawan. *Phys. Rev. Lett.*, 96:066402, 2006.

[AGL71] B. Alascio, V. Grunfeld, and A. Lopez. *Solid State Commun*, 9:1711, 1971.

[AHY00] V.N. Antonov, B.N. Harmon, and A.N. Yaresko. *Phys. Rev. B*, 63:205112, 2000.

[AHY02] V.N. Antonov, B.N. Harmon, and A.N. Yaresko. *Phys. Rev. B*, 66:165208, 2002.

[AL92] J.W. Allen and L.Z. Liu. *Phys. Rev. B*, 46:5047, 1992.

[ALO73] B. Alascio, A. Lopez, and C.F.E. Olmedo. *J. Phys. F: Metal Phys.*, 3, 1973.

[AM82] J.W. Allen and R. M. Martin. *Phys. Rev. Lett.*, 49:1106, 1982.

[AOL$^+$81] J. W. Allen, S.-J. Oh, I. Lindau, J.M. Lawrence, L.I. Johansson, and S.B. Hagstrom. *Phys. Rev. Lett.*, 46:1100, 1981.

[AOL$^+$82] J.W. Allen, S.-J. Oh, I. Lindau, M. B. Maple, J.F. Suassuna, and S.B. Hagstrom. *Phys. Rev.*, 26:445, 1982.

[AP89] I.Sh. Averbukh and N.F. Perelman. *Phys. Lett. A*, 139:449, 1989.

[AW57] B.J. Alder and T.E. Wainwright. *J. Chem. Phys.*, 27:1208–1209, 1957.

[BBSS06] J. Bonse, G. Bachelier, J. Siegel, and J. Solis. *Phys. Rev. B*, 74:134106, 2006.

[BFI87] S.D. Brorson, J.G. Fujimoto, and E.P. Ippen. *Phys. Rev. Lett.*, 59:1962, 1987.

[BGR$^+$08] D. Boschetto, E.G. Gamaly, A.V. Rode, B. Luther-Davies, D. Glijer, T. Garl, O. Albert, A. Rousse, and J. Etchepare. *Phys. Rev. Lett.*, 100:11225, 2008.

[Bir47] F. Birch. *Phys. Rev.*, 71:809–824, 1947.

[BMP00] N. Bernstein, M.J. Mehl, and D.A. Papaconstantopoulos. *Phys. Rev. B*, 62:4477, 2000.

[BOA] *The BOA claims that due the difference between electrons and ions mass (electron mass is three times smaller than the ion mass), the electrons move very fast compared to the ionic motion. This can be explained by the fact that the forces acting on both nuclei and electrons due to their electric charge, are of the same order of magnitude and consequently the change in their momenta as a result of these forces are also the same.*

[Bor00] J.K. Bording. *Phys. Rev. B*, 62:7103, 2000.

[BSM$^+$01] P. Blaha, K. Schwarz, G.K.H. Madsen, D. Kvasnicka, and J. Luitz. Wien2k, an augmented plane wave + local orbitals program for calculating crystal properties (technische universität wien austria). 2001.

[CBRZ08] F. Carbone, P. Baum, P. Rudolf, and A. H. Zewail. *Phys. Rev. Lett.*, 100:035501, 2008.

[CBWL74] M. Campagna, E. Burke, G.K. Wertheim, and L.D. Longinotti. *Phys. Rev. Lett.*, 33:820, 1974.

[Cha78] D.J. Chadi. *Phys. Rev. Lett.*, 41:1062, 1978.

[Cha84] D.J. Chadi. *Phys. Rev. B*, 29:785, 1984.

[CTS$^+$01] A. Cavalleri, C. Tóth, C. W. Siders, J. A. Squier, F. Ráksi, P. Forget, and J. C. Kieffer. *Phys. Rev. Lett.*, 87:237401, 2001.

[CVJ$^+$92] J.P. Perdew J.A. Chevary, S. Vosko, K.A. Jackson, M.R. Pederson, D.J. Singh, and C. Fiolhais. *Phys. Rev. B*, 46:6671, 1992.

[DGJY04] T. Dumitrica, M.E. Garcia, H.O. Jeschke, and B.I. Yakobson. *Phys. Rev. Lett.*, 92:117401, 2004.

[DGJY06] T. Dumitrica, M.E. Garcia, H.O. Jeschke, and B.I. Yakobson. *Phys. Rev. B*, 74:193406, 2006.

[ea04] I.K. Jeong et al. *Phys. Rev. Lett.*, 92:105702, 2004.

[ESRL91] T. Elsaesser, J. Shah, L. Rota, and P. Lugli. *Phys. Rev. Lett.*, 66:1757, 1991.

[Fey56] R. Feynman. *Phys. Rev.*, 56(4):340, 1956.

[FF82] M.D. Feit and J.A. Fleck. *J. Chem. Phys.*, 78:301, 1982.

[FWK$^+$95] Th. Frauenheim, F. Weich, Th. Kohler, S. Uhlmann, D. Porezag, and G. Seifert. *Phys. Rev B*, 52:1995, 1995.

[GDG83] D. Guidotti, T.A. Driscoll, and H.J. Gerritsen. *Solid State Com.*, 46:337, 1983.

[GDJ04] M.E. Garcia, T. Dumitrica, and H.O. Jeschke. *App. Phys. A*, 79:855, 2004.

[GJ03] M.E. Garcia and H.O. Jeschke. *Appl. Surf. Sci.*, 208-209:61, 2003.

[GMCP89] G. Galli, R. M. Martin, R. Car, and M. Parrinello. *Phys. Rev. Lett.*, 63:988, 1989.

[GMR69] D. Gustafson, J. McNutt, and L. Roellig. *Phys. Rev.*, 183:435, 1969.

[GR73] W. H. Gust and E. B. Royce. *Phys. Rev. B*, 8:3595, 1973.

[GSP89] L. Goodwin, A.J. Skinner, and D.G. Pettifor. *Europhys. Lett.*, 9:701, 1989.

[G32] P. Gttinger. *Z. Phys.*, 73:69, 1932.

[Har] Walter A. Harrison. *Electronic structure and the properties of Solids.*

[HE] R.W. Hockney and J.W. Eastwood. *Computer Simulations Using Particles.*

[HEH$^+$08] M. Harb, R. Ernstorfer, Ch.T. Hebeisen, G.Sciaini, W. Peng, T. Dartigalongue, M.A. Eriksson, M.G. Lagally, S.G. Kruglik, and R.J.D. Miller. *Phys. Rev. Lett.*, 100:155504, 2008.

[HK64] P. Hohenberg and W. Kohn. *Phys. Rev.*, 136:B864, 1964.

[HKNM02] M. Hase, M. Kitajima, S.-I. Nakashima, and K. Mizoguchi. *Phys. Rev. Lett.*, 88:067401, 2002.

[HMS01] K. Held, A.K. McMahan, and R. T. Scalettar. *Phys. Rev. Lett.*, 87:276404, 2001.

[Hof63] R. Hoffmann. *J. Chem. Phys.*, 39:1397–1412, 1963.

[HOSK05] K. Haule, V. Oudovenko, S.Y. Savrasov, and G. Kotliar. *Phys. Rev. Lett.*, 94:036401, 2005.

[HS83] Tu Hailing and G.A. Saunders. *Phys. Rev. B*, 29:1848, 1983.

[Hub74] J. Hubbard. *Proc. R. Soc. London A*, 276:238, 1974.

[HWDK95] S. Hunsche, K. Wienecke, T. Dekorsy, and H. Kurz. *Phys. Rev. Lett.*, 75:1815, 1995.

[IKU06] K. Ishioka, M. Kitajima, and K. Ushida. *Journal of Physical Society of Japan*, 75:084704, 2006.

[IZ03] D. S. Ivanov and L. V. Zhigilei. *Phys. Rev. B*, 68:064114, 2003.

[JBM$^+$08] S. L. Johnson, P. Beaud, C. J. Milne, F. S. Krasniqi, E. S. Zijlstra, M. E. Garcia, M. Kaiser, D. Grolimund, R. Abela, and G. Ingold. *Phys. Rev. Lett.*, 100:155501, 2008.

[JDG09] H.O. Jeschke, M.S. Diakhate, and M.E. Garcia. *App. phys. A*, 96:3342, 2009.

[JG] H. O. Jeschke and M. E. Garcia. *Ultrafast structural changes induced by femtosecond laser pulses.*

[JG02] H.O. Jeschke and M.E. Garcia. *Appl. Surf. Sci.*, 197-198:107, 2002.

[JGB99a] H.O. Jeschke, M.E. Garcia, and K.H. Bennemann. *Phys. Rev. B*, 60:R3701, 1999.

[JGB99b] H.O. Jeschke, M.E. Garcia, and K.H. Bennemann. *Appl. Phys. A*, 69:49, 1999.

[JGB01] H. O. Jeschke, M. E. Garcia, and K. H. Bennemann. *Phys. Rev. Lett.*, 87:015003, 2001.

[JGB02] H.O. Jeschke, M.E. Garcia, and K.H. Bennemann. *J. Appl. Phys.*, 91:18, 2002.

[JGL$^+$02] H.O. Jeschke, M.E. Garcia, M. Lenzner, J. Bonse, J. Krüger, and W. Kautek. *Appl. Surf. Sci.*, 197-198:839, 2002.

[JHL$^+$03] S.L. Johnson, P.A. Heimann, A.M. Lindenberg, H.O. Jeschke, M.E. Garcia, Z. Chang, R.W. Lee, J.J. Rehr, and R.W. Falcone. *Phys. Rev. Lett.*, 91:157403, 2003.

[JLMC94] Jr. J. L. Mercer and M.Y. Chou. *Phys. Rev. B*, 49:8506, 1994.

[JNM70] A. Jayaraman, V. Narayanamurti, and R.G. Maines. *Phys. Rev. Lett.*, 25:1430, 1970.

[Joh74] B. Johansson. *Philos. Mag.*, 30:469, 1974.

[KBW$^+$94] I. Kwon, R. Biswas, C.Z. Wang, K.M. Ho, and C.M. Soukoulis. *Phys. Rev. B*, 49:7242, 1994.

[KCL$^+$88] W.H. Knox, D.S. Chemla, G. Livescu, J.E. Cunningham, and J.E. Henry. *Phys. Rev. Lett.*, 61:1290, 1988.

[KEH$^+$07] C. Kübler, H. Ehrke, R. Huber, R. Lopez, A. Halabica, R. F. Haglund, and A. Leitenstorfer. *Phys. Rev. Lett.*, 99:116401, 2007.

[KHCP05] M. Kitajima, M. Hase, A.M. Constantinescu, and H. Petek. volume 79. Springer Berlin Heidelberg, 2005.

[KLL80] U. Kornstadt, R. Lasser, and B. Lengeler. *Phys. Rev.*, 21:1898, 1980.

[KM] K. Kunc and R. M. Martin. In proceedings of the international conference on phonon physics, bloomington, indiana, 1981.

[KM82] K. Kunc and R. M. Martin. *Phys. Rev. Lett.*, 1982.

[KS65] W. Kohn and L.J. Sham. *Phys. Rev.*, 140:A1133, 1965.

[KTM03] R. Kitagawa, H. Takebe, and K. Morinaga. *Appl. Phys. Lett.*, 82:3641, 2003.

[KZ90] L.R Khundkar and A.H. Zewail. *Ann. Rev. Phys. Chem.*, 41:15–40, 1990.

[LED$^+$05] M. Lüders, A. Ernst, M. Däne, Z. Szotek, A. Svane, D. Ködderitzsch, W. Hergert, B.L. Györffy, and W.M. Temmerman. *Phys. Rev. B*, 71:205109, 2005.

[LKJ$^+$00] A. M. Lindenberg, I. Kang, S.L. Johnson, T. Missalla, P.A. Heimann, Z. Chang, J. Larsson, P.H. Bucksbaum, H.C. Kapteyn, H.A. Padmore, R.W. Lee, J.S. Wark, and R.W. Falcone. *Phys. Rev. Lett.*, 84:111, 2000.

[LLC83] M. Lavagna, C. Lacroix, and M. Cyrot. *J. Phys. F: Met. Phys.*, 13:1007–1015, 1983.

[LLSTeA05] A. M. Lindenberg, J. Larsson, K. Sokolowski-Tinten, and K. J. Gaffney et Al. *Science*, 308:392, 2005.

[LM88] D.C. Langreth and M.J. Mehl. *Phys. Rev. B*, 38:3098, 1988.

[LSK88] Z.W. Lu, D.J. Singh, and H. Krakauer. *Phys. Rev. B*, 37:10045, 1988.

[MBS$^+$01] G.K.H. Madsen, P. Blaha, K. Schwarz, E. Sjöstedt, and L. Nordström. *Phys. Rev. B*, 64:195134, 2001.

[Mer65] N.D. Mermin. *Phys. Rev. B*, 137:A1441, 1965.

[MMHK04] O.V. Misochko, K. Ishioka M. Hase, and M. Kitajima. *Phys. Rev. Lett.*, 92:197401–1, 2004.

[MS94a] M. Menon and K.R. Subbaswamy. *Phys. Rev B*, 50:11577, 1994.

[MS94b] M. Menon and K.R. Subbaswamy. *Phys. Rev B*, 47:12754, 1994.

[MS98] M. Menon and K.R. Subbaswamy. *J. Phys.: Condens. Matter*, 10:10991, 1998.

[MSN00] O.V. Misochko, K. Sakai, and S. Nakashima. *Phys. Rev. B*, 61:11225, 2000.

[NHM$^+$01] M. Nakajima, H. Harima, K. Morita, K.M. Itoh, and K. Mizoguchi. *Phys. Rev. B*, 63:161304, 2001.

[NN70] G. Nilsson and G. Nelin. *Phys. Rev. B*, 3:364, 1970.

[OA84] S.-J. Oh and J. W. Allen. *Phys. Rev. Lett.*, 33:589, 1984.

[PBE96] J.P. Perdew, K. Burke, and M. Ernzerhof. *Phys. Rev. Lett.*, 77:3865, 1996.

[PBF92] D. Porezag G. Seifert P. Blaudeck, Th. Frauenheim and E. Fromm. *J. Phys.: Condens. Matter*, C4:6389, 1992.

[PHP$^+$92] E. D. Potter, J. L. Herek, S. Pedersen, Q. Liu, and A.H. Zewail. *Nature*, 355:66–68, 1992.

[PKKS92] T. Pfeifer, W. Kütt, H. Kurz, and R. Scholz. *Phys. Rev. Lett.*, 69:3248, 1992.

[PMCL03] A.G. Petukhov, I.I. Mazin, L. Chioncel, and I. Lichtenstein. *Phys. Rev. B*, 67:153106, 2003.

[PR81] M. Parrinello and A. Rahman. *J. Appl. Phys.*, 1981.

[PW92] J.P. Perdew and Y. Wang. *Phys. Rev. B*, 45:13244, 1992.

[RF71] R. Ramirez and L.M. Falicov. *Phys. Rev. B*, 3:2425, 1971.

[RGV$^+$05] A.H. Romero, M.E. Garcia, F. Valencia, M. Terrones, H. Terrones, and H.O. Jeschke. *Nano Lett.*, 5:1361, 2005.

[RSTvdLA04] R. Rethfeld, K. Sokolowski-Tinten, D. von der Linde, and S.I. Anisimov. *App. Phys. A*, 79:767–769, 2004.

[RTD$^+$07] M. Rini, R. Tobey, N. Dean, J. Itatani, Y. Tomioka, R.W. Schoenlein Y. Tokura, and A. Cavalleri. *Nature*, 449:72, 2007.

[SABW82] W.C. Swope, H.C. Anderson, P.H. Berens, and K.R. Wilson. *J. Chem. Phys.*, 76:637–649, 1982.

[SAPF96a] P.L. Silvestrelli, A. Alavi, M. Parrinello, and D. Frenkel. *Phys. Rev. Lett.*, 77:3149, 1996.

[SAPF96b] P.L. Silvestrelli, A. Alavi, M. Parrinello, and D. Frenkel. *Phys. Rev. Lett.*, 77:3149, 1996.

[SB90] P. Stampfli and K.H. Bennemann. *Phys. Rev. B*, 42:7163, 1990.

[SB92] P. Stampfli and K.H. Bennemann. *Phys. Rev. B*, 46:10686, 1992.

[SB93] P. Stampfli and K.H. Bennemann. *J. Phys.: Condens. matter*, 5:A173–A174, 1993.

[SB94] P. Stampfli and K.H. Bennemann. *Phys. Rev. B*, 49:7299, 1994.

[SFL98] A.B. Shick, A.J. Freeman, and A.I. Liechtenstein. *J. App. Phys.*, 83:7022, 1998.

[SFPO88] A.P. Sutton, M.W. Finnis, D.G. Pettifo, and Y. Ohta. *J. Phys. C*, 21:35, 1988.

[Sin91] D. Singh. *Phys. Rev. B*, 43:6388, 1991.

[Sin94] D. Singh. *Planewaves, pseudopotentials, and the LAPW method*. Kluwer Academic Boston, 1994.

[SK54] J.C. Slater and G.F. Koster. *Phys.Rev.*, 94:1498, 1954.

[SLFE87] R.W. Schönlein, W.Z. Lin, J.G. Fujimoto, and G.L. Eesley. *Phys. Rev. Lett.*, 58:1680, 1987.

[SLH+82] G.A. Saunders, W.A. Lambson, Tu Hailing, D.W. Bullett, H. Bach, and S. Methfessel. *J. Phys. C: Solid State Phys.*, 15:L551–L556, 1982.

[SNS00] E. Sjöstedt, L. Nordström, and D.J. Singh. *Solid State Commun.*, 114:15, 2000.

[SP98] P.L. Silvestrelli and M. Parrinello. *J. Appl. Phys.*, 83:1998, 1998.

[SPK93] R. Scholz, T. Pfeifer, and H. Kurz. *Phys. Rev. B*, 47:16229, 1993.

[SPL00] A.B. Shick, W.E. Pickett, and A.I. Liechtenstein. *Cond-mat*, page 0001255, 2000.

[STBB+03] K. Sokolowski-Tinten, C. Blome, J. Blums, A. Cavalleri, C. Dietrich, A. Tarasevitch, I. Uschmann, E. Förster, M. Horn von Hoegen, and D. von der Linde. *Nature (London)*, 422:287, 2003.

[STBD+03] K. Sokolowski-Tinten, C. Blome, C. Dietrich, A. Tarasevitch, M. Horn von Hoegen, and D. von der Linde. *Phys. Rev. Lett.*, 87:225701, 2003.

[STBvdL95] K. Sokolowski-Tinten, J. Bialkowski, and D. von der Linde. *Phys. Rev. B*, 51:14186, 1995.

[STvdL04] K. Sokolowski-Tinten and D. von der Linde. *J. Phys. Cond. Matter*, 16:R1517–R1536, 2004.

[SWS+91] P. Saeta, J.K. Wang, Y.N. Siegal, N. Bloembergen, and E. Mazur. *Phys. Rev. Lett.*, 67:1023, 1991.

[sy96] Pavol Farka sovsk y. *Phys. Rev. B*, 54:7865, 1996.

[SYH83] C.V. Shank, R. Yen, and C. Hirlimann. *Phys. Rev. Lett.*, 51:900, 1983.

[TABC88] H.W.K. Tom, Aumiller, and C.H. Bruto-Cruz. *Phys. Rev. Lett.*, 60:1438, 1988.

[Tog] A. Togo. *http://fropho.sourgeforge.net/.*

[vdEKvdM01] J.W. van der Eb, A.B. Kuz'menko, and D. van der Marel. *Phys. Rev. Lett.*, 86:3407, 2001.

[Vera] L. Verlet. "computer experiment on classical fluids. *ii. equilibrium correlation functions.*

[Verb] L. Verlet. "experiments" on classical fluids. *i. thermodynamical properties of lennard-jones molecules.*

[VGCC96] A. De Vita, G. Galli, A. Canning, and R. Car. *Nature*, 379:523, 1996.

[vSH71] M. van Schilfgaarde and W.A. Harrison. *Phys.Rev. Lett.*, 67:3487, 1971.

[VVS96] M.J. Vrakking, D.M. Villeneuve, and A. Stolow. *Phys. Rev. A*, 54:R37, 1996.

[WFP+94] W. Woerner, W. Frey, M.T. Portella, C. Ludwig, T. Elsaesser, and W. Kaiser. *Phys. Rev. B*, 49:17007, 1994.

[WH52] M. Wolfsberg and L. J. Helmholz. *J. of Chem. Phys.*, 20:837, 1952.

[WHC93] C.Z. Wang, K.M. Ho, and C.T Chan. *Phys. Rev. Lett.*, 70:611, 1993.

[XWCH92] C.H. Xu, C.Z. Wang, C.T. Chan, and K. M. Ho. *Phys. Cond. Mat.*, 4:6047, 1992.

[YMJ90] J.A. Yeazell, M. Mallalieu, and C. R. Stroud Jr. *Phys. Rev. Lett.*, 64:2007, 1990.

[YN87] Y.X. Yan and K.A. Nelson. *J. Chem. Phys.*, 87:6240, 1987.

[Zew88] A.H. Zewail. *Science*, 242:1645–1653, 1988.

[Zew92] A.H. Zewail. Academic Press Boston, 1992.

[Zew00] A.H. Zewail. *J. Phys. Chem. A*, 104:5660–5694, 2000.

[ZTG06a] E. S. Zijlstra, L. Tatarinova, and M. E. Garcia. *phys. Rev.B*, 74:220301, 2006.

[ZTG06b] E.S. Zijlstra, L. Tatarinova, and M.E. Garcia. *Proc. SPIE*, 6261:62610R, 2006.

[ZVC+91] H.J. Zeiger, J. Vidal, T.K. Cheng, E.P. Ippen, G. Dresselhaus, and M.S. Dresselhaus. *Phys. Rev. B*, 45:768, 1991.

[ZWG+08] E. S. Zijlstra, J. Walkenhorst, C. Gilfert, C. Sippel, W. Tws, and M. E. Garcia. *Phys. Rev. Lett.*, 101:135701, 2008.

Publications related to this thesis

M. S. Diakhate and M. E. Garcia

"Photoinduced ultrafast local volume changes in intermediate valence solids"

Phys. Rev. B **79**, 094117 (2009).

M. S. Diakhate, E. S. Zijlstra and M. E. Garcia

"Quantum dynamical study of the amplitude collapse and revival of coherent A1g phonons in bismuth: A classical phenomenon?"

Appl. Phys. A **96**, 5-10 (2009).

H. O. Jeschke, M. S. Diakhate and M. E. Garcia

"Molecular dynamics simulations of laser induced damage of nanostructures and solids."

App. Phys. A **96**, 33-42 (2009).

M. S. Diakhate, H. O. Jeschke and M. E. Garcia

"Molecular dynamics simulation of laser induced nonthermal melting of bulk germanium"

Paper in preparation (2009).

Acknowledgements

My acknowledgments will go first to my thesis supervisor Pr. Dr. Martin E. Garcia. I am deeply endepted to him, whose patience and help were very important during this work. This thesis would not be achieved without his stimulating suggestions and encouragements. I am also grateful to Dr. Harald O. Jeschke, for his help and nice collaboration regarding the study of semiconductor germanium. This part of the thesis would not be possible without his assistance. I express also many thanks to Dr. Eeuwe S. Zilstra for his help and nice suggestions on the part regarding the calculations on bismuth.

I thank Pr. Dr. Gustavo M. Pastor for his interest about my work, and for his understanding and his tolerance concerning the time that I took to give the manuscript.

I would like to show my gratitude to Pr. Dr. Burkhard Fricke and Pr. Dr. Thomas Baumert for the interest in my work.

I want to thank the university of Kassel in general for giving me the opportunity to do this thesis, and particularly the personnel of the physics department.

This work is dedicated to my father and my mother, for the long and sincere support. I am particularly very indebted to my father Abdou Salam Diakhate for his care and love. As a typical father in a Senegalese family, he worked to support the family and spare no effort to provide the best possible environment for me and the rest of the family to grow up and attend school, this was not obvious. He had never complained in spite of all the hardships in his life. Although he is no longer with us, he is forever remembered. This work is dedicated to him. I cannot ask for more from my mother, Maguette Diop, as she is simply wonderful. I have no suitable word that can fully describe her love and support to me.

This work would not be possible without the generous support of the Deutsche Forschungsgemeinschaft (DFG) which allowed me to realize my ambition to do my thesis in Germany.

Erklärung

Hiermit versichere ich, daß ich die vorliegende Dissertation selbständig und ohne unerlaubte Hilfe angefertigt und andere als die in der Dissertation angegebenen Hilfsmittel nicht benutzt habe. Alle Stellen, die wörtlich oder sinngemäß aus veröffentlichten oder unveröffentlichten Schriften entnommen sind, habe ich als solche kenntlich gemacht. Kein Teil dieser Arbeit ist in einem anderen Promotions- oder Habilitationsverfahren verwendet worden.

October 2009, Kassel

Momar Sokhna Diakhate